Quantitative Analysis of Magnetic Resonance Diffusion Tensor Imaging of the Human Brain

– The effect of varying number of acquisitions and number of diffusion sensitizing directions

by

Ketil Oppedal

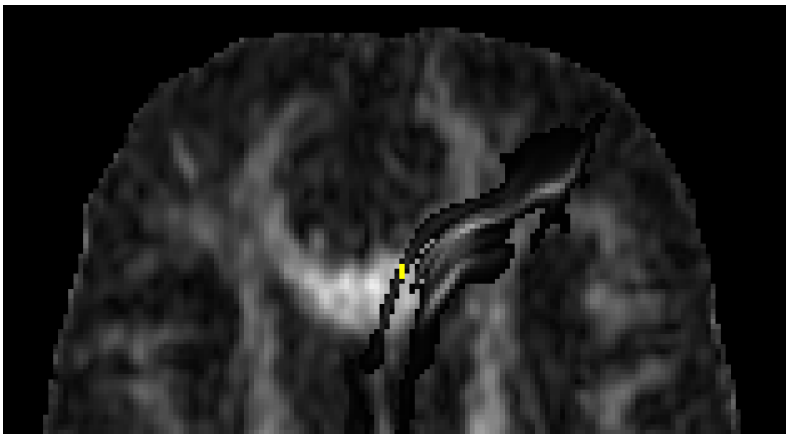

Thesis for the *Candidatus Scientarium* degree in
Experimental and Human Physiology

Department of Biomedicine
Section of Physiology
University of Bergen
Bergen, Norway
May 2005

Frontpage image depicts preliminary results from probabilistic fibre tracking in the corpus callosum region, applying the FDT package from Oxford Centre for Functional Magnetic Resonance Imaging of the Brain to MR-DTI data (isotropic 2.3 x 2.3 x 2.3 mm3 voxels, 25 directions) recorded in a healthy volunteer.

Abstract

Magnetic resonance diffusion tensor imaging (DTI) is both an advanced imaging technique and increasingly clinically important. DTI enables many options and parameters such as number of slices, image matrix, slice thickness, diffusion weighting (i.e. b-value), number of diffusion sensitizing directions, and number of measurements (NEX) to be k-space averaged in each direction.

The aim of my master thesis project was to study which of several different combinations of DTI sequence parameters gives the best estimation of the diffusion tensor (D) and a geometric measure of diffusion anisotropy - the fractional anisotropy (FA) index.

The DTI parameters subject to experimental control were:

(i) the number, K, of diffusion sensitizing gradient directions,
$g_k = (g_{kx}, g_{ky}, g_{kz})^T (k = 1, \ldots, K; K \geq 6)$, and

(ii) the number of image excitations (NEX) used for averaging in each of the directions
$k = 1, \ldots, K$.

It is expected that both increasing K and NEX will increase the quality of the images and the voxel-wise diffusion tensor derived from these image data. However, both factors are increasingly time consuming. The task was then to experimentally determine which combination of (i) and (ii) will give the best result for a fixed duration of measurement time (approximately 7 min).

In this experiment we have used three different experimental setups (protocols) for each of the participating subjects, i.e. 1. K=6 and NEX =8; 2. K=13 and NEX =4; 3. K=25 and NEX =2. Time consumption for each of these protocols was approximately 7 minutes. We compared results from 5 healthy volunteers using a GE Signa 1.5 Tesla Echospeed MR scanner. All subjects were males (age: 24-29 years). Other parameters that were common for all subjects were: 24 axial slices covering the whole brain, 4mm slice thickness, 128x128 acquisition matrix (interpolated to 256x256), b=1000s/mm2.

To analyze the goodness and difference between the three protocols we calculated standard deviation, mean and coefficient of variation of tissue specific (i.e. WM, GM, CSF using SPM2) fractional anisotropy values. We also plotted the standard deviation of FA, as a function of the principal direction of diffusion in three dimensional plots (using spherical coordinates) and employed visual inspection of color-coded fractional anisotropy images as well. All this was done to reveal differences in quality and direction dependent variation in FA between the three protocols.

From our data and analysis we found that there was, in white matter, a slightly higher quality for the protocol with K= 6 and NEX = 8 than for the other two protocols, and for CSF with K= 25 and NEX = 2 the quality was slightly higher than using K=6 and NEX = 8. However the difference was too small to make any firm recommendations between the three protocols. Since a large number of directions enables more sophisticated analysis (e.g. diffusion spectrum imaging, DSI) we recommend a protocol with a high number of directions (for a given measurement time). This is also in accordance with the latest recommendation from the vendor of the scanner where K=25 and NEX=1 is proposed in their standard DTI protocol.

Acknowledgements

The present study was carried out in the Neuroinformatics and Image Analysis group, Section of Physiology, Department of Biomedicine, University of Bergen, from January 2003 to May 2005.

First of all I want to express my gratitude to my supervisor Associate Professor Arvid Lundervold for leading me into the intriguing field of magnetic resonance imaging where I have had the possibility to combine my interests in biology, physics and informatics. I also want to thank him for being an important role model for me as an idealistic, enthusiastic and motivating scientist. I really appreciate the way I naturally have been included in his working environment and his participation in the students daily life. At last I want to thank him for his guidance and support through the work of this thesis, for instance his contributions to programming and commenting on my writings.

My study has been performed on the basis of MR-DTI data acquired at the Department of Radiology, Haraldsplass Deaconess University Hospital. I want to thank Head of Department, MD, PhD Jonn Terje Geitung, MD Pjotr Barkovskij and MR technician Sverre Østerhus for letting me use data from their MR scanner and also part of their time, including the weekends.

I also want to thank the experimental subjects for their participation in the imaging experiments, Ørjan Bergmann for letting me use his MATLAB code, Eirik Thorsnes for his extensive knowledge and help on Linux and LaTeX, Stefan Skare for letting me use his program for calculating diffusion sensitizing gradient directions and some of the figures from his thesis, Trygve Nilsen for his instructive work on tensor calculation, other fellow students for the social events at the university, especially Eyvind Kartveit for holding out with my stupidity, hours and hours of discussions of philosophical, religious and everyday character, his unceremoniously behaviour and for introducing me to triathlon and Martin Ystad for his contributions to making the working day nice at our image analysis laboratory.

Finally I will express my deep gratitude to friends and family - for their persistent encouragement and continuous support. An exceptional special and deep thanks goes to my beautiful girlfriend and future wife Henriette, for giving me, and bringing up, the most extraordinary beautiful daughter I could ever dream of, "eg elske deg!".

Bergen, May 2005

Ketil Oppedal

Contents

List of Figures

List of Tables

1

General Introduction

1.1 Diffusion of molecules

1.1.1 The diffusion process

Diffusion is a physical process that involves the translational movement of molecules from one part of space to another via thermally driven random motions called Brownian motions. It can be illustrated by the classical experiment (see fig. 1.1) in which a tall cylindrical container has its lower part filled with iodine solution and a column of clear water is poured on top in such a way that no convection currents are set up. At first the colored part is separated from the clear part by a sharp, well-defined boundary. Later it is found that the upper part becomes colored, the color getting fainter towards the top, while the lower part becomes correspondingly less intensely colored until a sufficient time has passed and the whole solution appears uniformly colored. There is an indisputable transfer of iodine molecules from the lower to the upper part of the vessel taking place in the absence of convection currents. The iodine is said to have diffused into the water. By replacing the iodine with particles small enough to share the molecular motions, but large enough to be visible under the microscope, it will be possible to observe that the motion of each molecule is random. In a dilute solution the diffusing molecules will seldom meet and will therefore behave independently. Each will constantly undergo collisions with solvent molecules which sometimes

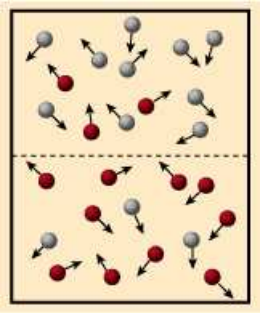

Figure 1.1: The diffusion process

results in motion towards a region of higher concentration and sometimes towards a region of lower concentration, having no preferred direction. The motion of a single molecule can be described in terms of a "random walk", and whilst it is possible to calculate the mean-square distance traveled in a given interval of time it is not possible to say in what direction that given molecule will move in that time. The picture of the diffusion as a random motion process which has no preferred direction, has to be reconciled with the fact that the diffusing particle is nevertheless observed to move from a region of high concentration to a region of low concentration. To illustrate this, imagine any horizontal section in the solution and two thin, equal, elements of volume one just below and one just above the section. Even if it is not possible to predict which way any particular diffusion molecule will move in a given interval of time, it will be discovered that on the average the same amount of molecules will cross the section upwards from the lower volume as will downwards from the upper volume. Thus, simply because there are more diffusion molecules in the lower element than in the upper one, there is a net transfer from the lower to the upper side of the section as a result of random molecular motion.

1.1.2 Diffusion isotropy and anisotropy

In a given amount of time the distance the water molecule diffuses can be the same in all directions or longer in some directions than others. The former case is termed isotropic diffusion and the latter case anisotropic diffusion. In a pure liquid where there are no hindrances to diffusion or in a sample where the barriers are not coherently oriented water molecules diffuse isotropically or nearly isotropically. In a sample with highly oriented barriers the diffusion distance depends on which direction it spreads out, hence the water molecules diffuse anisotropically. In this way, structural subtypes can be identified simply on the basis of their diffusion characteristics and the anisotropy is directly related to the geom-

etry of the diffusion hindrances. In our case we study water diffusion in tissue using proton magnetic resonance diffusion tensor imaging (MR-DTI), where diffusion characteristics such as isotropy and anisotropy are related to the geometry and physico-chemical properties of local tissue micro-architecture.

1.1.3 The concept of eigenvectors and eigenvalues of a tensor matrix

The six different components of the diffusion tensor are defined according to the scanner frame of reference, i.e. reference coordinate system for the diffusion sensitizing gradients $\mathbf{g}_k$ (see section 1.3). However, it is possible to transform the calculated diffusion tensor $\mathbf{D}$ into another tensor matrix D having off-diagonal elements equal to zero, i.e. matrix diagonalization. $\mathbf{D} = PDP^{-1}$ if the column vectors of P are n linearly independent eigenvectors of $\mathbf{D}$ and the diagonal entries of D are the corresponding eigenvalues. We say a 3×3 matrix A has an eigenvector $\mathbf{e}$ and corresponding eigenvalue λ if $Ax = \lambda x$ where the eigenvector $\mathbf{e}_i$ for $i = 1$ corresponding to the largest eigenvalue λ_i denotes the principal direction of diffusivity.

1.1.4 Remark on spatial transformation of DTI data

When registering DT-MR images, a spatial transformation of the data is applied. However, it is well known that spatial transformation of a tensor field is different from transformation of scalar images, because DTI contains directional information which are affected by the transformation [1]. In this paragraph we show how the tissue-based principal diffusion direction (i.e. direction of eigenvector associated to the largest eigenvalue) can be preserved when applying spatial transformations consisting of a series of simple rotations of the x-, y- and z-axis.

Assume that R is the 3x3 rotation matrix representing the image transformation. Then it can be shown (e.g. [1]) that if each diffusion tensor D is replaced by D', defined by the similarity transform, D' = RDRT, then the new diffusion tensors D' are consistent with the anatomical structures being transformed. This is so because a similarity transform preserves the eigenvalues, and only the eigenvectors are affected.

Before we present results from our MATLAB implementation of the similarity transform, we give an example where the original image is transformed, and where the values at each voxel in the transformed image is simply copied from the corresponding position in the original image using some interpolation method [2]. In Fig. 1.2 (b) we see that the fiber pathways in the corpus callosum no longer points in the same direction as in the pre-transformed image (a). However, after

proper reorientation of the tensor (using the above similarity transform) we see that the local tissue orientation is preserved (Fig. 1.2 (c)). In Fig. 1.3 we see the effect of using the similarity transform for given tensor D and rotation matrix R (as implemented in MATLAB, where a fragment of the code is given in appendix B.1).

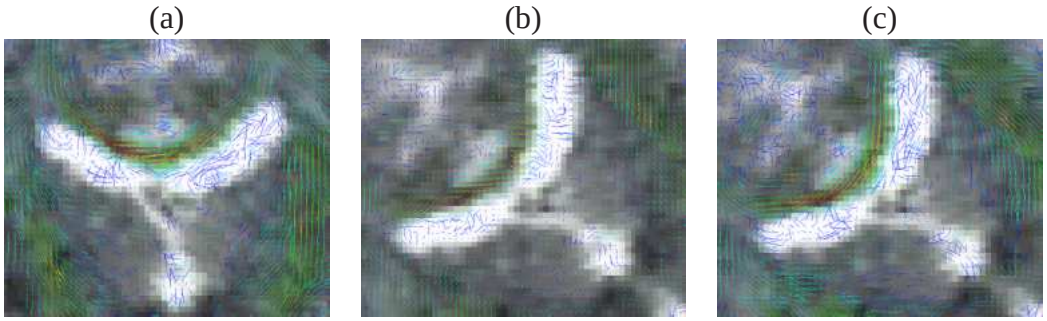

Figure 1.2: A 45° rotation of the DT-MRI image, with and without tensor reorientation (modified from [2]). (a) tensor glyph image (zoomed in around the corpus callosum), (b) rotated image without reorientation of tensors, (c) rotated image after reorientation of tensors.

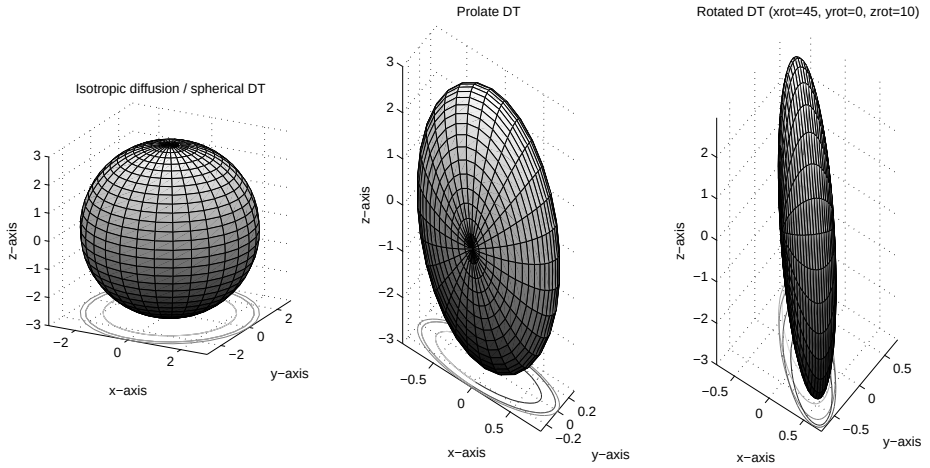

Figure 1.3: A tensor representing spherical diffusion, prolate diffusion and a tensor which is rotated 45° around the x-axes and 10° around the z-axis.

1.2 Causes for anisotropy in the human brain

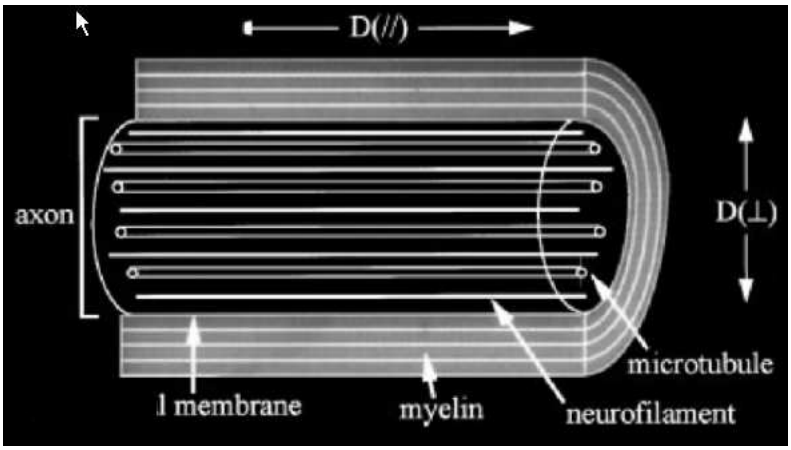

Figure 1.4: *Myelin*, the *axonal membrane*, *microtubules* and *neurofilaments* are all longitudinally oriented structures that could hinder water diffusion perpendicular to the length of the axon and cause the perpendicular diffusion coefficient $D\perp$ to be smaller than the parallel diffusion coefficient $D\parallel$. Other postulated sources of diffusion anisotropy are axonal transport and susceptibility-induced gradients. Taken from Beaulieu [3].

1.2.1 Myelin and axonal membranes

The interest in studying the white matter maturation and demyelinating diseases such as multiple sclerosis with diffusion weighted MRI has probably forced through the unproven hypothesis of the time for anisotropic diffusion, namely that the myelin sheath encasing the axons is the primary source for anisotropy. The numerous lipid bilayers of myelin have limited permeability to water and would be expected to hinder diffusion perpendicular to the fibers more than diffusion in the parallel direction. If myelin were the sole source of anisotropy, then it would be expected that diffusion would be much more isotropic in a normal fiber tract without myelin. In one of the first systematic studies on the underlying source of anisotropy, this was found not to be the case by Beaulieu and Allen [5], who showed that water diffusion was significantly anisotropic in a normal, intact, non-myelinated olfactory nerve of the garfish. The degree of anisotropy in these excised nerve samples measured at room temperature was quite similar to the anisotropy measured *in vivo* in humans, lending credibility to the *in vitro* data, although the absolute ADC values were likely modulated by the excision of the nerves and the temperature difference. This study provided the first evidence that myelin was not an essential component for anisotropic diffusion in neural fibers and that structural features of the axons other than myelin are suffi-

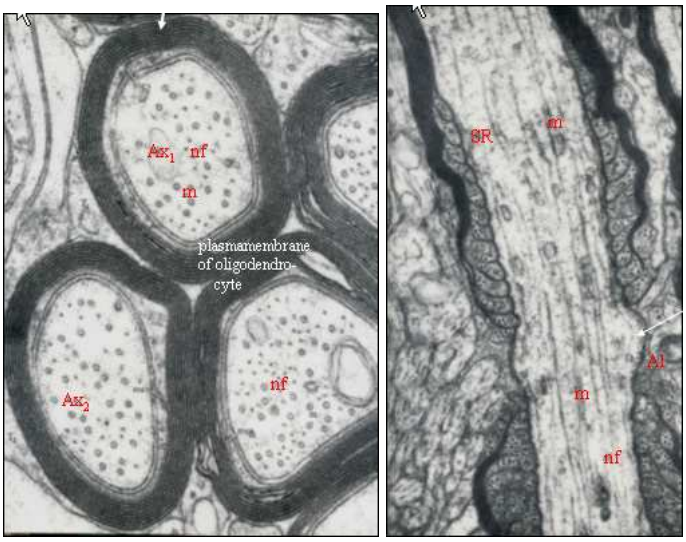

Figure 1.5: Diffusion barriers and ultrastructure of myelinated nerve fibers. A is short for axon, m for microtubulus, nf for neurofilaments, SR for smooth endoplasmatic reticulum and Al for axolemma. The images are taken from Peters *et al.* [4].

cient to give rise to anisotropy. This initial observation of anisotropy in the intact non-myelinated garfish olfactory nerve has subsequently been confirmed in various other models with non-myelinated neural fibers both *in vitro* and *in vivo* [5]. Moreover, in a report by Gulani *et al.* [6] diffusion tensor micro-imaging of the spinal cord in an X-linked recessive Wistar rat mutant, which shows near total lack of myelination in its central nervous system, shows that myelination of white matter is not a requirement for the presence of significant anisotropic diffusion. The anisotropy decreased only by about twenty percent in the myelin deficient rats relative to healthy rats and signified that the residual structures, namely the membranes of the numerous axons, are sufficient for anisotropic diffusion in this model. However, the myelin deficit did alter the absolute ADC values. The increased water mobility was more prevalent in the perpendicular direction than in the parallel. Hüppi *et al.* [7] and Neil *et al.* [8] showed respectively diffusion anisotropy in non-myelinated fibers of the corpus callosum and anterior limb of the internal capsule in humans. Therefore *anisotropic water diffusion in neural fibers must not be regarded as myelin specific*, and the packed arrangement of non-myelinated axons is sufficient to impede perpendicular water diffusion and generate anisotropy [9, 10, 11, 12, 13]. Gulani *et al.* [6] pointed out that myelination can modulate the degree of anisotropy. Because direct comparisons of anisotropy between unique fibers with different axon diameters, degree of myelination and fiber packing density are difficult, a quantitative or qualitative determination of the relative importance of myelin, relative to the axonal membranes are

difficult to assess. Thus for two given fiber tracts with equally sized axons and density, one with myelin and one without, it would still be predicted that myelin would increase anisotropy due to greater hindrance to intra-axonal diffusion and greater tortuosity for extra-axonal diffusion. Pierpaoli *et al.* [14] had also difficulty in attributing particular micro-structural features to explain the variability in diffusion anisotropy observed amongst different white matter tracts in the adult human brain. Sakuma *et al.* [15] observed that anisotropy increases with brain development in neonates. However, there are questions as to whether this signifies myelination and/or just improved coherence of the fiber tracts.

1.2.2 Neurofibrils and fast axonal transport

Inside the axons is the complex and dense three-dimensional cytoskeleton. It is composed of longitudinally oriented and cylindrically shaped neurofibrils. These are microtubules and neurofilaments, inter-connected by small microfilaments. If the small and numerous neurofibrils presented sufficient physical barriers to hinder perpendicular water diffusion to a greater extent than parallel, these structures could presumably cause anisotropic diffusion. In addition, fast axonal transport is intimately linked to the presence of microtubules since cellular organelles (e.g. mitochondria and vesicles) are transported by their attachment to mechanochemical enzymes that pull the organelles along the microtubules tracks. Beaulieu

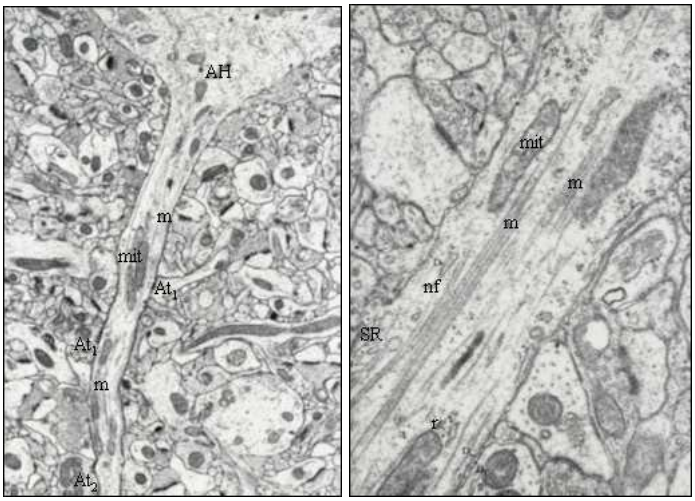

Figure 1.6: Diffusion barriers and axoplasmatic ultrastructure. D is short for dense undercoating, m for microtubules, mit for mitochondrion, nf for neurofilaments, SR for smooth endoplasmatic reticulum, D for dense layer, r for ribosomes, Al for axolemma, AX for axon hillock and At for axon-terminal. The images are taken from Peters *et al.* [4].

and Allen [5] evaluated the role of microtubules and fast axonal transport in

anisotropic diffusion by treating excised myelinated and non-myelinated nerves of the garfish with vinblastine. Vinblastine is known to depolymerize microtubules and inhibit fast axonal transport. The authors demonstrated that anisotropy was preserved in all three types of nerve treated with vinblastine suggesting that microtubules, of themselves, and the fast axonal transport they facilitate are not the dominant determinants of anisotropy. However, all three vinblastine-treated nerves demonstrated absolute ADC decreases of approximately 30-50 percent in both the parallel and perpendicular directions relative to the freshly excised nerves. This finding was attributed to either an increase in free tubulin (the monomeric unit of microtubules), the presence of vinblastine paracrystals within the axoplasm or some degradation over the 48 hours that the nerves were immersed in vinblastine buffer. In Beaulieu and Allen [16] the influence of the neurofilamentary cytoskeleton on water mobility was evaluated by making measurements in axoplasm with minimal interference from membranes. This is possible by examining the axoplasmic space in the isolated giant axon from squid, because the diameter is much greater than the one-dimensional (root-mean-square) RMS displacement (approximately $11\mu m$)of a water molecule randomly diffusing over typical diffusion times used in NMR studies (approximately $30ms$). The conclusions from this work is that the neurofilaments do not have a significant role in diffusion anisotropy within the axon. This points towards *the importance of myelin and multiple axonal membranes* as the primary determinant of the observed anisotropy in neural fibers.

1.2.3 Local magnetic susceptibility

Anisotropic water diffusion, as measured by MR-DTI, can possibly be caused by local susceptibility-difference-induced gradients in the nerves and white matter. Trudeau *et al.* [17] was the first to evaluate the potential contribution of magnetic susceptibility to white matter anisotropy in an experiment on excised porcine spinal cord at 4.7 T. In their experimental procedure, it was possible to respectively minimize or maximize the background gradients by varying the orientation of the fiber tracts parallel or perpendicular to the static magnetic field B_0. The ADCs measured parallel or perpendicular to the fibers were found to be independent of the fiber orientation relative to B_0. Hence the induced gradients seem not to play a role in the anisotropy of white matter diffusion.

The independence of ADC and anisotropy on susceptibility-induced gradients was also confirmed by Beaulieu and Allen [18]. Four different nerves from garfish and frog was excised and evaluated at 2.35 T by varying the orientation of the fibers relative to the static magnetic field and by eliminating the background gradients through the use of a spin-echo diffusion sequence with a specific bipolar gradient pulse scheme. Clark *et al.* [19] extended this work to human brain white matter *in vivo* at 1.5 T, and found no effect of local magnetic susceptibility

induced gradients on water diffusion.

1.2.4 Concluding remarks on biological causes for diffusion anisotropy

By experimental elimination of the dominating role of fast axonal transport, the axonal cytoskeleton of neurofibrils and microfilaments and local susceptibility-difference-induced gradients, the intact membranes are confirmed to be the primary determinant of anisotropic water diffusion in neural fibers such as brain or spinal cord white matter and nerve-bundles. The available data do not permit the dissection of the individual contributions of myelin and axonal membranes to the degree of anisotropy, but the evidence suggests that myelination, although not necessary for significant anisotropy, can modulate the degree of anisotropy.

1.3 Calculation of the diffusion tensor, D

In several earlier studies [5, 16, 18, 19] excised neural fiber samples would be readily oriented parallel or perpendicular to the applied gradients (i.e. the laboratory frame of reference) in order to simplify the measurements of the principal diffusion coefficients. This was done because it obviated the need for calculating the full diffusion tensor and the signal to noise ratio (SNR) was good. Then the ratio of the parallel ADC over the perpendicular ADC is presented as an immediate and intuitive feel for the degree of anisotropy.

The full tensor is needed to calculate the anisotropy for a whole brain *in vivo*.

1.3.1 Stejskal-Tanner equation system

Magnetic resonance diffusion tensor imaging (MR-DTI) ([20], [21]) is sensitive to molecular displacement along the axis of the diffusion-sensitizing gradients applied in a standard Stejskal-Tanner pulsed-gradient spin-echo (PGSE) experiment [22]. Therefore, diffusion along different directions in tissue can be readily evaluated by varying the direction of the diffusion-sensitizing gradients.

In DTI, image intensities are related to the relative mobility of endogenous tissue water molecules. From diffusion measurements in several directions a diffusion tensor is calculated for each voxel. The tensor describes the local water diffusion. To accomplish this, the Stejskal-Tanner imaging sequence [22] is typically used. The Stejskal-Tanner sequence uses two strong gradient pulses, symmetrically positioned around a 180° refocusing pulse allowing for controlled diffusion weighting, see figure 1.7. The first gradient pulse induces a phase shift for all

spins and the second gradient pulse reverses it. Thus the phase shift will be canceled for static spins. But for spins that have completed a change of location due to Brownian motion during a time period Δ, the phase shift will be different for the two gradient pulses. This means that the gradient pulses are not completely refocused, which consequently results in a signal loss. The principles of MR-DTI is described in more detail in appendix D. To eliminate the dependence of T1 and T2 relaxation and spin density, at least two independent measurements of diffusion weighted images must be taken. The images must be differently sensitized to diffusion but remain identical in all other respect. To manage that, one measurement without diffusion weighting and one with diffusion weighting is typically used to calculate diffusion with the following equation [22]

$$S = S_0 e^{-bD} \tag{1.1}$$

Here D is the diffusion constant in the voxel, S_0 is the observed signal intensity without diffusion weighting (i.e. b=0) and S is the observed signal intensity with diffusion weighting. The amount of diffusion weighting is given by the so-called b-factor, introduced by Le Bihan *et al.* [23] and is defined as:

$$b = \gamma^2 \delta^2 \left(\Delta - \frac{\delta}{3} \right) |\mathbf{G}|^2 \tag{1.2}$$

where γ is the proton gyro magnetic ratio (42 MHz/Tesla for water proton spin), $|\mathbf{G}|$ is the strength (i.e. area) of the diffusion sensitizing gradient pulses and Δ is the time between diffusion gradient pulses. The diffusion constant D with unit

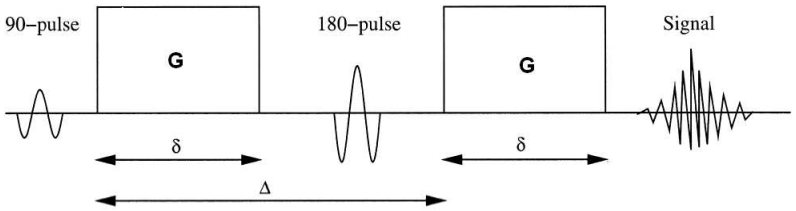

Figure 1.7: The Stejskal-Tanner imaging sequence, see text for explanations.

$[m^2/s]$, is also known as ADC (Apparent Diffusion Coefficient). The term apparent is used to take into account that it is not a true measure of the "intrinsic" diffusion, but rather that the diffusion parameter depends on the interactions of the diffusing water molecules with the tissue micro-structures in the volume element (voxel) over a given diffusion time. It also emphasizes that the diffusion parameter generated from this procedure depends on the experimental conditions such as the direction **g** of the sensitizing gradient **G**. In the case of anisotropic diffusion

Eq. (1.1) has to be written in a more general form,

$$S = S_0 e^{-\gamma^2 \delta^2 [\Delta - (\delta/3)] \mathbf{g}^T \mathbf{D} \mathbf{g}} \tag{1.3}$$

Remember that under the assumption that the probability of molecular Brownian motion follows a multivariate Gaussian distribution over the observation time, the diffusion can be described by a 3×3 tensor matrix, proportional to the variance/co-variance of the Gaussian distribution. The diffusion tensor $\mathbf{D}$ is characterized by nine elements:

$$\mathbf{D} = \begin{bmatrix} D_{xx} & D_{xy} & D_{xz} \\ D_{yx} & D_{yy} & D_{yz} \\ D_{zx} & D_{zy} & D_{zz} \end{bmatrix} \tag{1.4}$$

. Here the diagonal elements D_{xx}, D_{yy} and D_{zz} define the diffusion constants along the x, y and z-axes of the laboratory frame of reference, and the off-diagonal elements D_{ij} represents the effect of a concentration gradient along one axis i on the diffusive displacement along an orthogonal axis j. For water the diffusion tensor is symmetric such that $D_{ij} = D_{ji}$ for $i, j = x, y, z$. Accordingly, the water diffusion tensor $\mathbf{D}$ is completely defined by the six elements: D_{xx}, D_{yy}, D_{zz}, D_{xy}, D_{xz} and D_{yz}.

The formula in Eq. (1.3) reverts to the isotropic case (Eq. (1.1)) with $\mathbf{D} = D\mathbf{I}$, where $\mathbf{I}$ is the identity matrix. By inserting normalized gradient vectors, $\hat{\mathbf{g}} = \mathbf{g}/|\mathbf{g}|$, we can write equation (1.3) using LeBihan's b-factor Eq.(1.2) as

$$S = S_0 e^{-b \hat{\mathbf{g}}^T \mathbf{D} \hat{\mathbf{g}}} \tag{1.5}$$

In addition to the baseline image S_0, there is thus a need for at least six measurements, using different non-collinear gradient directions, to estimate the symmetric 3×3 diffusion tensor $\mathbf{D}$. Therefore, at least seven images with different diffusion weightings and gradient directions need to be collected for each slice in the data set. Figure 1.8 shows an example of a dataset with seven measurements with the corresponding diffusion sensitizing gradient directions, where $\{S_0, S_1, \ldots, S_6\}$ represents the signal intensities in the presence of the gradients $\mathbf{g}_k$ for $k \geqq 6$. S_0 is the signal intensity in the absence of a diffusion-sensitizing field gradient ($|\mathbf{g_0}| = 0$), which is the baseline measurement to which the remaining measurements S_k can be related. By inserting the gradients $\mathbf{g}_k$ and the signals $\{S_k\}$ into Eq. (1.3) we have

$$S_k = S_0 e^{-b \hat{\mathbf{g}}_k^T \mathbf{D} \hat{\mathbf{g}}_k} \tag{1.6}$$

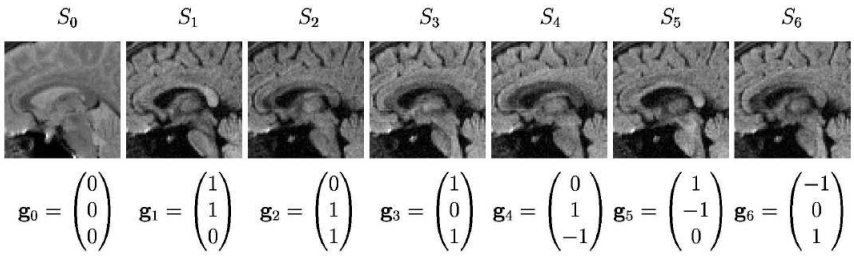

Figure 1.8: Examples of sagittal diffusion measurements with corresponding magnetic field gradients used for diffusion weighting. Courtesy of Skare [24].

It is now possible to calculate the full tensor from this system of equations:

$$\begin{aligned}
ln(S_1) &= ln(S_0) - b\hat{\mathbf{g}}_1^T \mathbf{D}\hat{\mathbf{g}}_1,\\
ln(S_2) &= ln(S_0) - b\hat{\mathbf{g}}_2^T \mathbf{D}\hat{\mathbf{g}}_2,\\
ln(S_3) &= ln(S_0) - b\hat{\mathbf{g}}_3^T \mathbf{D}\hat{\mathbf{g}}_3,\\
ln(S_4) &= ln(S_0) - b\hat{\mathbf{g}}_4^T \mathbf{D}\hat{\mathbf{g}}_4,\\
ln(S_5) &= ln(S_0) - b\hat{\mathbf{g}}_5^T \mathbf{D}\hat{\mathbf{g}}_5,\\
ln(S_6) &= ln(S_0) - b\hat{\mathbf{g}}_6^T \mathbf{D}\hat{\mathbf{g}}_6.
\end{aligned} \tag{1.7}$$

By solving this equation system for each voxel in the data set (note that all $\mathbf{g}_k$ column vectors are given by the sequence definition), it is possible to get the final diffusion tensor field.

1.3.2 A least squares estimation method

For more than six diffusion sensitizing directions, $\mathbf{g}_1,\ldots,\mathbf{g}_k,\ldots,\mathbf{g}_K$ for $K > 6$ a least-squares estimation method for obtaining the diffusion tensor **D** is the obvious choice. Below we give a short description, generalizing simple linear regression in 2D.

Simple Linear Regression

Let us look at a 2D example first. Say we have a linear relationship, representing a straight line, between x and y, $y = \beta_1 + \beta_2 x$, where the coefficients β_1 and β_2 are unknown. Moreover, the independent variable x (and the dependent variably y) are typically hampered with uncertainty, i.e. stochastic variables. Since a straight line can be determined by two arbitrary points along that line, it is obviously sufficient to let only two arbitrary observations (x_1, y_1) and (x_2, y_2) determine β_1 and β_2. If we then do a third observation, this point (x_3, y_3) will probably not lay directly on

that straight line. The problem is, how are we going to take into consideration the third point, which do not lay on the line but none the less is as important as the two other points in determining β_1 and β_2

Usually, it is not the case that the three points $(x_1,y_1),(x_2,y_2),(x_3,y_3)$ lay directly on the straight line. In least squares linear regression, we want the line is positioned (determined from β_1 and β_2) in such a way that the sum of squares:

$$\begin{aligned} Q(\beta_1,\beta_2) &= \sum_{i=1}^{n} \left(y\,(\text{observed}) - y\,(\text{on the line})\right)^2 \\ &= \sum_{i=1}^{n} (y_i - \hat{y}_i)^2 \\ &= \sum_{i=1}^{n} (y_i - \beta_1 - \beta_2 x_i)^2 \end{aligned} \tag{1.8}$$

is minimal. By differentiating the sum of squares as a function of β_1 and β_2 and setting them to zero

$$\begin{aligned} \frac{\partial Q}{\partial \beta_1} &= 0 \\ \frac{\partial Q}{\partial \beta_2} &= 0 \end{aligned} \tag{1.9}$$

we obtain the system of equations:

$$\begin{aligned} n \cdot \beta_1 + \sum_{i=1}^{n} x_i \cdot \beta_2 &= \sum_{i=1}^{n} y_i \\ \sum_{i=1}^{n} x_i \cdot \beta_1 + \sum_{i=1}^{n} x_i^2 \cdot \beta_2 &= \sum_{i=1}^{n} x_i y_i \end{aligned} \tag{1.10}$$

which has the solution:

$$\begin{aligned} \hat{\beta}_2 &= \frac{\sum_{i=1}^{n} (x_i - \bar{x}) y_i}{\sum_{i=1}^{n} (x_i - \bar{x})^2} \\ \hat{\beta}_1 &= \bar{y} - \hat{\beta}_2 \bar{x} \end{aligned} \tag{1.11}$$

When $n = 2$ we obtain the solution for a straight line through two points. In statistics we usually employ the formalism of vectors and matrices:

$$\begin{aligned} \mathbf{y} &= X\beta + \mathbf{e} \\ Q &= |\mathbf{y} - X\beta|^2 \\ &= (\mathbf{y} - X\beta)^T (\mathbf{y} - X\beta) \end{aligned} \tag{1.12}$$

Here $\mathbf{y} = (y_1, \ldots, y_K)^T, \beta = (\beta_1, \beta_2)^T$ and X is the $K \times 2$ matrix where all the elements in the first column is 1 and the elements in the second column is $(x_1, \ldots, x_K)^T$. The solution of this problem is given by the *normal equations*

$$X^T X\beta \quad = X^T \mathbf{y} \quad \Leftrightarrow \quad X^T (\mathbf{y} - X\beta) = 0 \quad \Rightarrow \quad \hat{\beta} = \left(X^T X\right)^{-1} X^T \mathbf{y} \quad (1.13)$$

The last formula assumes that X has full rank.

Least square estimation method applied to the diffusion tensor

Now we want to do something analogously for the diffusion tensor. Assume we have measurements/observations S_k for $k = 0, \ldots, K; \quad K \geqq 6$. We then calculate

$$y_k = \frac{1}{b} \log \frac{S_0}{S_k} \quad (1.14)$$

If every observation was without errors and the diffusion model was exact, we should have had

$$y_k = \mathbf{g}_k^T \mathbf{D} \mathbf{g}_k = \sum_{i=1}^{3} \sum_{j=1}^{3} g_k^i D_{ij} g_k^j = \gamma_k^T \delta; \qquad k = 1, \ldots, K \quad (1.15)$$

where γ_k^T is denotes the direction of the diffusion sensitizing gradient and $\delta = (D_{11}, \ldots, D_{33})^T$. When $K = 6$ this gives us six equations to determine the six unknown elements in the 3×3 *symmetric* matrix $\mathbf{D}$. If $K > 6$, we will have too many equations. As for the straight line in section 1.3.2 this takes away the possibility to determine the tensor $\mathbf{D}$ exact. Instead we seek the values for the unknown that minimizes the square sum:

$$\begin{aligned} Q &= \sum_{k=1}^{K} \left(y_k - \mathbf{g}_k^T \mathbf{D} \mathbf{g}_k\right)^2 = \sum_{k=1}^{K} \left(y_k - \gamma_k^T \delta\right)^2 \\ &= (y - \Gamma\delta)^T (y - \Gamma\delta) \\ &= y^T y - 2\delta^T \Gamma^T y + \delta^T \Gamma^T \Gamma \delta \end{aligned} \quad (1.16)$$

where $y = (y_1, \ldots, y_K)^T$, $\Gamma = (\gamma_1, \ldots, \gamma_K)^T$ and $\delta = (D_{11}, \ldots, D_{33})^T$.

Now we will minimize Q with respect to δ under the condition that δ corresponds to a symmetric 3×3 matrix D. We will differentiate Q with respect to δ.

$$\frac{dQ}{d\delta} = 0 \quad (1.17)$$

Since γ_k corresponds to a symmetric matrix G_k, this means that column number four, seven and eight are superfluous and can be deleted. The rank of Γ will then

be six if the choice of diffusion sensitizing directions has been wise. If these columns in Γ are deleted it is important to delete element number four, seven and eight in δ. Let us assume that the reduction has been done. Then we have a matrix Γ with full rank and the solution will be:

$$\hat{\delta} = \left(\Gamma^T \Gamma\right)^{-1} \Gamma^T y \tag{1.18}$$

It is important to note that the elements δ that corresponds to non-diagonal elements in the matrix D are paired such that $\delta_2 = D_{12} + D_{21} = 2D_{21}$.

The method described above has been implemented in MATLAB to solve the diffusion tensor for each voxel in the brain imaging volume. See appendix B for details of the program.

1.3.3 Scalar rotationally invariant measures derived from the diffusion tensor

This leaves us with a diffusion tensor that looks like this in each voxel:

$$\mathbf{D} = \begin{bmatrix} D_{xx} & D_{xy} & D_{xz} \\ D_{yx} & D_{yy} & D_{yz} \\ D_{zx} & D_{zy} & D_{zz} \end{bmatrix} \tag{1.19}$$

In figure 1.9, the tensor for all voxels in slice #12 of subject JL is visualized. It

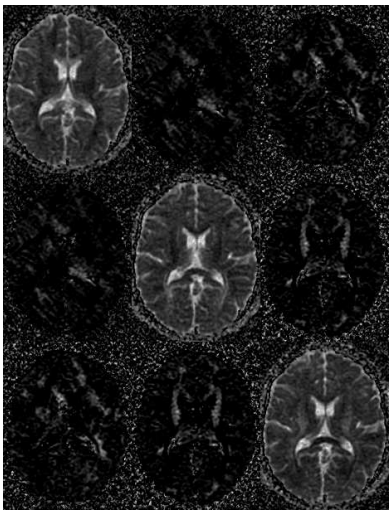

Figure 1.9: Visualization of the tensor. Data from subject JL.

gives little understanding to present the tensor data as tensor components. Instead

the six-dimensional diffusion tensor information is mapped to different scalar measures that gives a physically meaningful picture depicted as a grey scale map. The rotationally invariance of the scalars means that these measures are independent of the orientation of both tissue structure and the image scan plane. Images which depict rotationally invariant measures will have the same intensity for the same anatomical location regardless of the orientation of tissue (patient) in the scanner and of the image scan plane. In contrast, neither the elements in the diffusion tensor nor a diffusion-weighted image measured along one single direction is rotationally invariant.

Below follows a description of some types of scalar measures calculated from the diffusion tensor, used in the experimental part of this thesis.

Mean diffusivity

In section 1.1.4 we depicted the RMS displacement (iso-probability surfaces) for three different diffusion ellipsoids. The mean diffusivity denoted $\langle \mathbf{D} \rangle$ is when the average of the radii of the ellipsoid is used as a scale factor of the diffusion ellipsoid. As an example the $\langle \mathbf{D} \rangle$ in CSF (cerebrospinal fluid) is three times bigger than the $\langle \mathbf{D} \rangle$ in grey and white matter. The values are $2 \times 10^{-3} mm^2/s$ for CSF and $0.7 \times 10^{-3} mm^2/s$ in grey and white matter. The $\langle \mathbf{D} \rangle$ happens to be similar in grey and white matter despite the fact that the diffusion is more anisotropic in white than in grey matter. The $\langle \mathbf{D} \rangle$ can be calculated simply by averaging the diagonal elements of the diffusion tensor.

$$\langle \mathbf{D} \rangle = \frac{D_{xx} + D_{yy} + D_{zz}}{3} = \frac{Trace(\mathbf{D})}{3} \tag{1.20}$$

Maps which pixels represent the mean diffusivity $\langle \mathbf{D} \rangle$ is often called trace-maps.

Diffusion anisotropy

There are several other scalar measures that describes the *anisotropy* of the diffusion. Many of them are summarized in Skare *et al.* [25]. Common to all of them are that they depend on how anisotropic the diffusion actually is. That is, how much the diffusion ellipsoid deviates from a sphere. Simultaneously the anisotropy indices should be rotationally invariant which means that they should be independent of the orientation of the diffusion ellipsoid. The diffusion anisotropy indices are calculated from the *eigenvectors* and the corresponding *eigenvalues* of the diffusion tensor. This is done by solving the characteristic

equation.

$$\begin{aligned} det\,(\mathbf{D}-\lambda\mathbf{I}) &= det\left(\begin{bmatrix} D_{xx} & D_{xy} & D_{xz} \\ D_{xy} & D_{yy} & D_{yz} \\ D_{xz} & D_{yz} & D_{zz} \end{bmatrix} - \begin{bmatrix} \lambda & 0 & 0 \\ 0 & \lambda & 0 \\ 0 & 0 & \lambda \end{bmatrix}\right) \\ &= det\begin{bmatrix} D_{xx}-\lambda & D_{xy} & D_{xz} \\ D_{xy} & D_{yy}-\lambda & D_{yz} \\ D_{xz} & D_{yz} & D_{zz}-\lambda \end{bmatrix} = 0 \end{aligned} \tag{1.21}$$

This results in three eigenvectors $\mathbf{e}_i$ and three eigenvalues λ_i for $i = 1,2,3$; i.e. equation ((1.22)) yields:

$$\begin{aligned} &\mathbf{Ae_1} = \lambda_1\mathbf{e_1}, \quad \mathbf{Ae_2} = \lambda_2\mathbf{e_2}, \quad \mathbf{Ae_3} = \lambda_3\mathbf{e_3}; \\ &\mathbf{e_i} \neq [0,0,0]^T; \quad \lambda_1 \geq \lambda_2 \geq \lambda_3 \in \Re. \end{aligned} \tag{1.22}$$

After the eigenvalues of the tensor has been calculated, rotationally invariant anisotropy indices, which are no longer dependent on the orientation of the tensor, can be constructed. An intuitive definition of an anisotropy index is the ratio between the largest (λ_1) and the smallest (λ_3) eigenvalue, i.e.

$$A_{ratio} = \frac{\lambda_1}{\lambda_3} \tag{1.23}$$

A_{ratio} is equal to 1 if the diffusion tensor is isotropic. That is so because then $\lambda_1 = \lambda_2 = \lambda_3$. However A_{ratio} is numerically unstable and predisposed for noise. A more stable anisotropy index is the **relative anisotropy** index, *RA*, defined as:

$$RA = \frac{1}{\sqrt{6}} \frac{\sqrt{\sum\limits_{i=1,2,3} \left(\lambda_i - \bar{\lambda}\right)^2}}{\lambda} \text{ where } \qquad \bar{\lambda} = \frac{1}{3}\sum_{i=1}^{3} \lambda_i \tag{1.24}$$

The numerator is the standard deviation of the eigenvalues except for the scale factor of $1/\sqrt{2}$. The denominator is the mean diffusivity and is used to normalize with the size of the ellipsoid. Therefore *RA* represents the ratio of the anisotropic and the isotropic part of **D**. *RA* will be zero for isotropic diffusion and approach 1 when $\lambda_1 \gg \lambda_2 \approx \lambda_3$. It is important to note that the normalization factor in Eq. (1.24) differs from the original definition where the maximum value for *RA* is $\sqrt{2}$.

For the presentation of diffusion anisotropy as a grey scale map, the scale factor is of no importance. But it is preferred that one uses the same scale reaching from 0 to 1 while clearly stating the anisotropy index used when reporting anisotropy values in literature. Otherwise it will be harder to compare results and draw conclusions.

Another commonly used anisotropy index, which is also used in the experiments reported in this thesis, is the **fractional anisotropy** index *FA*. *FA* is defined as follows:

$$FA = \sqrt{\frac{3}{2}\frac{\sum_{i=1,2,3}\left(\lambda_i - \overline{\lambda}\right)^2}{\sum_{i=1,2,3}\lambda_i^2}} \text{ where } \qquad \overline{\lambda} = \frac{1}{3}\sum_{i=1}^{3}\lambda_i \tag{1.25}$$

FA measures the fraction of the total magnitude of **D** that can be ascribed to anisotropic diffusion and thus provides information about the shape of the diffusion tensor at each voxel [26]. The FA is based on the normalized variance of the eigenvalues. A FA value of "0" corresponds to a perfect sphere (i.e. $\lambda_1 = \lambda_2 = \lambda_3 = \lambda$), whereas 1 represents ideal linear diffusion (i.e. $\lambda_1 = \lambda, \lambda_2 = \lambda_3 = 0$). Well defined tracts have FA larger than 0.20. Few regions have FA larger than 0.90. The number gives us information of how asymmetric the diffusion is but says nothing of the direction. See figure 1.10 for a depiction of an FA map.

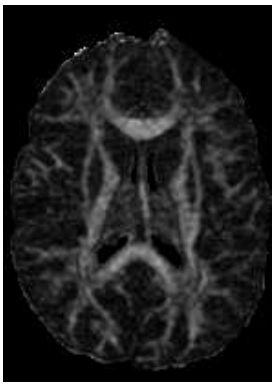

Figure 1.10: Fractional anisotropy map for subject OB and slice number 12.

Different anisotropy indices have slightly different physical interpretations and several groups have demonstrated that different indices differ in how strongly they are affected by image noise. For *mean* see [27], for *Trace(***D***)* see [28], [29], for *RA* see [30] and [25], for *FA* see [27], [30] and [25].

1.4 Motivation and problem formulation for this thesis

The signal in MR-DTI is both weak and vulnerable to noise and artifacts, such that the determination of the diffusion tensor **D** and the FA-index are subject to uncertainty and errors. There are several methods that can be applied during acquisition to improve the signal strength and reduce noise i.e. increase the signal to noise ratio. Two of them are:

1. increasing the number of diffusion sensitizing gradient directions
2. increasing the number of excitations used for averaging (NEX).

However both of these leads to an increase in the acquisition time, and which one is better is not generally known and partly scanner and sequence dependent. In this work we wanted to explore the potentially significant differences between DTI head acquisitions obtained along the two different types of schemes denoted (1.) and (2.) below.

For a fixed number of measurement time (e.g. 6-7 minutes),

1. select as many averages (NEX) as possible with as few diffusion sensitizing directions as necessary (e.g. K=6), against
2. select as many diffusion sensitizing directions (K) as possible with as few averages as necessary (e.g. NEX=1-2).

To study this problem we have used three different DTI acquisition protocols, applied to five different subjects. If we denote K the number of diffusion sensitizing directions and NEX the number of excitations for signal averaging (in k-space), we designed comparative experiments with the following combinations (K=6 and NEX=8), (K=13 and NEX=4) and (K=25 and NEX=2).

To *evaluate the respective results* we calculated the diffusion tensor **D** using a least square estimation method, see page 14 in section 1.3.2. From the eigensystem of the tensor, FA values were calculated mapping the whole brain. Fractional anisotropy standard deviation and coefficient of variation were calculated in tissue specific regions (GM, WM and CSF). To reveal any directional dependent differences in the FA values, 3D plots were made where the standard deviation of the tissue specific FA values was plotted against the principal direction of diffusion, i.e. the direction of the eigenvector of **D** corresponding to the largest eigenvalue. Finally the FA maps were color-coded with separate colors for the individual elements of the principal diffusion vector and careful inspection were done to visually detect possible differences between the (K=6 and NEX=8), (K=13 and NEX=4) and (K=25 and NEX=2) protocols.

2

Material and Methods

2.1 Subjects

We have performed MR-DTI head examinations of five healthy volunteers, age spanning from 24 to 29 years (mean age = 27 years). These data were used for planning DTI protocols for routine clinical use. All subjects were healthy deemed normal without known CNS pathology, current or past, medical or psychiatric conditions. No medication or substance abuse were reported. For more detailed information, see Table 2.1.

2.2 Scanner and imaging protocol

For DTI data acquisitions we used a General Electric Signa 1.5T Echospeed MR scanner equipped with EPI measurement techniques. Whole brain, multislice DTI acquisitions were performed using 24 axial slices (128x128 acquisition matrix, interpolated to 256x256, FOV=240mm, slice thickness 4mm with no gap). We used b-values 0 (S_0) and $1000 s/mm^2$ (S_k) and different number of diffusion sensitizing directions $K = 6, 13, 25$ and number of excitations (NEX) per direction $\mathbf{g}_k$ for signal averaging, i.e. NEX$= 8, 4, 2$. The repetition times (TR) and echo times (TE) varied slightly for the different protocols (cf. Table 2.1). The total acquisition time for each DTI protocol lasted between 6 and 7 minutes (cf. Table 2.2). One

additional subject (TN) was scanned on a Siemens Symphony 1.5T scanner with $K = 6$ and $K = 12$ for fixed NEX=8 to assess the effect of increasing signal to noise ratio on the diffusion tensor.

Subject parameters

Subject	*weight*[*kg*]	*age*	$TR_{6,8}$	$TR_{13,4}$	$TR_{25,2}$	$TE_{6,8}$	$TE_{13,4}$	$TE_{25,2}$
EK	70	28	7400	7560	7400	85.2	85.2	85.2
OB	72	26	7400	7560	7400	85.2	85.2	85.2
JL	76	24	7400	7400	7560	98.8	98.8	98.8
OH	90	29	7400	7400	7560	98.6	98.6	98.6
SA	86	28	7400	7400	7560	100.6	100.6	100.6

Table 2.1: TR is repetition time, TE is echo time (both in [ms]), the subscripts 6, 8, 13, 4, 25 and 2 refers to the number of diffusion sensitizing directions and number of excitations in the three experimental setups (6 and 8, 13 and 4, 25 and 2).

Acquisition times

	6dir 8NEX	13dir 4NEX	13dir 5NEX	25dir2NEX
OB	7:09	7:18		6:39
EK	7:09		9:04	6:39
JL	7:09	7:18		6:39
OH	7:09	7:18		6:39
SA	7:09	7:18		6:39

Table 2.2: Acquisition times for the five subjects and the respective sequences.

Diffusion sensitizing directions

The spatial directions of the diffusion sensitizing gradients $\mathbf{g}_1, \ldots, \mathbf{g}_K$ are given in table 2.3. This information was obtained from files “deep” in the pulse sequence software on the GE scanner and follows the optimal choise of diffusion sensitizing directions proposed by Jones [31].

Software

Several programs and software tools (mostly MATLAB) have been used in this project. See Appendix A for details.

	6 dirs.			13 dirs.			25 dirs.		
#	x	y	z	x	y	z	x	y	z
1	0.707	0.000	0.707	-0.754	0.173	-0.633	0.532	0.104	-0.840
2	-0.707	0.000	0.707	0.330	-0.372	0.867	0.250	-0.722	0.645
3	0.000	0.707	0.707	-0.533	0.459	0.711	-0.634	-0.753	-0.177
4	0.000	0.707	-0.707	-0.687	-0.708	-0.163	-0.219	0.850	0.478
5	0.707	0.707	0.000	-0.321	0.942	-0.101	-0.413	-0.780	0.470
6	-0.707	0.707	0.000	0.618	0.786	-0.018	0.734	-0.662	0.151
7				0.019	0.576	0.817	0.936	0.054	0.347
8				0.311	-0.949	0.051	-0.333	-0.243	0.911
9				-0.883	0.314	0.350	0.103	-0.992	-0.077
10				-0.038	-0.536	-0.843	-0.927	0.373	-0.049
11				0.184	0.469	-0.864	0.801	0.543	-0.250
12				0.937	0.004	0.350	-0.917	-0.262	0.301
13				0.814	-0.236	-0.531	-0.538	0.438	-0.720
14							-0.214	-0.665	-0.716
15							-0.124	-0.052	-0.991
16							0.274	0.960	-0.053
17							-0.443	0.878	-0.180
18							0.024	0.369	0.929
19							0.568	0.637	0.521
20							0.931	-0.168	-0.324
21							-0.825	-0.182	-0.534
22							0.473	-0.630	-0.617
23							0.504	-0.129	0.854
24							0.149	0.689	-0.709
25							-0.695	0.344	0.631

Table 2.3: This table shows the x-,y- and z-coordinates for the diffusion sensitizing gradient vectors with three decimals using 6, 13 and 25 directions. The values were obtained from the *tensor.dat* file as a part of the GE MR scanner software. Note that the vectors are normalized, i.e. $\sqrt{x^2+y^2+z^2} = 1$.

2.3 Data analysis

2.3.1 Image format conversion

The acquisition data from the MR-scanner is stored as files in DICOM format. To work with these data sets in MATLAB and SPM2 the images have to be converted to other formats. A DTI dataset typically contains one image for every diffusion sensitizing direction and one image without diffusion weighting per slice. Using $K = 6$ diffusion sensitizing directions and 24 slices covering the whole brain, our dataset will contain $(6+1)\cdot 24 = 168$ images. In MATLAB we wanted to organize the dataset as one single 4D-dti-volume which can be addressed as M[k, row, col, slice] being the signal intensities in diffusion direction $k = 1,\ldots,K+1$, row$= 1,\ldots,256$, column col$= 1,\ldots,256$ and in slice$= 1,\ldots,24$. This is accomplished with a MATLAB script (*loaddti.m*). We have also converted the DICOM data to Analyze format, because this is the image-format SPM2 uses. We used nICE [32] to organize the data in $K+1$ blocks (e.g. one volume of 24 slice for each direction) and saved each block to Analyze-format. Note that the first block is the S_0-volume.

2.3.2 Estimation of D from the image data

The M-data (M[1:K+1, 1:256, 1:256, 1:24]) consists of K+1 image volumes with 24 images (slices) in each. The first volume represents the $b = 0$ acquisition, i.e. S_0 (= the $0'th$ direction). Accordingly, there are K+1 image volumes with a water diffusion measurement S_k for the k'th direction in each voxel (volume element). For each voxel a diffusion tensor **D** was calculated based upon the measurements $S_0, S_1, \ldots, S_K$, for $K \geq 6$, as described in section 1.3.2. The result is a 5D tensor volume **D**[i, j, row, col, slice], where $i = 1,2,3$ is the i'th row-element of the diffusion tensor and $j = 1,2,3$ is j'th column-element. Consequently the tensor **D** is a matrix-valued 3D image volume that contains a 3×3 symmetric matrix in each voxel, see figure 1.9. From the tensor data the eigenvectors $\mathbf{e}_1, \mathbf{e}_2, \mathbf{e}_3$ and the corresponding eigenvalues $\lambda_1 \geq \lambda_2 \geq \lambda_3$ were calculated as described in section 1.1.3 and the equations (1.21) and (1.22).

2.3.3 Computing FA maps

From the water diffusion tensor volume, **D**=**D**[i,j,row,col,slice] a scalar measure for anisotropic diffusion, FA ([26]) (fractional anisotropy), was calculated in each voxel, giving a 3D FA map volume, see section 1.3.3 and figure 1.10 for further explanations and examples.

2.3.4 Tissue specific anisotropy parameters

To make it possible to calculate tissue specific FA values we segmented the DT-MRI images into white matter (WM), grey matter (GM) and cerebrospinal fluid (CSF).

Tissue Segmentation

SPM2 (see section A.3 for more details) was used to segment the T_2-weighted S_0 brain volume into the three tissue types, (see figure 2.1). These three brain volumes are probability masks, i.e. voxels with high probability for a specific tissue will appear as white on the tissue specific image, and reversely, voxels with low probability for a given tissue will appear as dark on the image. To reduce

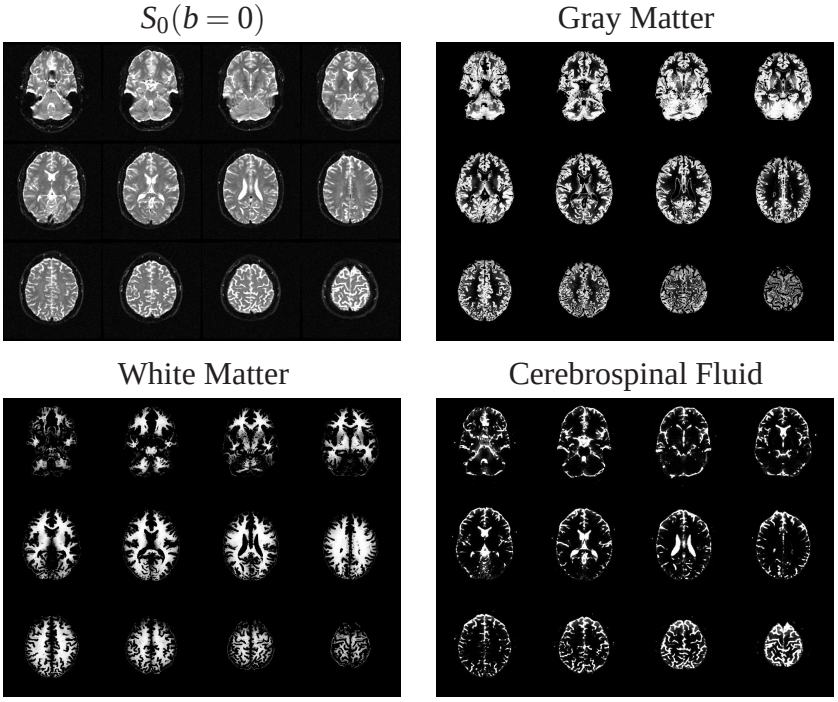

Figure 2.1: The S_0 and the segmented volumes. Data from subject JL.

the number of voxels in which FA is calculated, a threshold value was set. This was done in MATLAB (see Appendix A.1 and B.8). The threshold value in our experiments was set to 0.925 which means that every voxel included in the mask has 92,5 % probability or higher of being the tissue specified.

The collection of voxels in these restricted tissue masks were used for the tissue specific FA calculations.

2.3.5 Standard deviation and CV of tissue specific FA

The first tissue specific parameters being calculated were sample mean, $mean(FA)$, sample standard deviation, $std(FA)$, and coefficient of variation, $cv(FA) = std(FA)/mean(FA)$.

2.3.6 Uncertainty of FA, std(FA|θ and ϕ)

Signal to noise ratio (SNR) and other image degradation are important for the quality of the resulting FA map. One measure of this quality is to assess the directional dependence of the standard deviation of the FA, i.e. $std(FA|\theta,\phi)$ ([24], [33]), where θ and ϕ denote the azimuth- and elevation angles (spherical coordinates), respectively of the principal diffusion direction in a given tissue specific voxel. This is so because the SNR, image degradations and numerical errors might depend on the number of averages (NEX), the selection of directions $\mathbf{g}_k$ and the number of diffusion sensitizing gradients K, being used in the acquisition. Such noise and errors will propagate in the calculation of the eigensystem of the diffusion tensor, and the FA value is directly dependent on the principal diffusion direction (i.e. direction of eigenvector belonging to the largest eigenvalue) at the specific voxel. To obtain sufficient samples in the different directions, we have binned the samples into discrete (θ,ϕ)-values in steps of $\Delta\theta = 15^\circ$ and $\Delta\phi = 15^\circ$, and made surface plots of $std(FA)$ vs. $n\cdot\Delta\theta, m\cdot\Delta\phi$ where n,m ranges from $-6,\ldots,0,\ldots+6$ and $-12,\ldots,0,\ldots,+12$ respectively and θ,ϕ ranges from $-90,\ldots,0,\ldots+90$ and $-180,\ldots,0,\ldots,+180$ respectively (see figure 2.2). Large oscillations in the plot, implies high directional dependency of FA-variation and more severe image degradation, and low variation, a smooth or flat plot, implies higher quality.

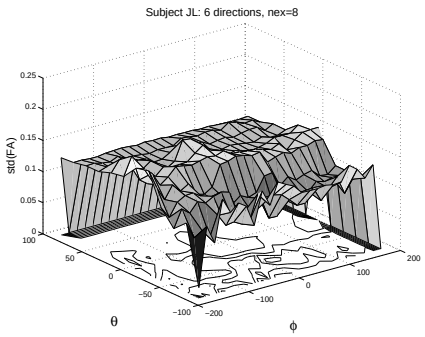

Figure 2.2: A three dimensional plot showing the standard deviation of the FA in white matter for subject JL as a function of the azimuth angle θ and the elevation angle ϕ for the largest eigenvector.

2.3.7 Direction-dependent color-coding of the FA map

It is possible to superimpose directional information on the FA map in terms of color-coding ([34]). This is achieved by letting each of the vector components in the principal eigenvector of a voxel get a separate color (i.e. red, green and blue respectively) and the FA value in the same voxel the strength or saturation of the color. Thus the $e_{1,x}$ element, i.e. right-left direction has the color-code red, $e_{1,y}$, i.e. anterior-posterior direction has the color-code green and $e_{1,z}$, i.e. inferior-superior direction has the color-code blue. When FA is close to zero the strength of the color is weak and when FA is close to one the color strength is strong. Examples of a plain FA map and a corresponding color-coded FA map are shown below in figure 2.3.

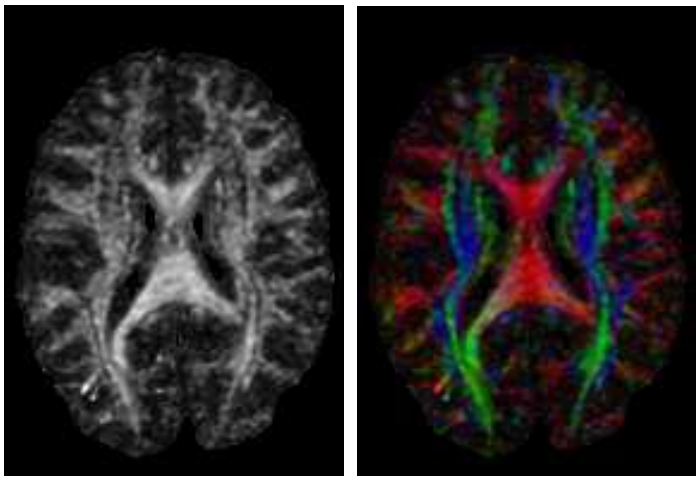

Figure 2.3: FA map to the left and the color-coded map to the right. Data from subject OH K=25 and NEX=2.

The objective of color-coding of the FA map was to reveal if one of the protocols to be compared (cf. section 1.4) was visually better than another.

2.3.8 Eddy current correction

When a diffusion gradient is applied, there is a change in the total magnetic field **B** equivalent to $\partial\mathbf{B}/\partial t$. This change induces an eddy current (EC) ([35]) which in turn induces an extra magnetic field and the resulting Fourier-reconstructed image gets geometrically distorted, and also a little blurred. Since this is dependent on the diffusion sensitizing gradient, the stack of images $S_0, S_1, \ldots, S_K$ might be slightly in mis-registration, i.e. not geometrically aligned, and this will introduce error in the voxel-wise calculations of the diffusion tensor and the FA value. The

eddy current effect causes the diffusion gradient waveform to be smoother than expected. To obtain the desired waveform, *pre-emphasis* is often used. That is, the diffusion gradient is ramped up in a way that compensates for the change.

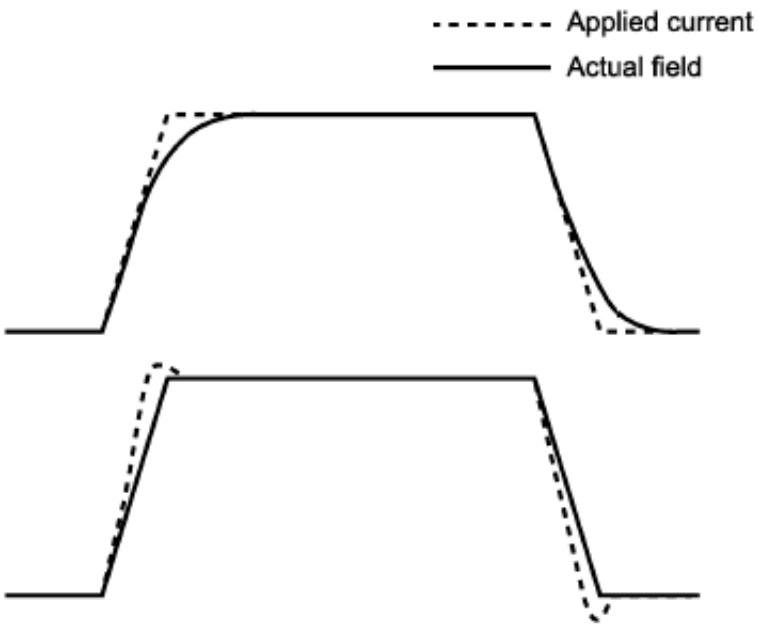

Figure 2.4: Upper part: Eddy current pre-emphasis. The dashed line denotes the current applied in the gradient coil. Due to eddy currents during the ramp times, the actual field gradient obtained differs from the nominal (solid line). Lower part: Employing gradient pre-emphasis the applied current during the ramps is adjusted so that the actual magnetic field gradient becomes close to the nominal shape indicated by the dashed line on the top figure. Courtesy of Skare [24].

Many MR scanner manufacturers have implemented a pre-emphasis system that is not typically sufficient to correct for the ECs induced by the very strong diffusion gradients applied in the EPI sequence. However, some of the eddy current components are approximately constant during the acquisition and will give linear effects. This is possible to correct by post-processing methods on the reconstructed magnitude images. Methods for such geometric correction are implemented in the FSL software package 3.10, which is recently released. For all of our results, correction of such possible geometric distortion due to insufficient EC compensation, was not performed. However, late in the project we used the newly released FSL routines to assess the effect of “EC correction” on one of our data sets (subject OB). The results of this EC correction are described in section 3.10. See also Fig. 2.6.

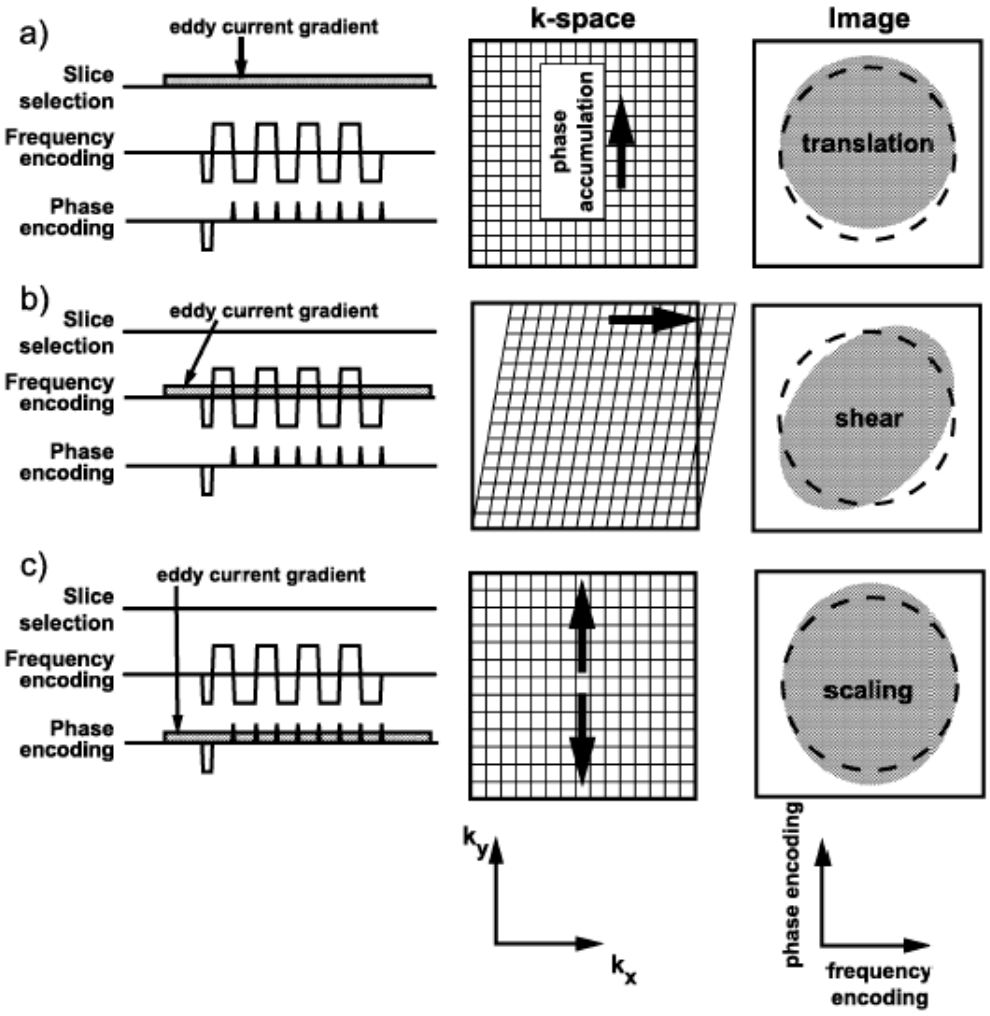

Figure 2.5: Eddy currents (EC) during the EPI readout. a) An EC in the slice selection direction will cause a linear phase shift in the k_y direction in k-space. This corresponds to a shift of the object in the phase encoding direction (here y) in the reconstructed image. b) An EC in the frequency encoding directions will cause the k-space to be sheared resulting in a shear of the object in the image in the phase encoding direction. c) Finally, an EC in the phase encoding direction makes sampling density of k-space to change in the k_y direction. This causes the effective FOV to change in the MR image, which is equivalent to a scaling effect of the object. Courtesy of Skare [24].

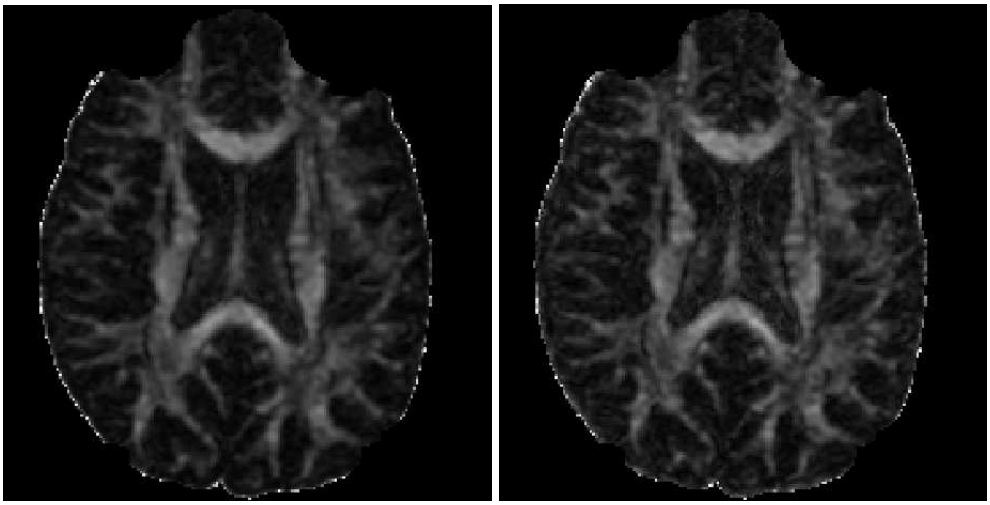

Figure 2.6: The left image shows FA based on geometric eddy current correction and the right image shows FA without eddy current correction. Subject OB with K=25 and NEX=2.

3

Experimental results

3.1 The original DTI acquisitions

In this section we present a selection of original recorded DTI data from five volunteers and graphs and images associated to the various processing steps of our evaluation study. The guiding principle has been to report potentially significant differences between image data obtained along the two extreme situations: for a fixed measurement time, (*i*) select as many averages (NEX) as possible with as few diffusion sensitizing directions as necessary (e.g. 6) and (*ii*) select as many diffusion sensitizing directions as possible with as few averages as necessary (e.g. 1-2).

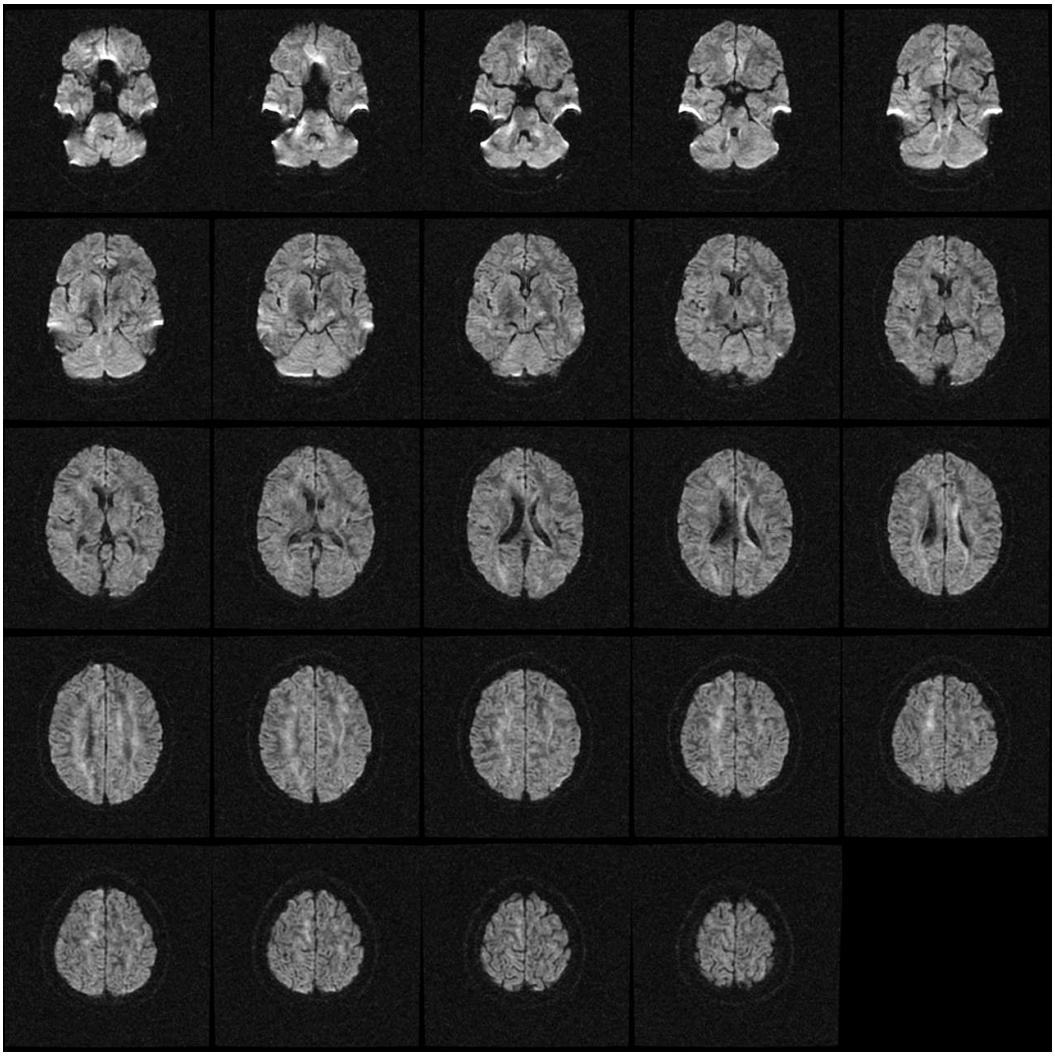

Figure 3.1: Typical diffusion weighted image volume, the diffusion sensitizing gradient vector coordinates are (x,y,z)=(0.707, 0.000, 0.707). Every slice from slice number 1 to 24 is presented. Axial slice direction. Data from subject JL.

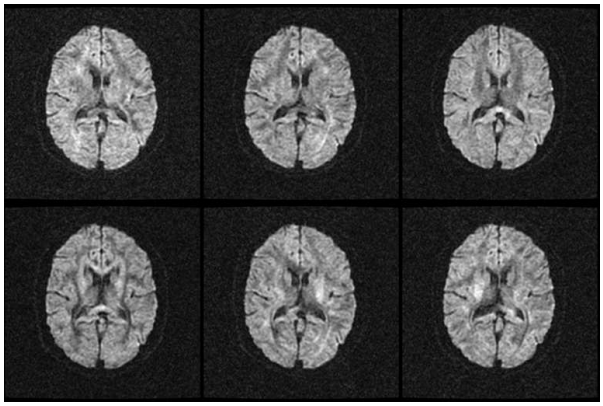

Figure 3.2: Typical diffusion weighted image for 6 diffusion sensitizing directions and 8 NEX, slice number 12 is selected from each volume to save space. Data from subject JL. To see the diffusion sensitizing gradient vector coordinates see table 2.3 page 23.

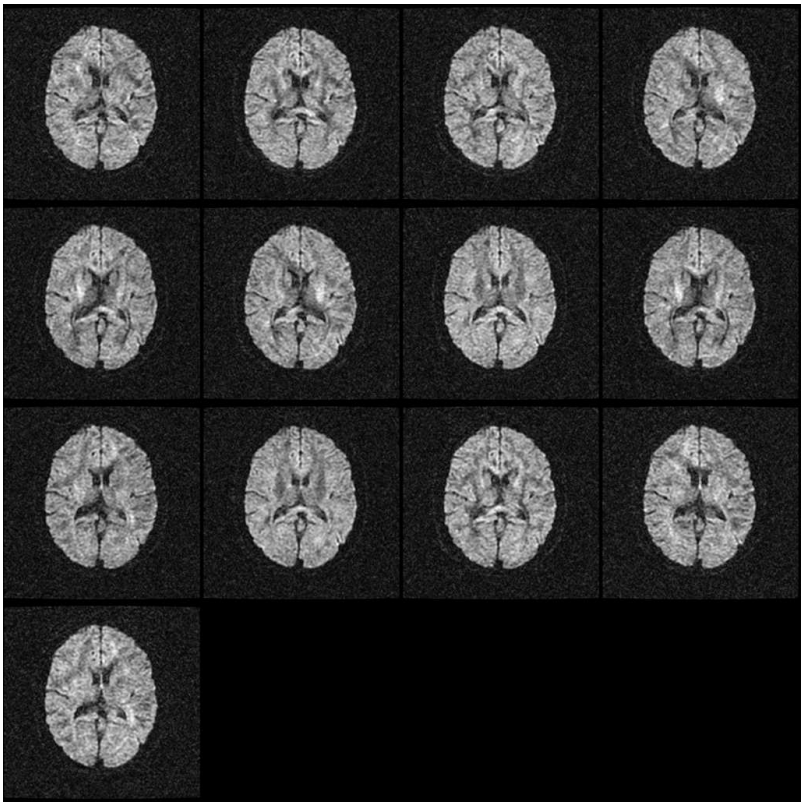

Figure 3.3: Typical diffusion weighted image for 13 diffusion sensitizing directions and 4 NEX, slice number 12 is selected from each volume to save space. Data from subject JL. To see the diffusion sensitizing gradient vector coordinates see table 2.3 page 23.

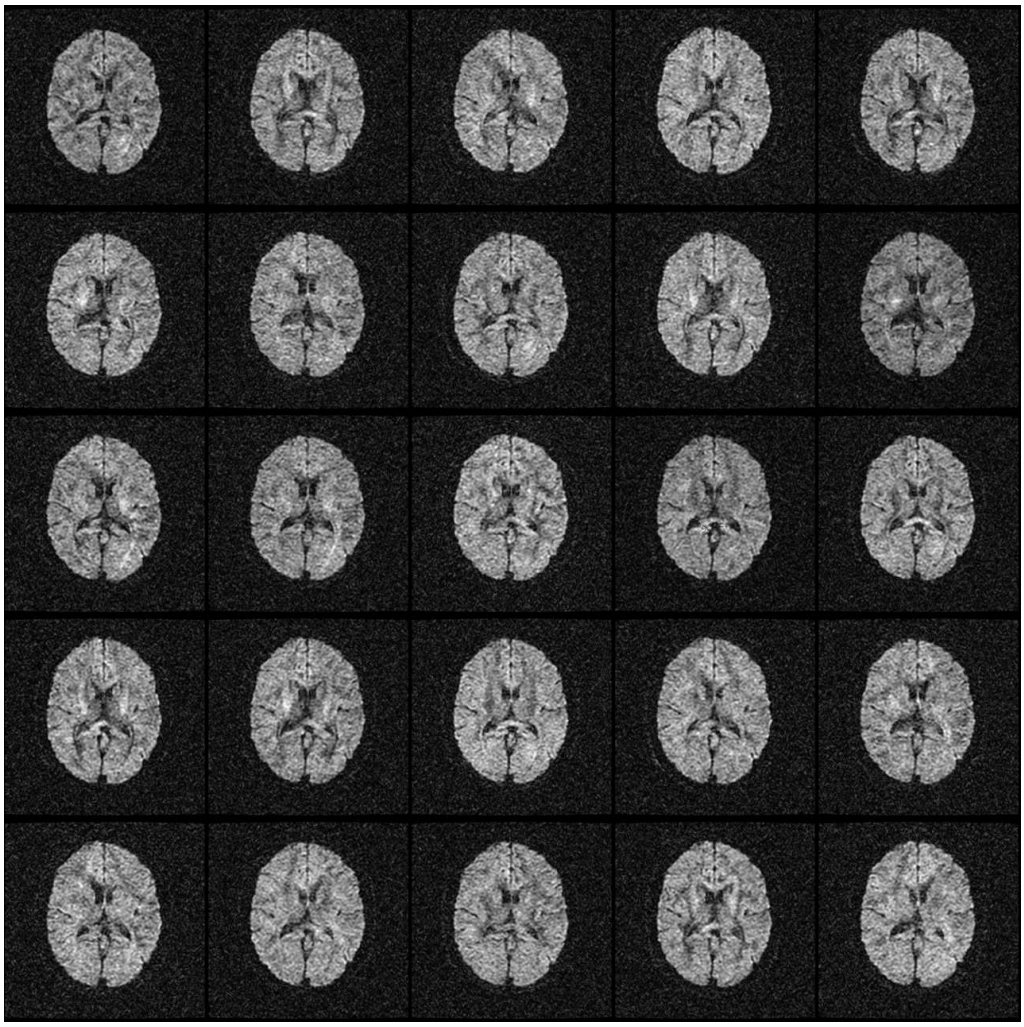

Figure 3.4: Typical diffusion weighted image for 25 diffusion sensitizing directions and 2 NEX, slice number 12 is selected from each volume to save space. Data from subject JL. To see the diffusion sensitizing gradient vector coordinates see table 2.3 page 23.

3.2 Calculated diffusion tensors

One important stage in the processing chain of DTI images is the calculation of the diffusion tensor **D**. The tensors are calculated as described in section 1.3.2 page 14.

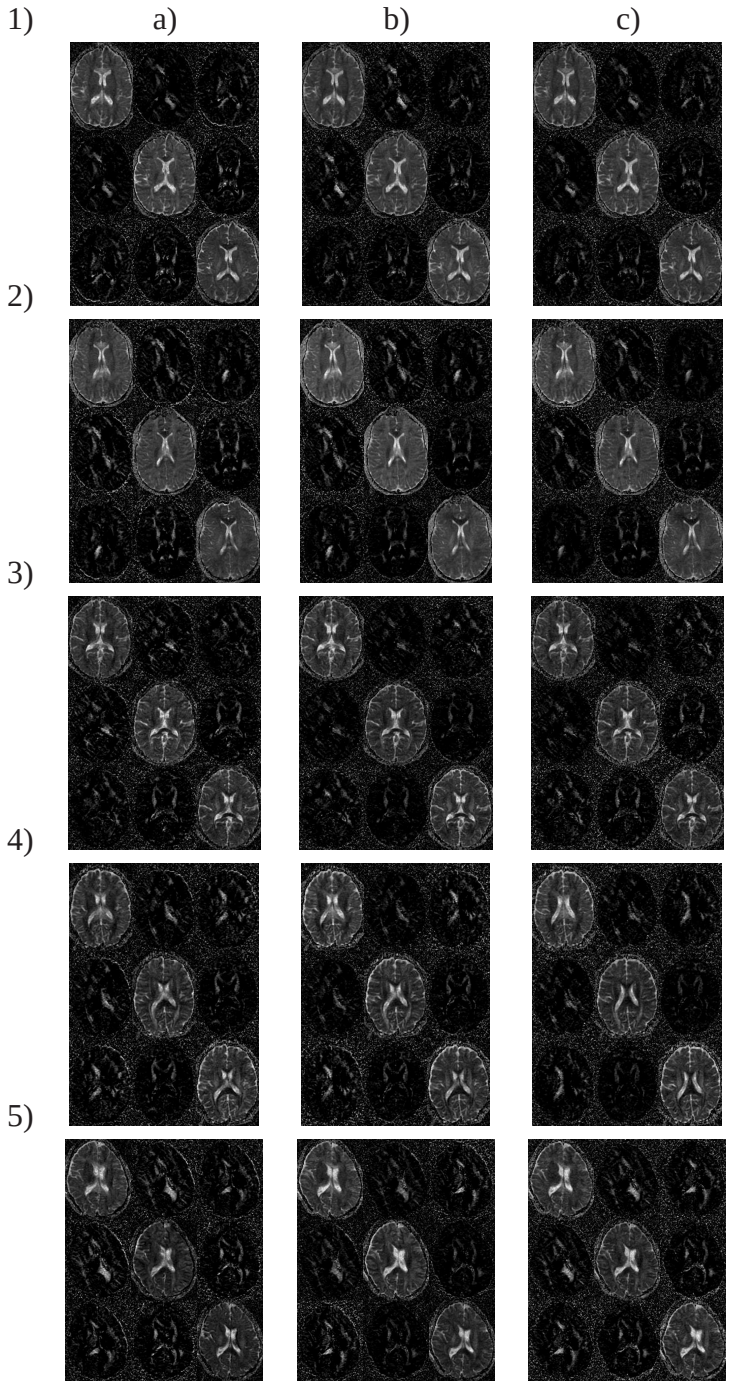

Figure 3.5: The calculated tensors, slice number 12 only is used from each of the nine volumes to save space. The three columns represents from left to right the three sequences used in the experiments a) 6 directions and 8 NEX, b) 13 directions and 4 NEX, c) 25 directions and 2 NEX and the five rows represents the five subjects 1) OB, 2) EK, 3) JL, 4) OH and 5) SA respectively. If you see closely it is possible to find that the tensors are symmetric matrixes, i.e. the elements above the diagonal elements are equal to the elements below the diagonal elements.

The tensor field is a 3-D volume with a 3×3 matrix associated to each voxel.

$$\mathbf{D} = \begin{bmatrix} D_{xx} & D_{xy} & D_{xz} \\ D_{yx} & D_{yy} & D_{yz} \\ D_{zx} & D_{zy} & D_{zz} \end{bmatrix} \tag{3.1}$$

It is therefore possible to make a new brain volume containing only one of the tensor elements in each voxel. This will give us nine new volumes, which is illustrated for subject OB, EK, JL, OH and SA in figure 3.5 page 35.

3.3 Fractional anisotropy maps

From the diffusion tensor **D**, we have calculated scalar maps of water diffusion anisotropy, where the fractional anisotropy index (FA) is the most frequently used. From such FA maps region and tissue specific values are often calculated and compared between clinical groups (having specific diagnosis) and control groups. We have therefore calculated and depicted FA maps for all our subjects using the different acquisition schemes.

FA is calculated from the eigenvalues as described in equation (1.25) in section 1.3.3. FA is then a image volume containing an FA value in each voxel.

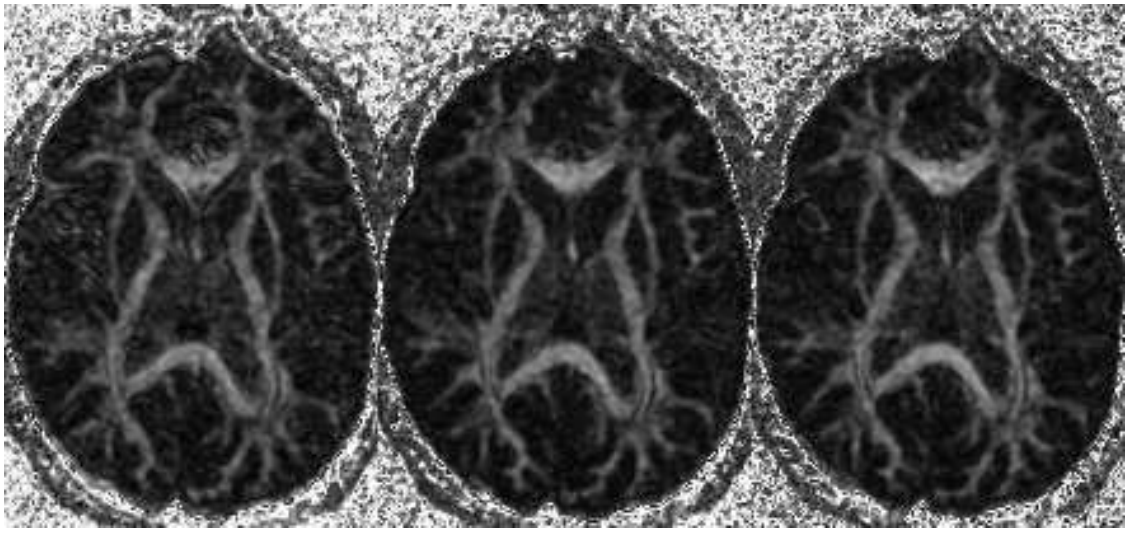

Figure 3.6: This figure shows the calculated FA maps for the three selected combinations of sequence parameters. From left to right, 6 directions and 8 NEX, 13 directions and 4NEX and 25 directions and 2 NEX. Data from subject OB.

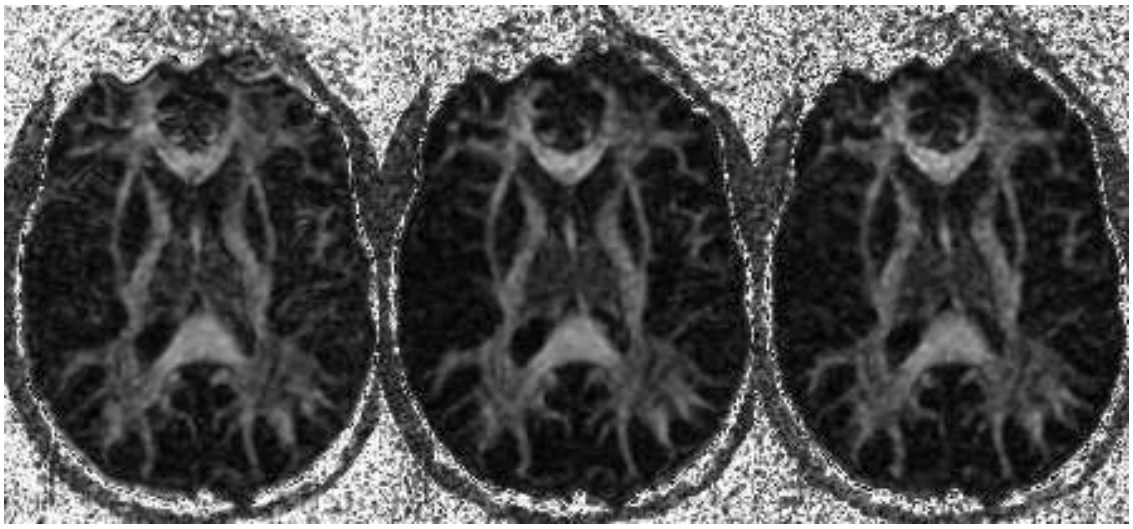

Figure 3.7: This figure shows the calculated FA maps for the three selected combinations of sequence parameters. From left to right, 6 directions and 8 NEX, 13 directions and 4NEX and 25 directions and 2 NEX. Data from subject EK.

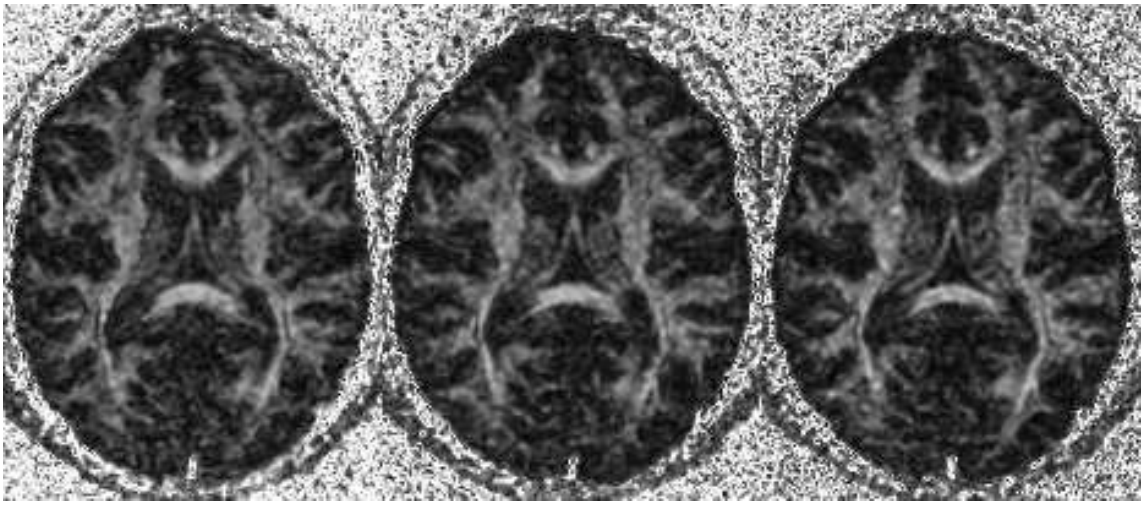

Figure 3.8: This figure shows the calculated FA maps for the three selected combinations of sequence parameters. From left to right, 6 directions and 8 NEX, 13 directions and 4NEX and 25 directions and 2 NEX. Data from subject JL.

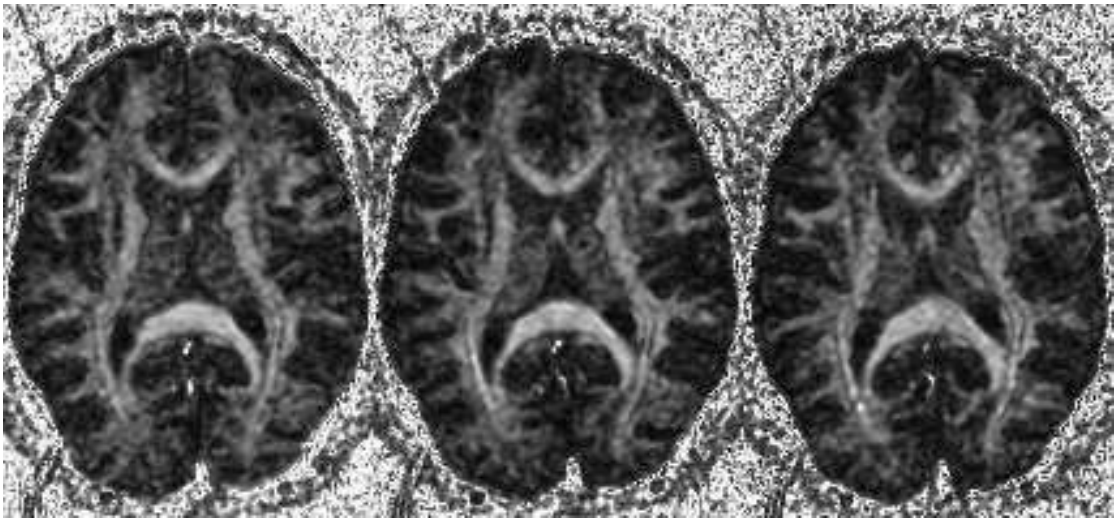

Figure 3.9: This figure shows the calculated FA maps for the three selected combinations of sequence parameters. From left to right, 6 directions and 8 NEX, 13 directions and 4NEX and 25 directions and 2 NEX. Data from subject OH.

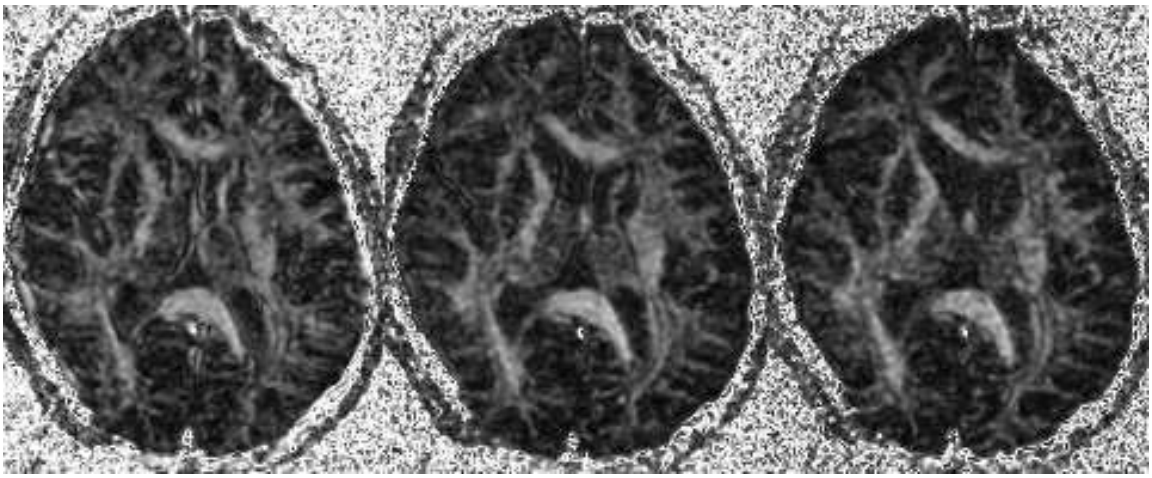

Figure 3.10: This figure shows the calculated FA maps for the three selected combinations of sequence parameters. From left to right, 6 directions and 8 NEX, 13 directions and 4NEX and 25 directions and 2 NEX. Data from subject SA.

3.4 The segmented volumes and the masks made from them

In order to obtain tissue specific statistics of FA values, we have performed probabilistic tissue segmentation using SPM2. The S_0-image, see figure 3.11 top left, which is the image without diffusion weighting (b=0), is segmented into the three parts – grey matter, white matter and cerebrospinal fluid – as described in section 2.3.4 page 25. The three parts are visualized in figure 3.11 left column. These images are probability masks. That means that in each voxel there is a certain probability that the voxel represents a certain tissue. Totally black is associated to a probability of 0 that the image voxel contains the specific tissue, totally white represents a probability of 1 (100%) that the image voxel contains the specific tissue. To place a certainty and limitation on the number of voxels in which FA is calculated, a threshold value is set to produce the final tissue specific masks. The threshold value in these experiments is set to 0.925. That means that there is 92.5 % probability that only the specific tissue is represented in the mask. Then it is possible to calculate tissue specific FA values. The final mask images are shown below in figure 3.11 right column.

	gVx	wVx	cVx
EK	37877	32022	25607
OB	61886	42720	49298
JL	56466	39588	48372
OH	41600	33623	40683
SA	42594	24987	35175

Table 3.1: The table shows the number of voxels in each mask using the threshold value 0.925. gVx is gray matter mask, wVx is white matter mask and cVx is the mask obtained from cerebrospinal fluid. It is important to note that the masks spans the whole brain volume.

To better illustrate the "the quality" of the tissue specific masks we have made depictions where the masks is superimposed on the S_0-image. Such composite images are shown in figures 3.17, 3.18, 3.16, 3.19 and 3.20 for subject OB, EK, JL, OH and SA respectively. Table 3.1 page 39 gives the number of tissue specific voxels used for obtaining the FA statistics for each subject.

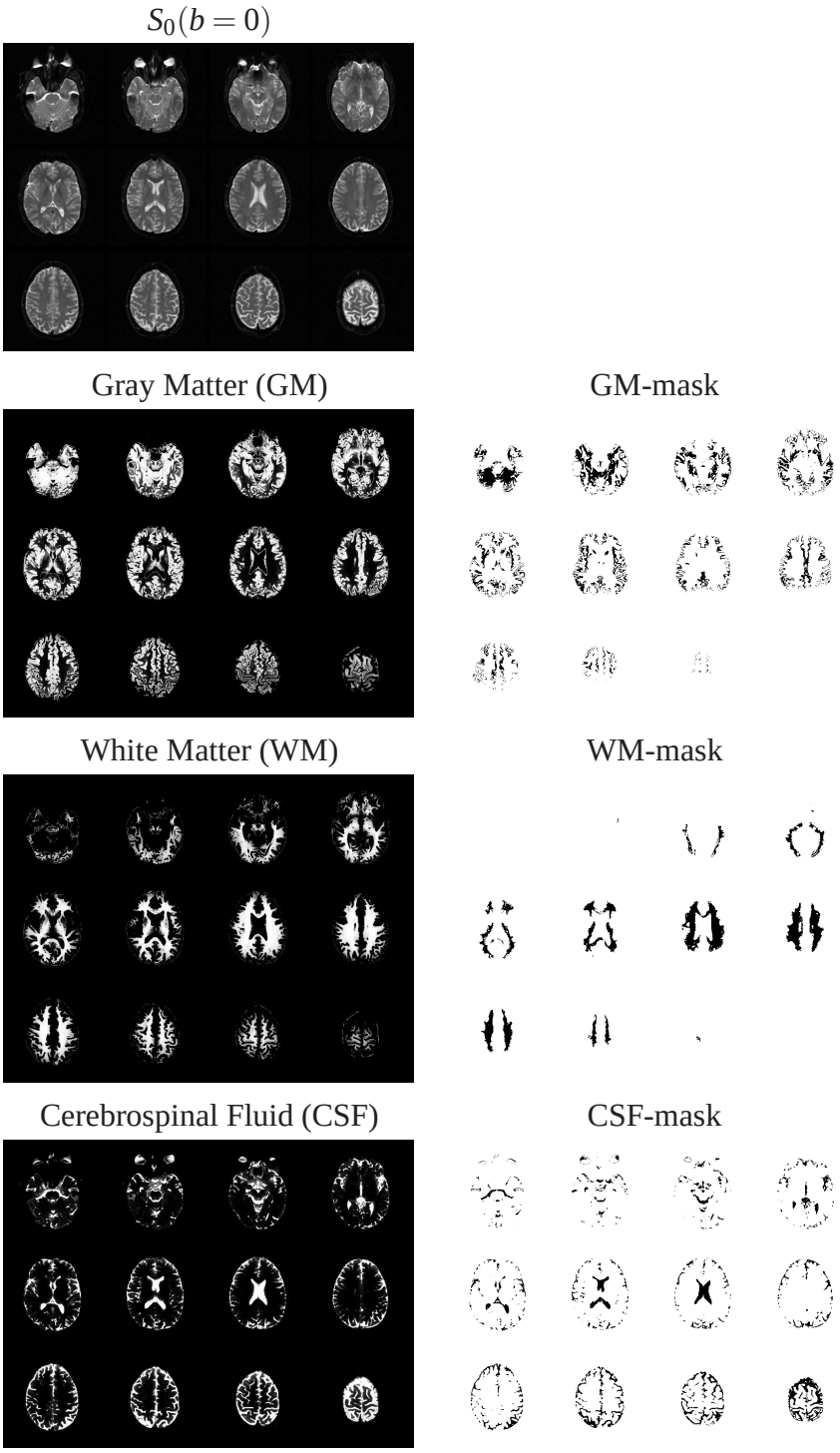

Figure 3.11: The segmented volumes and the masks. Data from subject OB.

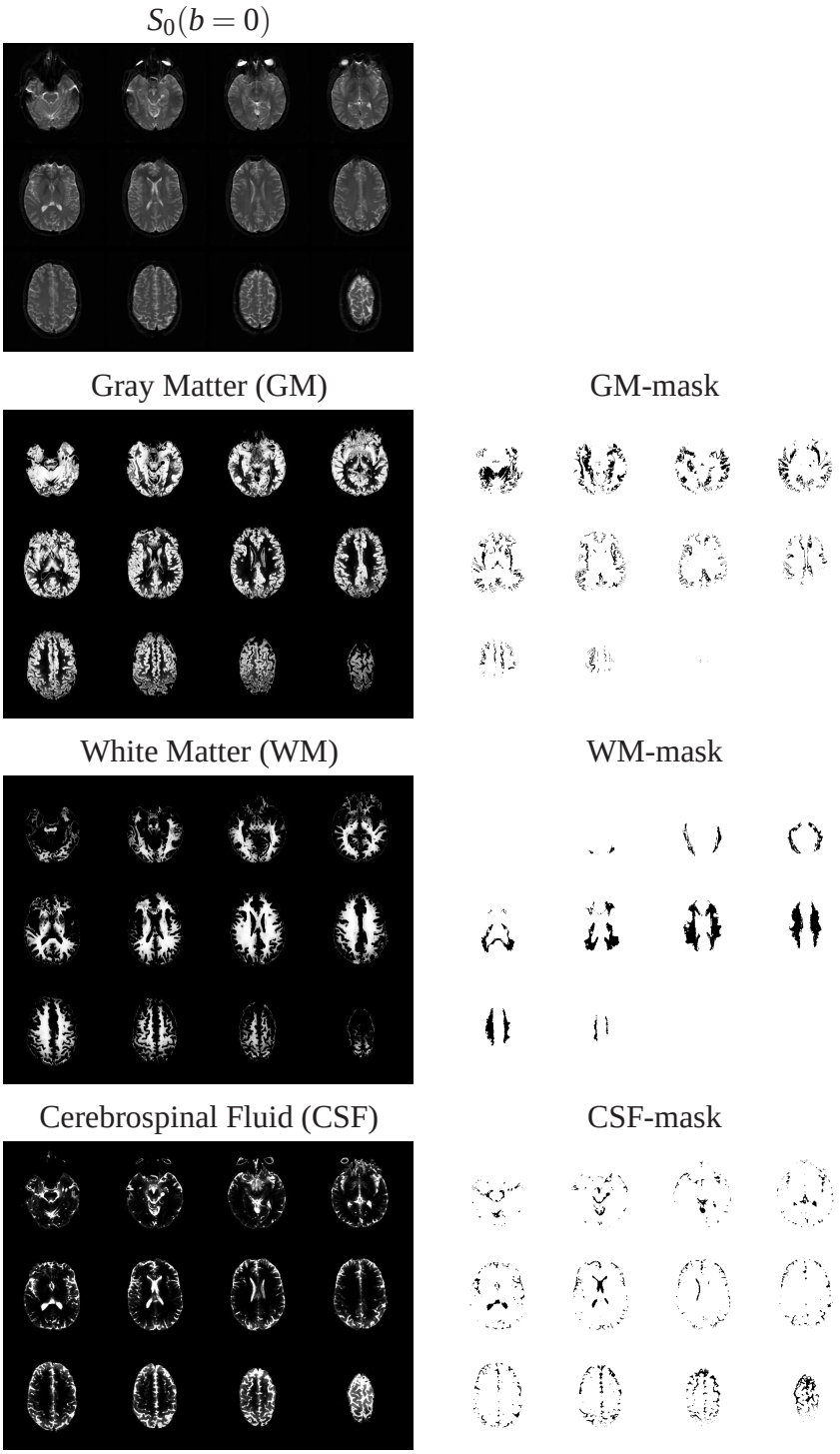

Figure 3.12: The segmented volumes and the masks. Data from subject EK.

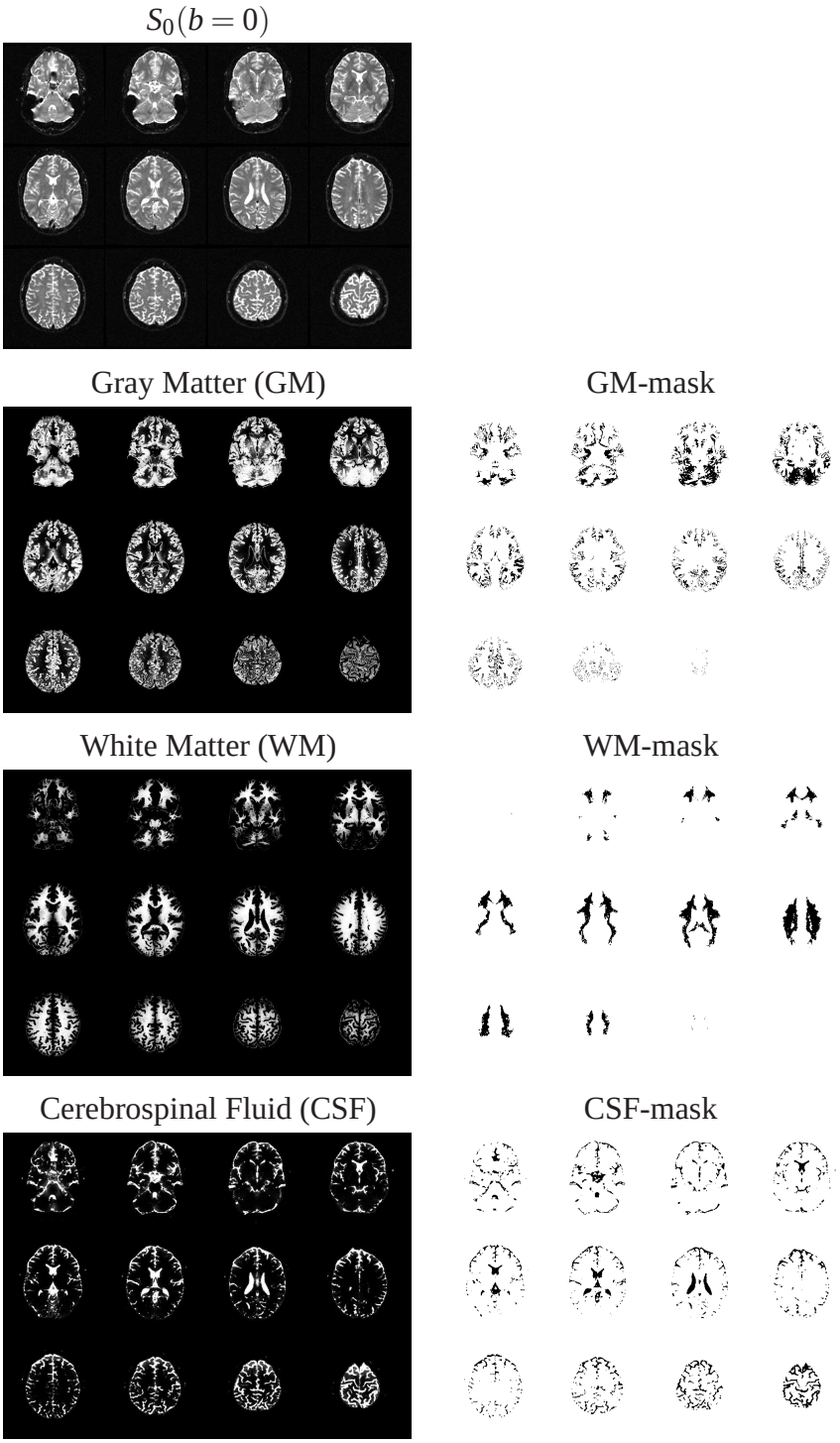

Figure 3.13: The segmented volumes and the masks. Data from subject JL.

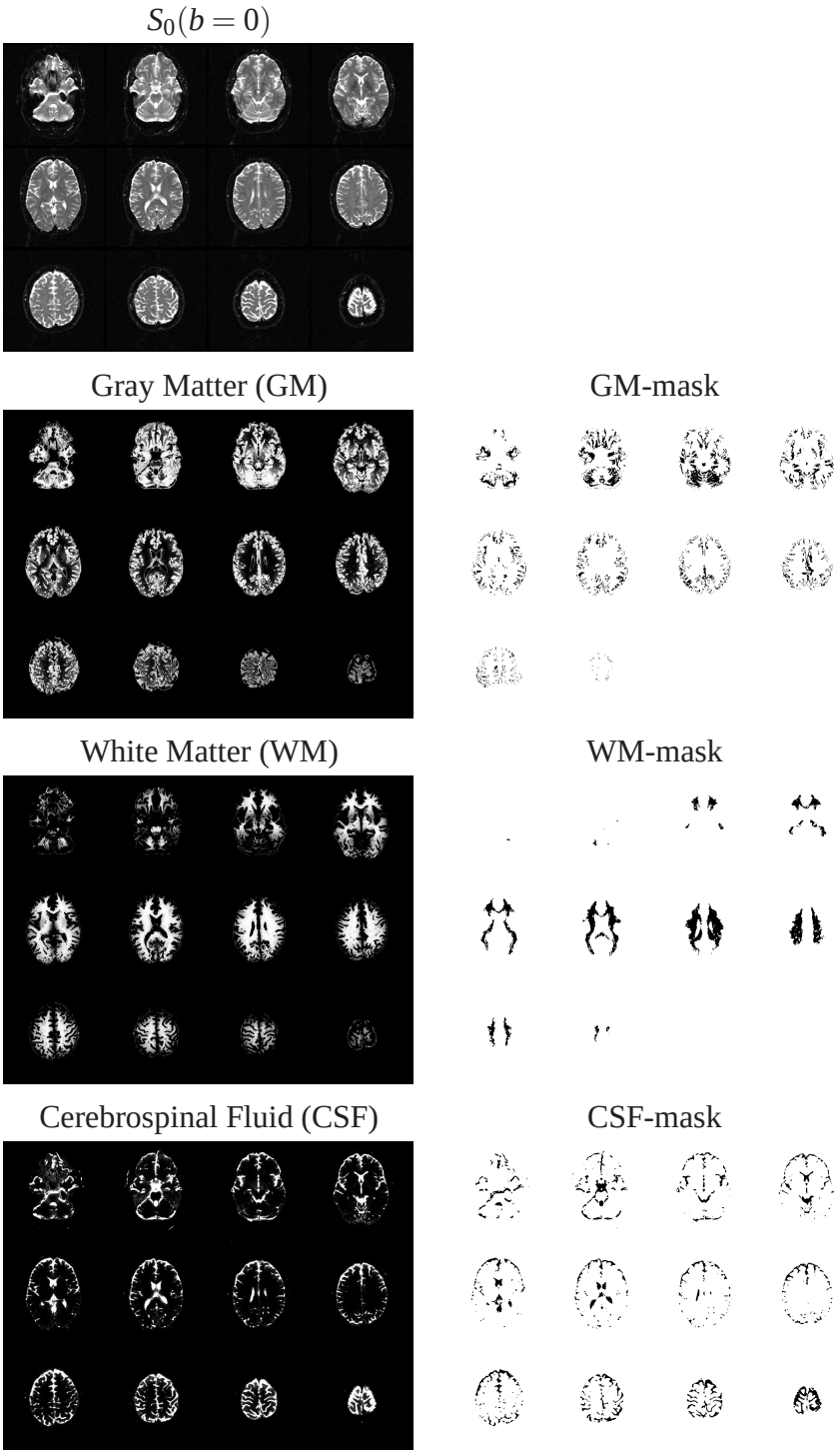

Figure 3.14: The segmented volumes and the masks. Data from subject OH.

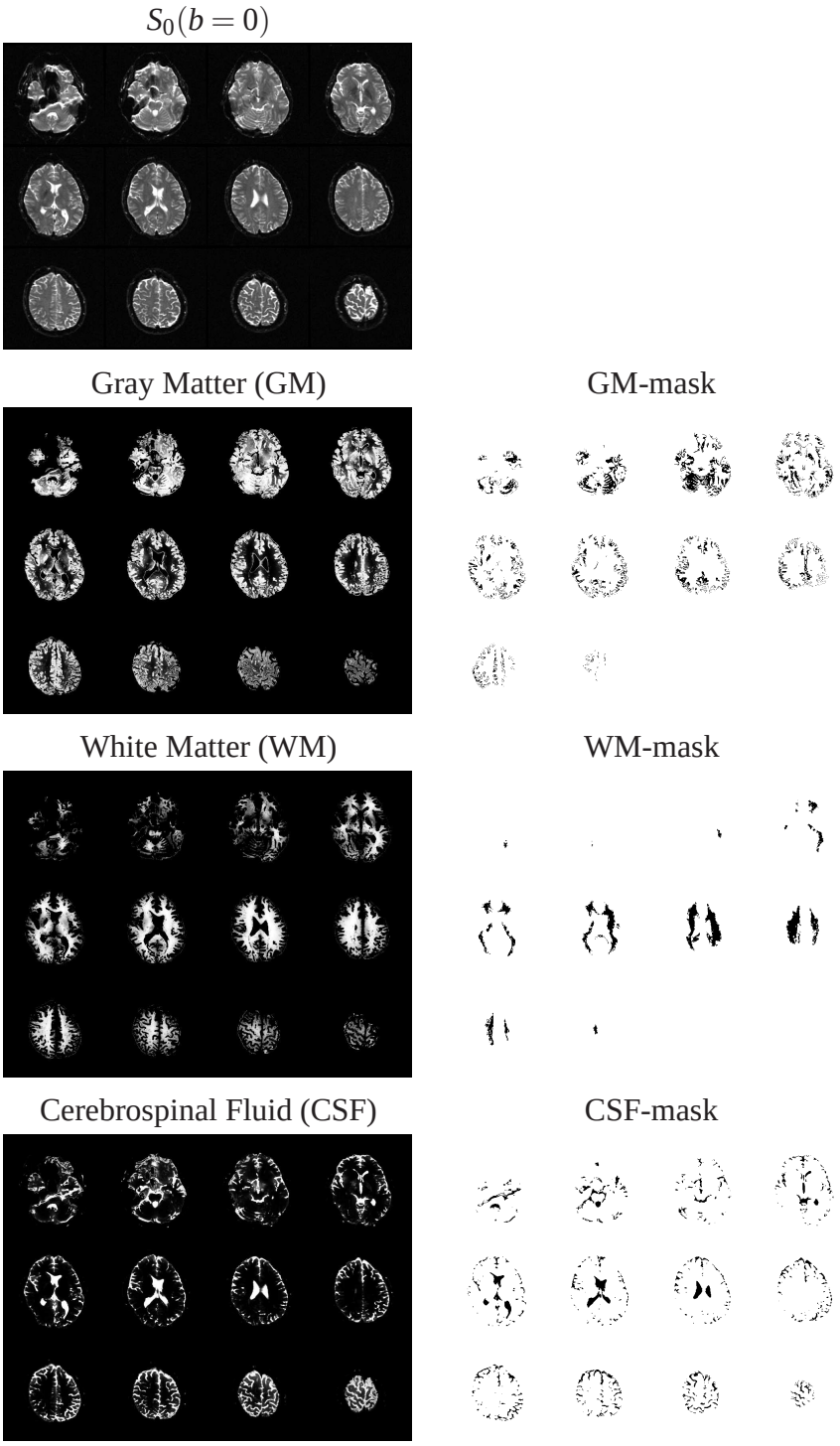

Figure 3.15: The segmented volumes and the masks. Data from subject SA.

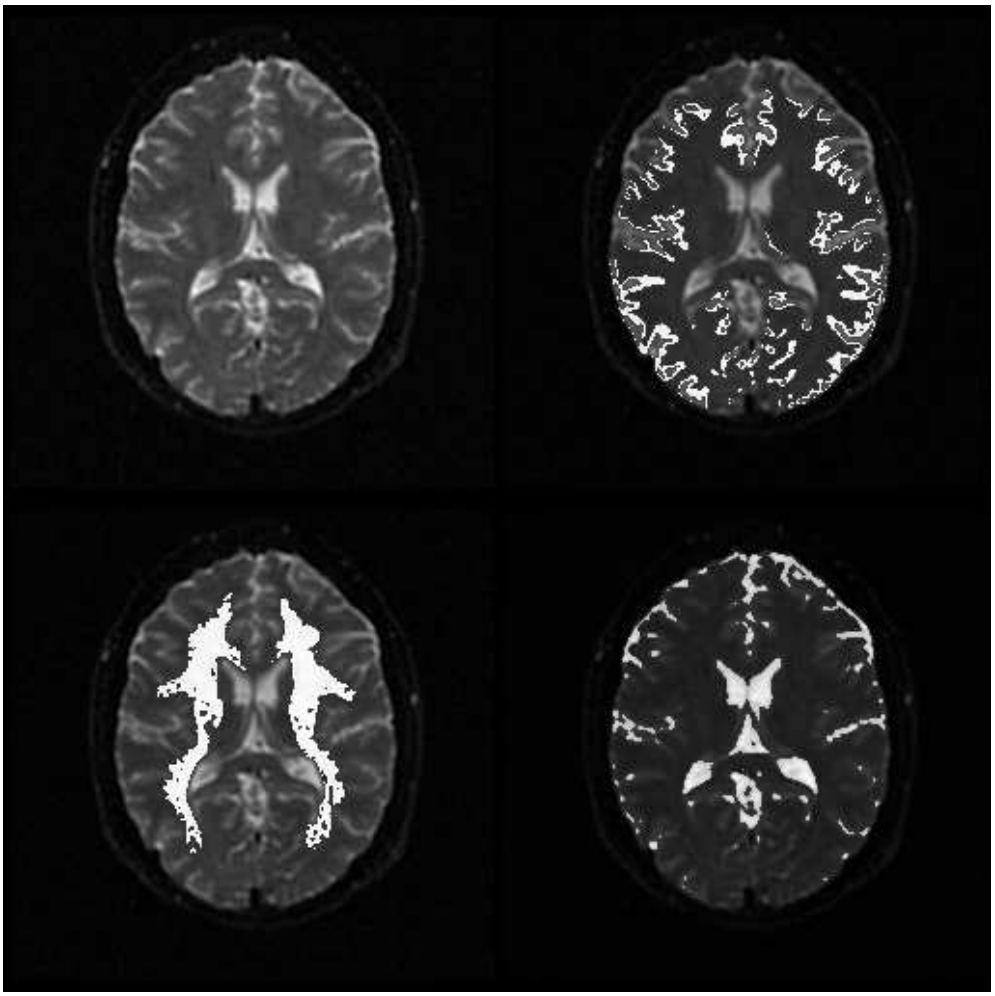

Figure 3.16: This figure demonstrates the location of the tissue specific masks on a non diffusion weighted image (the b0 image). The top left image is a plain b0 image, the top right shows the gray matter voxels, the bottom left the white matter voxels and the bottom right the cerebrospinal fluid voxels. Only slice number 12 is shown to save space. The subject that is used to exemplify these results is JL.

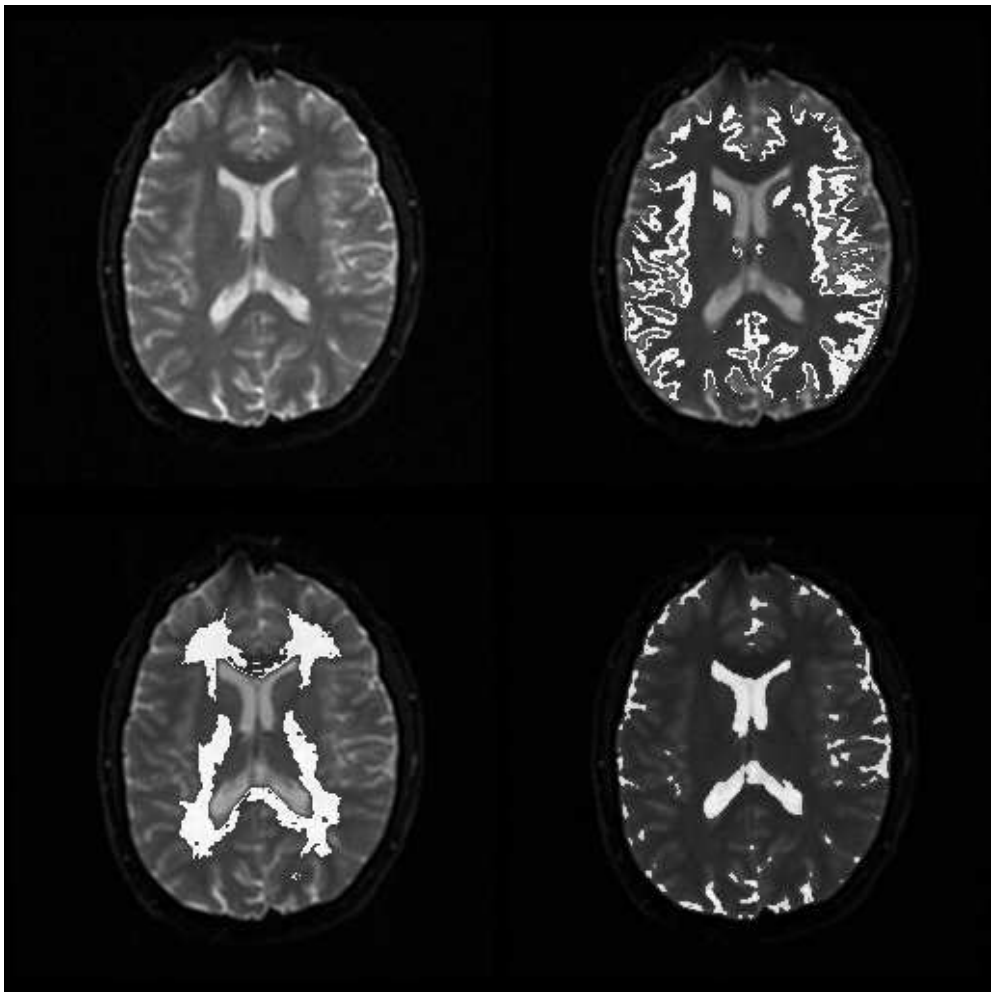

Figure 3.17: This figure demonstrates the location of the tissue specific masks on a non diffusion weighted image (the b0 image). The top left image is a plain b0 image, the top right shows the gray matter voxels, the bottom left the white matter voxels and the bottom right the cerebrospinal fluid voxels. Only slice number 12 is shown to save space. The subject that is used to exemplify these results is OB.

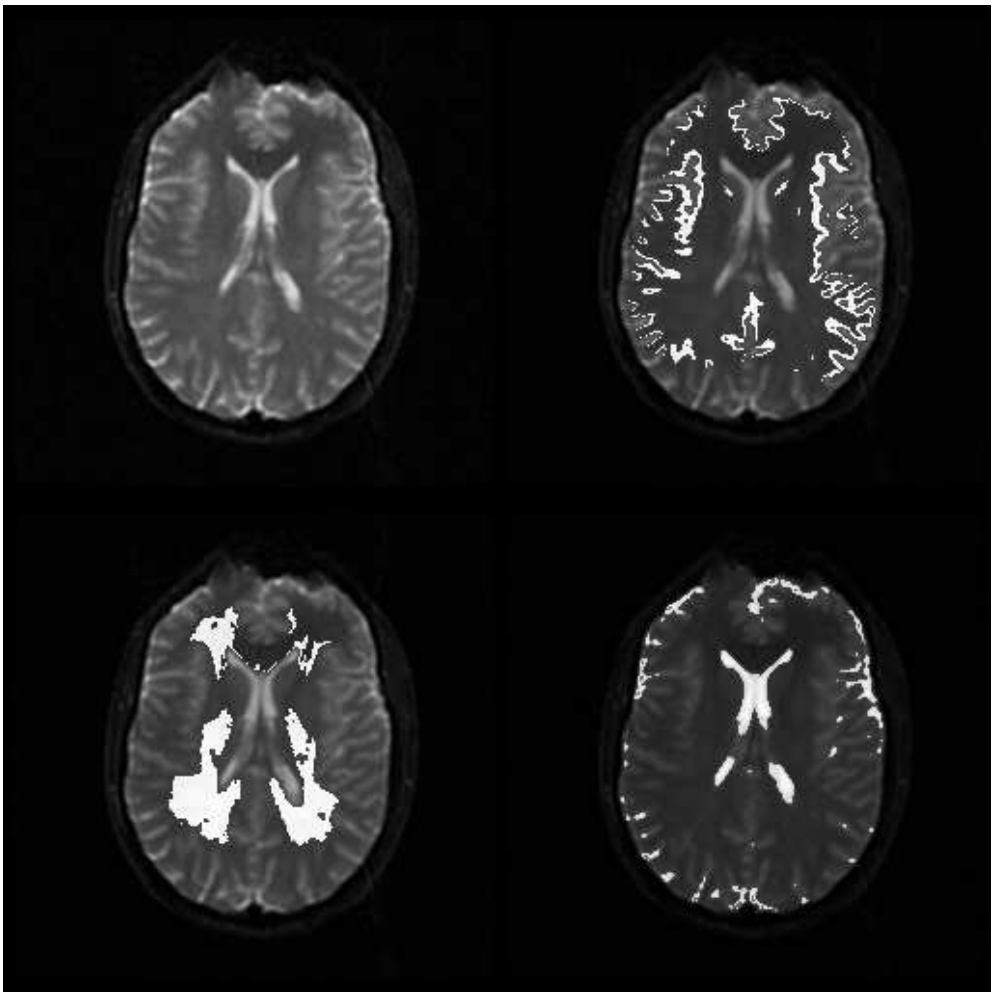

Figure 3.18: This figure demonstrates the location of the tissue specific masks on a non diffusion weighted image (the b0 image). The top left image is a plain b0 image, the top right shows the gray matter voxels, the bottom left the white matter voxels and the bottom right the cerebrospinal fluid voxels. Only slice number 12 is shown to save space. The subject that is used to exemplify these results is EK.

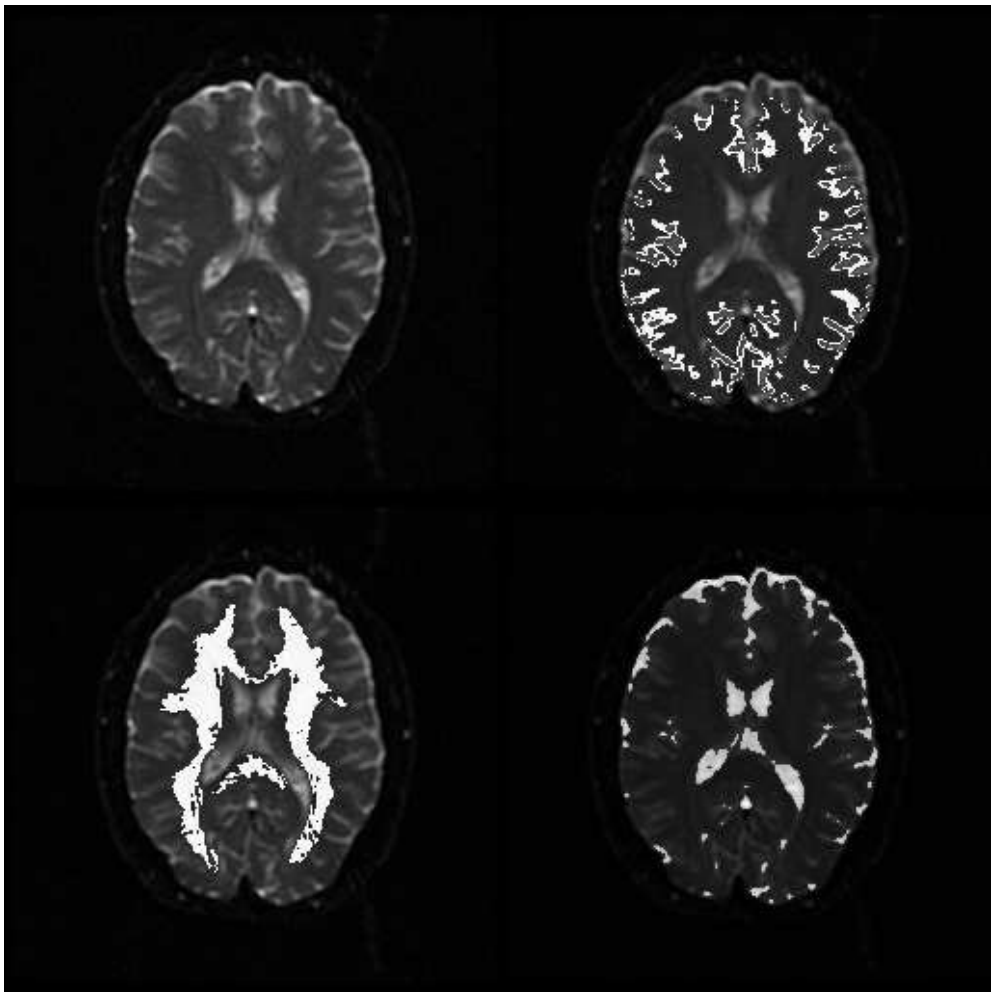

Figure 3.19: This figure demonstrates the location of the tissue specific masks on a non diffusion weighted image (the b0 image). The top left image is a plain b0 image, the top right shows the gray matter voxels, the bottom left the white matter voxels and the bottom right the cerebrospinal fluid voxels. Only slice number 12 is shown to save space. The subject that is used to exemplify these results is OH.

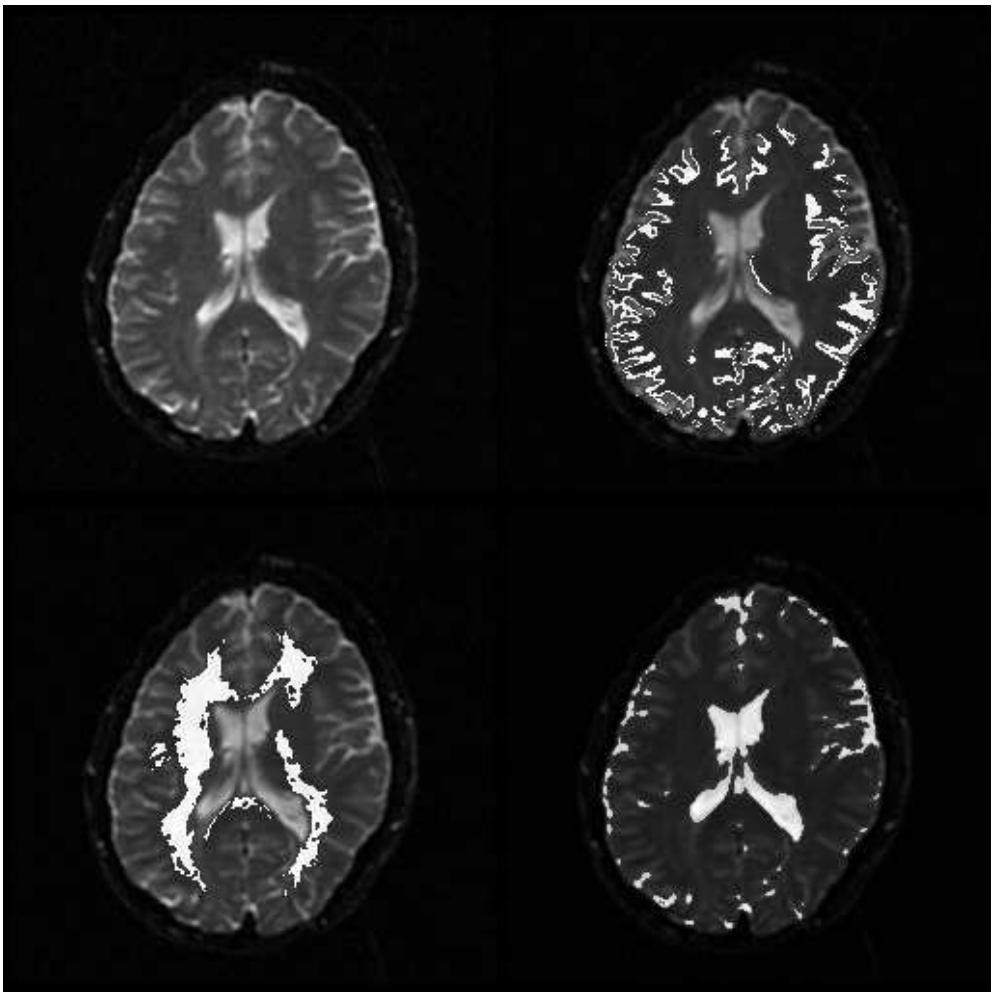

Figure 3.20: This figure demonstrates the location of the tissue specific masks on a non diffusion weighted image (the b0 image). The top left image is a plain b0 image, the top right shows the gray matter voxels, the bottom left the white matter voxels and the bottom right the cerebrospinal fluid voxels. Only slice number 12 is shown to save space. The subject that is used to exemplify these results is SA.

3.5 FA distributions

A direct sample distribution of tissue specific FA-values are given below for the different DTI acquisition schemes. The distributions show how many voxels that holds the respective FA values in the specified masks. As expected from known tissue architecture of gray matter and white matter the FA values is generally lower for grey matter than for white matter. Cerebrospinal fluid is even more isotropic than grey matter and have even lower FA values as shown in the figures 3.21, 3.22 and 3.23. The distributions is nearly Gaussian, especially for white matter. Distribution plots will only be presented for one subject to save space.

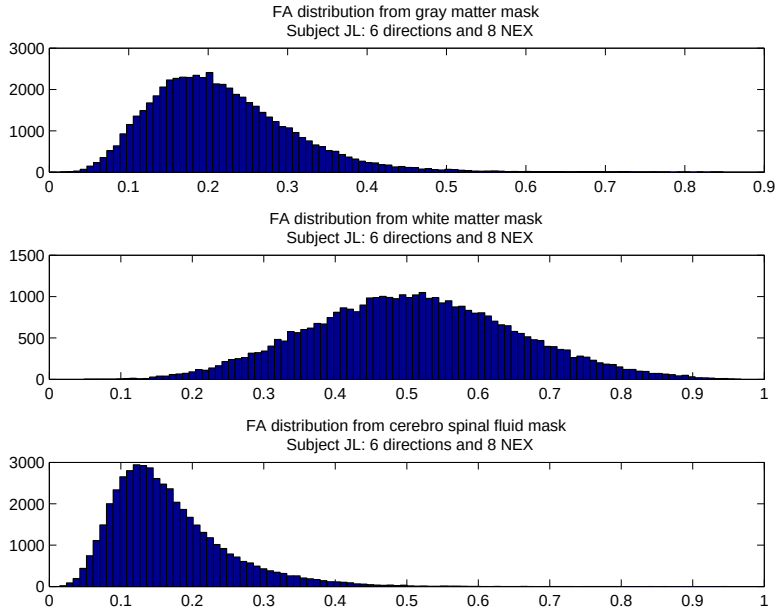

Figure 3.21: FA distribution for the three tissue specific masks for subject JL, the sequence is 6 diffusion sensitizing directions and 8 NEX. The mean values for FA from top to bottom is: 0.217, 0.510 and 0.167.

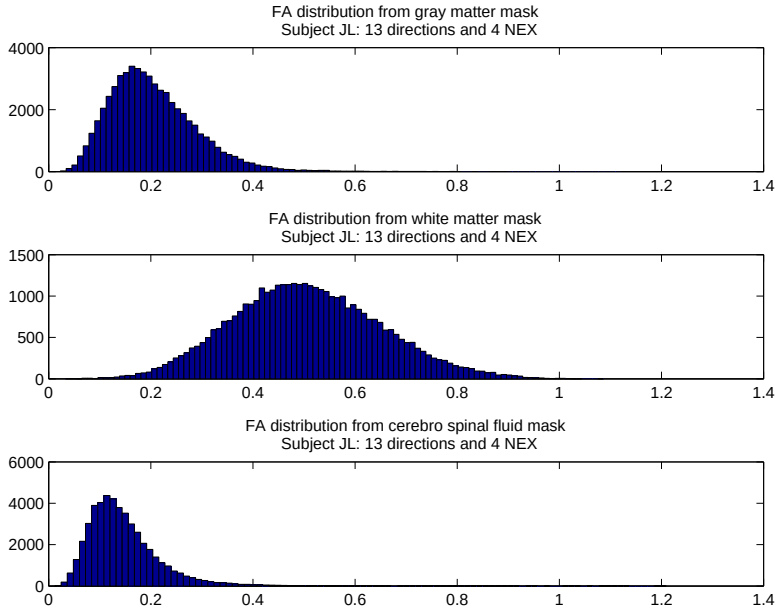

Figure 3.22: FA distribution for the three tissue specific masks for subject JL, the sequence is 13 diffusion sensitizing directions and 4 NEX. The mean values for FA from top to bottom is: 0.205, 0.506 and 0.147.

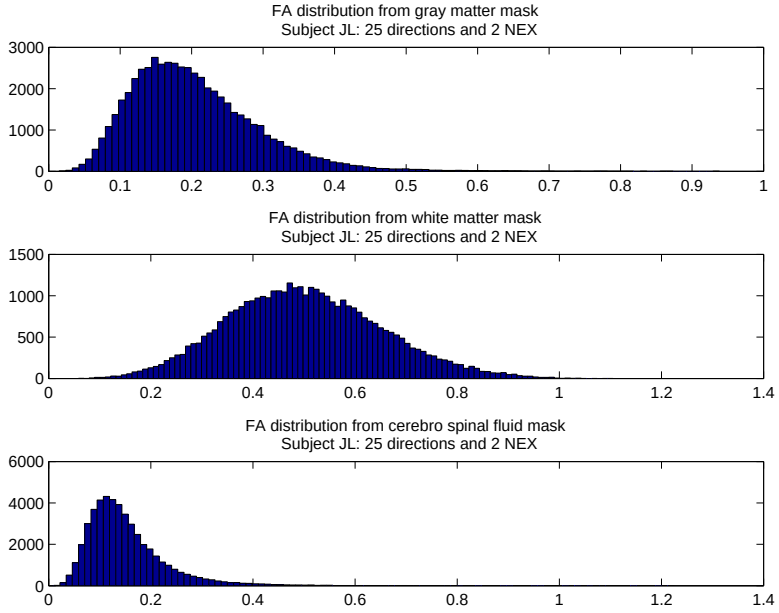

Figure 3.23: FA distribution for the three tissue specific masks for subject JL, the sequence is 25 diffusion sensitizing directions and 2 NEX. The mean values for FA from top to bottom is: 0.204, 0.502 and 0.152.

3.6 The standard deviation, mean and coefficient of variation of the FA

To further analyze the effect of DTI acquisition schemes on the tissue specific FA, we have calculated standard deviation, mean and coefficient of variation (CV). Normally the standard deviation of the FA values would have told us a lot about the differences in SNR for the three sequences. Since the mean values shows such variation we use the CV instead.

	6dir	8NEX		13dir	4NEX		25dir	2NEX	
#	std	mean	**cv**	std	mean	cv	std	mean	cv
OB_{gm}	0.076	0.151	0.504	0.073	0.136	0.535	0.069	0.133	0.518
OB_{wm}	0.111	0.347	**0.319**	0.111	0.333	0.333	0.110	0.337	0.328
OB_{csf}	0.086	0.150	0.576	0.061	0.115	0.530	0.062	0.116	**0.530**
EK_{gm}	0.073	0.146	0.497	0.063	0.123	0.508	0.063	0.129	0.493
EK_{wm}	0.114	0.361	**0.316**	0.115	0.354	0.325	0.117	0.361	0.323
EK_{csf}	0.094	0.145	0.648	0.060	0.106	0.569	0.060	0.106	**0.559**
JL_{gm}	0.090	0.217	0.416	0.086	0.205	0.422	0.089	0.204	0.439
JL_{wm}	0.142	0.510	**0.279**	0.144	0.506	0.285	0.150	0.502	0.299
JL_{csf}	0.081	0.167	**0.481**	0.075	0.147	0.510	0.081	0.152	0.533
OH_{gm}	0.098	0.210	0.466	0.098	0.200	0.491	0.120	0.216	0.555
OH_{wm}	0.147	0.489	**0.301**	0.147	0.472	0.311	0.152	0.447	0.341
OH_{csf}	0.083	0.174	**0.476**	0.100	0.164	0.609	0.178	0.208	0.856
SA_{gm}	0.127	0.258	0.493	0.126	0.246	0.513	0.134	0.240	0.559
SA_{wm}	0.132	0.434	**0.305**	0.142	0.398	0.357	0.148	0.380	0.390
SA_{csf}	0.119	0.240	**0.496**	0.131	0.222	0.591	0.152	0.223	0.681

Table 3.2: This table shows the standard deviation, the mean and the coefficient of variation for the fractional anisotropy values taken from the three masks for the three DTI acquisition schemes for all five subjects.

Notice that for all subjects the lowest CV is obtained in white matter using 6 diffusion directions and 8 NEX. However, the CV values for 13 directions and 4 NEX and 25 directions and 2 NEX are very close. Moreover, the CV of CSF is partly lower for 25 directions and 2 NEX compared to 6 directions and 8 NEX for subject OB and EK, and partly higher for subject JL, OH and SA. Since we expect FA to be high and rather homogeneous throughout CSF, it is hard to conclude from these data, which DTI acquisition scheme is generally best.

3.7 Plotting graphics

The next step in our analysis has been to explore directional dependence in our tissue specific FA calculations. With good quality data we should expect the standard deviation of FA, std(FA), to be dependent on the degree of anisotropy in tissue only and independent of the principal diffusion direction. By plotting the standard deviation of FA as a function of the azimuth θ and elevation ϕ of the principal eigenvector, we obtain a kind of directional dependent SNR for our three DTI acquisition schemes. Great variation, a rough plot, implies low SNR. Little variation, a smooth or flat plot, implies high SNR and better quality. Below plots, describing the directional dependencies of the standard deviation of the FA values are drawn.

In each voxel in the image volume the FA and directional information from the principal eigenvector is calculated. Voxels containing principal eigenvectors with directions in certain intervals are grouped together. The standard deviation of the FA values from the voxels in such groups are plotted against the azimuth θ and elevation ϕ values, which are the direction of the principal eigenvector in spherical coordinates.

Plots for every subject is made, but only one subject will be presented in this thesis to save space.

In gray matter, the three dimensional plots is smoother for 13 diffusion sensitizing directions with 4 NEX and 25 directions with 2 NEX than for 6 diffusion sensitizing directions with 8 NEX.

In white matter there is higher variation than in gray matter and cerebrospinal fluid. This is expected because white matter has higher directionality than the other tissue substances. The plot for 13 directions with 4 NEX shows a little smoother plot than for 6 directions with 8 NEX. The plot for 25 directions and 2 NEX is even smoother than the plot above. But the downhill for negative θ values is hard to explain.

In cerebrospinal fluid, the plot for 13 directions with 4 NEX is smoother than the other two plots.

But any of the difference is not large enough to have potential to make any conclusions in favor to one of the acquisition schemes.

3.7.1 Plots for gray matter

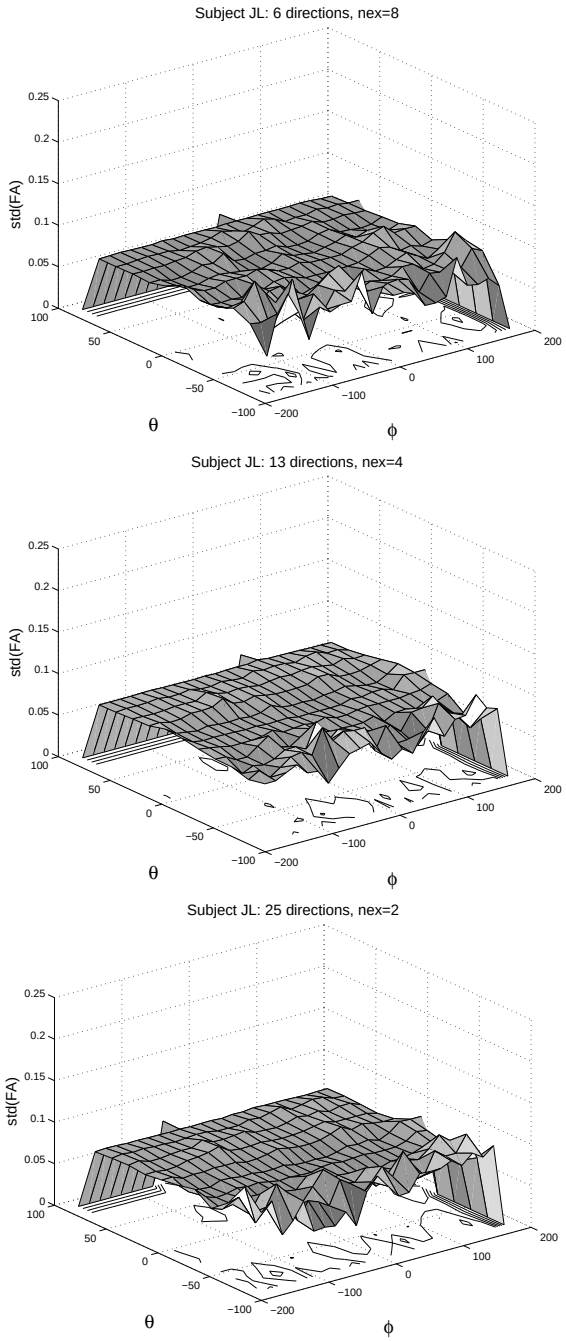

Figure 3.24: This 3D plot shows the standard deviation for the FA values as a function of the azimuth θ and elevation ϕ for the largest eigenvector. Data from subject JL. The plot at the top of the figure shows the results for the scanner image parameter sequence 6 directions and 8 NEX, the middle plot 13 directions and 4 NEX, the bottom plot 25 directions and 2 NEX. The voxels which is chosen to evaluate the FA are taken from the gray matter mask.

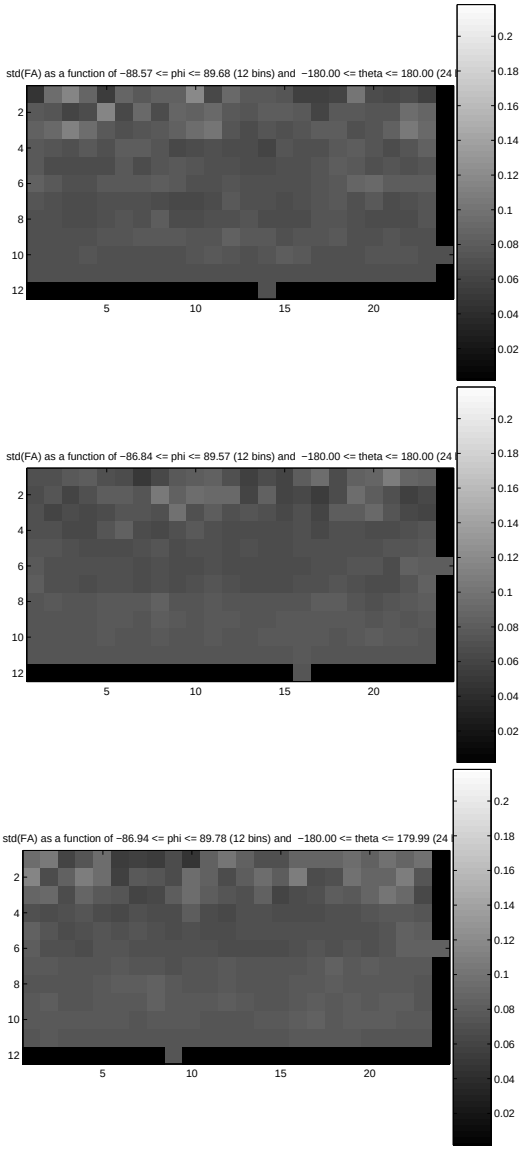

Figure 3.25: This plot demonstrates the same as the 3D plot above in a 2D plot. The gray scale intensity differences indicate the variation in the standard deviation of FA as a function of θ and ϕ. Data from subject JL and the three DTI sequences is displayed in rapid succession from top to bottom. The mask used is gray matter mask.

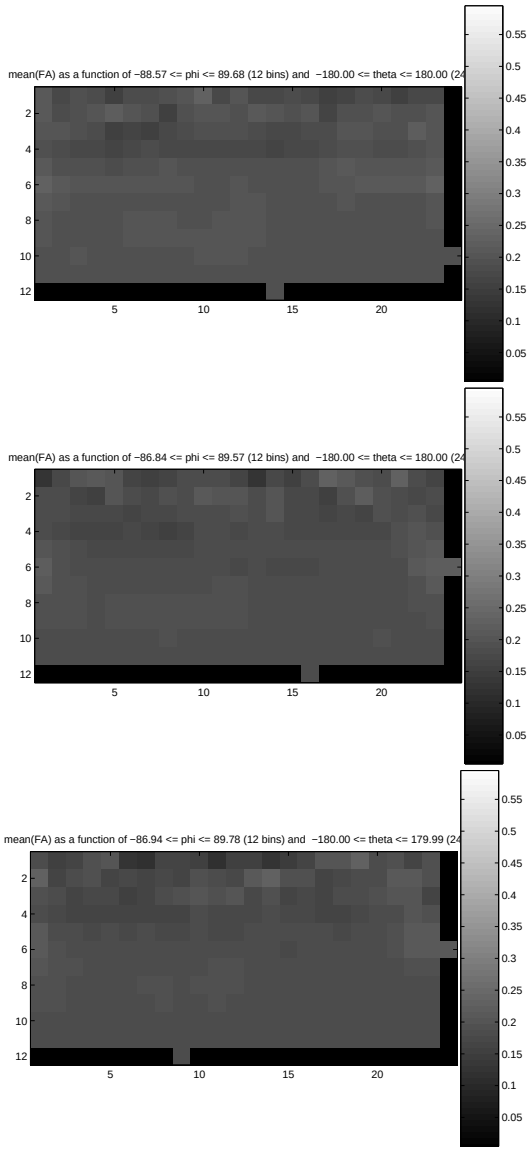

Figure 3.26: This plot demonstrates the mean values of FA in the same manner as the standard deviation plot above.

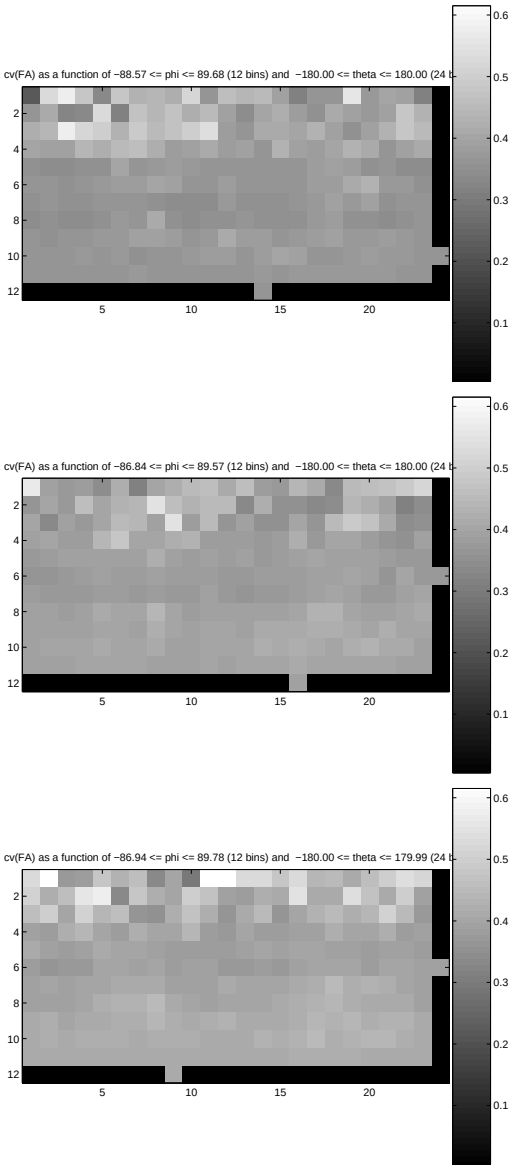

Figure 3.27: This plot demonstrates the coefficient of variation, CV, of the FA values in the same manner as the standard deviation plot above. $cv(FA) = std(FA)/mean(FA)$. That is the standard deviation relative to the mean value. The CV is useful when there are variations in the mean values.

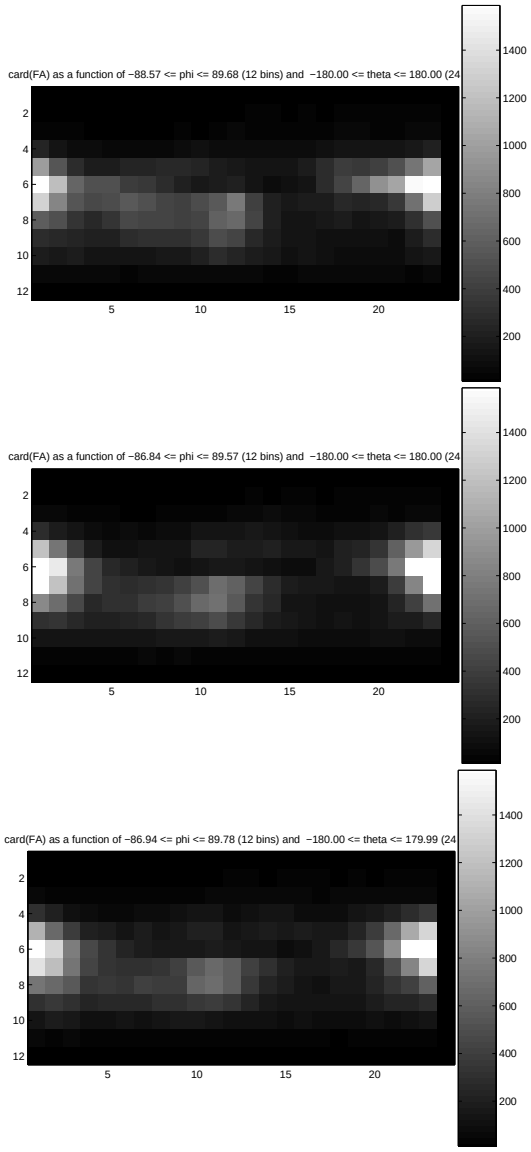

Figure 3.28: This gray scale plot demonstrates how many voxels that have the same values for the θ and ϕ angles.

3.7.2 Plots for white matter

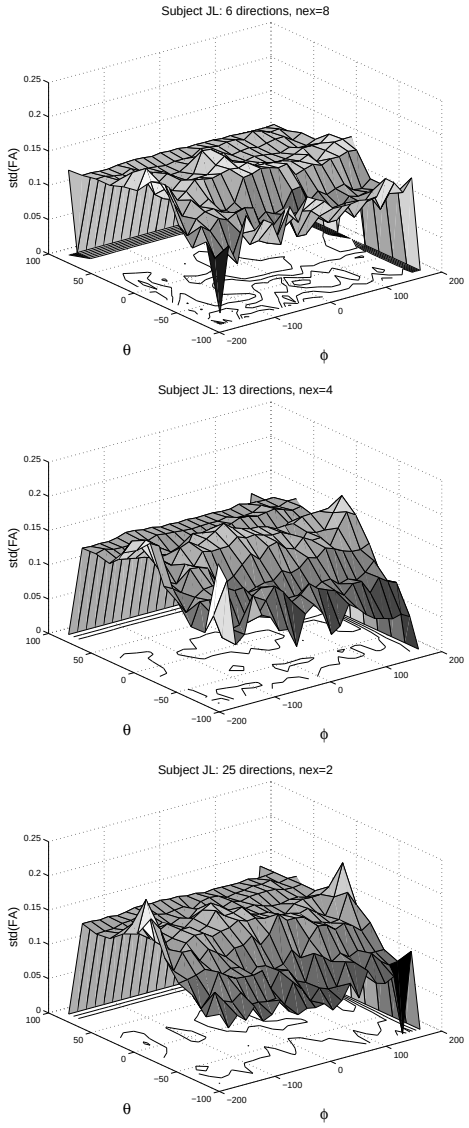

Figure 3.29: This 3D plot shows the standard deviation for the FA values as a function of the azimuth θ and elevation ϕ for the largest eigenvector. Data from subject JL. The plot at the top of the figure shows the results for the scanner image parameter sequence 6 directions and 8 NEX, the middle plot 13 directions and 4 NEX, the bottom plot 25 directions and 2 NEX. The voxels which is chosen to evaluate the FA are taken from the white matter mask.

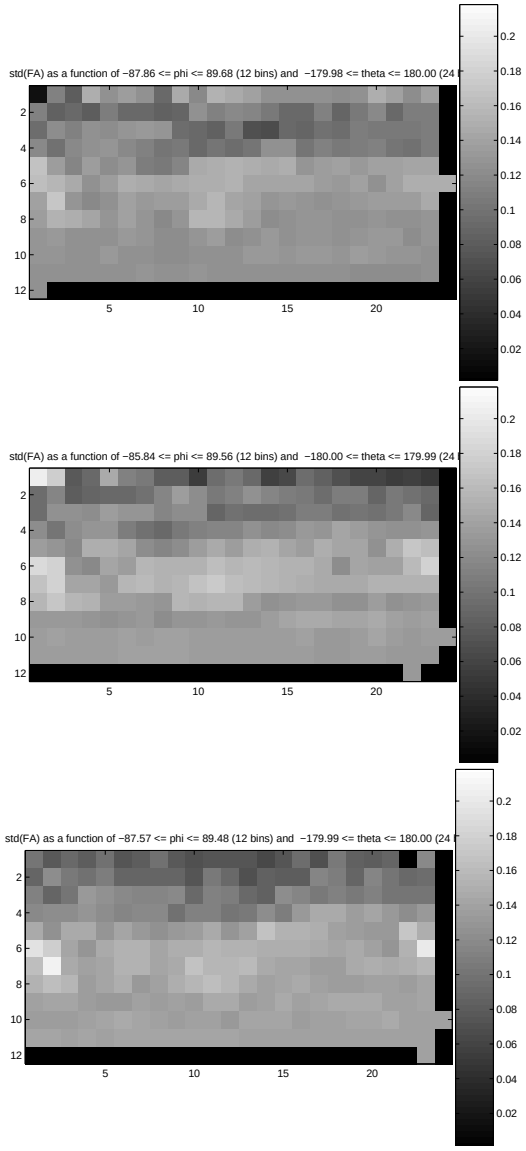

Figure 3.30: This plot demonstrates the same as the 3D plot above in a 2D plot. The gray scale intesity differences indicate the variation in the standard deviation of FA as a function of θ and ϕ. Data from subject JL and the three DTI sequences is displayed in rapid succession from top to bottom. The mask used is white matter mask.

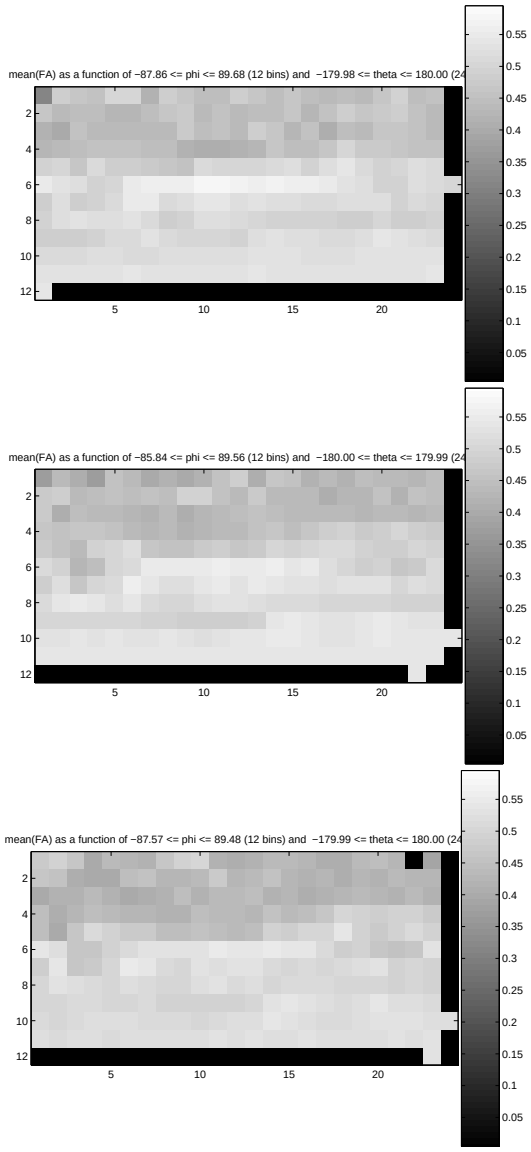

Figure 3.31: This plot demonstrates the mean values of FA in the same manner as the standard deviation plot above.

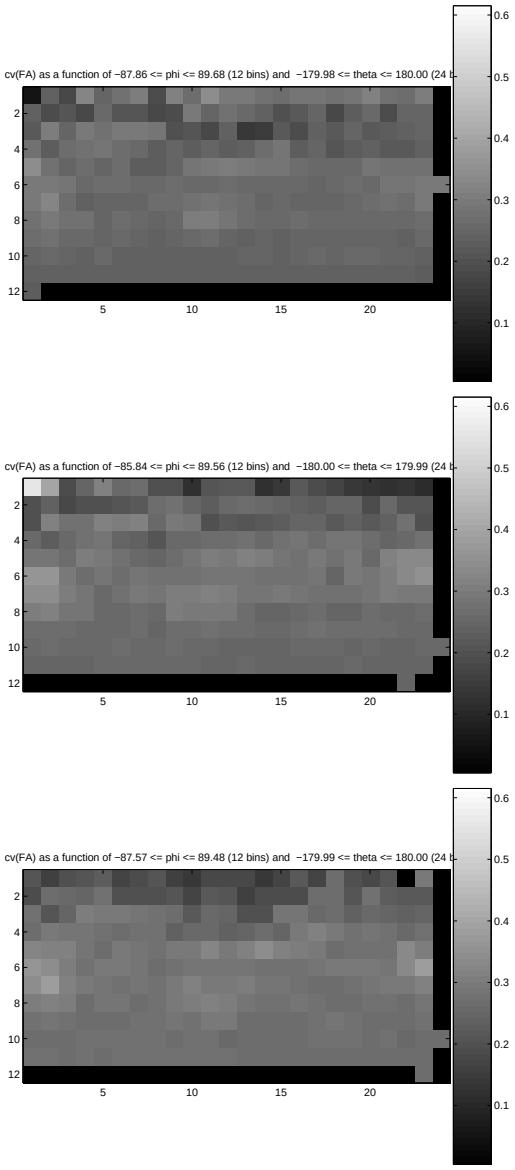

Figure 3.32: This plot demonstrates the coefficient of variation, CV, of the FA values in the same manner as the standard deviation plot above. $cv(FA) = std(FA)/mean(FA)$. That is the standard deviation relative to the mean value. The CV is useful when there are variations in the mean values.

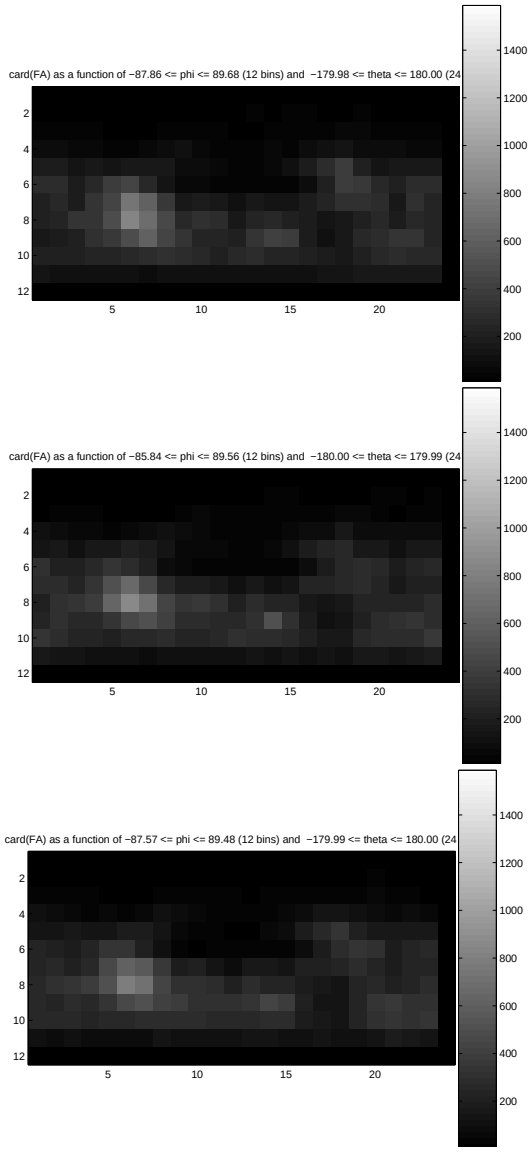

Figure 3.33: This gray scale plot demonstrates how many voxels that have the same properties for the θ and ϕ angles.

3.7.3 Plots for cerebrospinal fluid

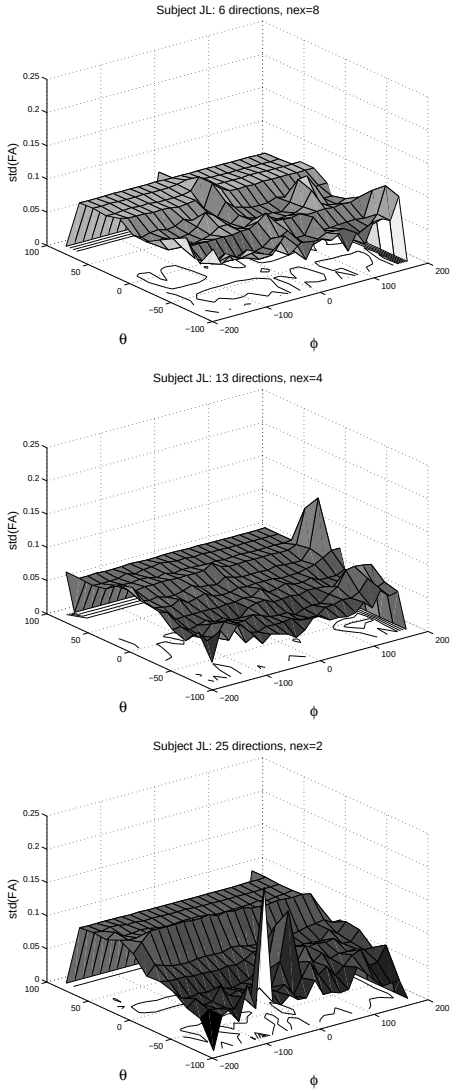

Figure 3.34: This 3D plot shows the standard deviation for the FA values as a function of the azimuth θ and elevation ϕ for the largest eigenvector. Data from subject JL. The plot at the top of the figure shows the results for the scanner image parameter sequence 6 directions and 8 NEX, the middle plot 13 directions and 4 NEX, the bottom plot 25 directions and 2 NEX. The voxels which is chosen to evaluate the FA are taken from the cerebrospinal fluid mask.

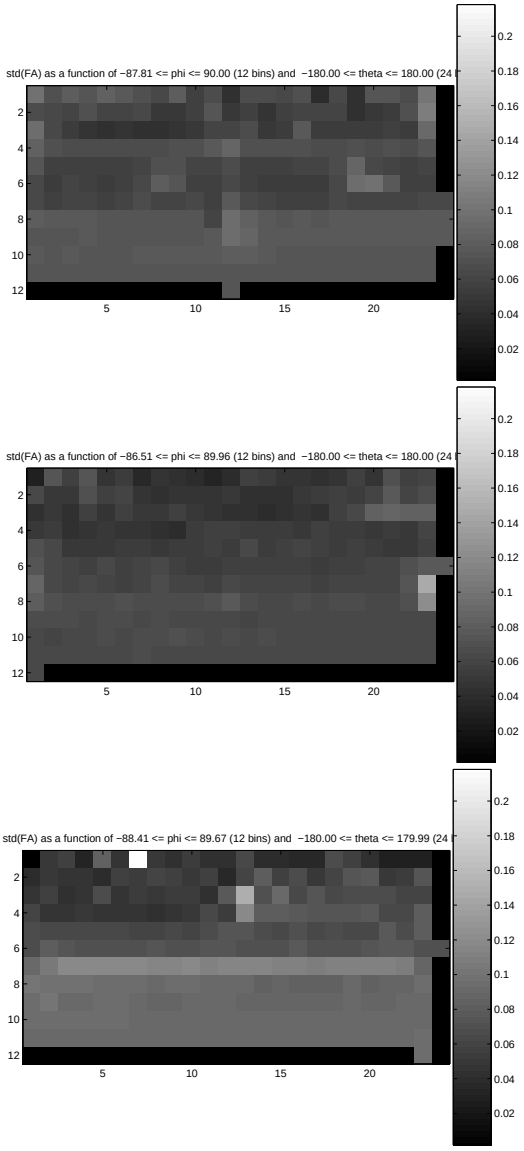

Figure 3.35: This plot demonstrates the same as the 3D plot above in a 2D plot. The gray scale intesity differences indicate the variation in the standard deviation of FA as a function of θ and ϕ. Data from subject JL and the three DTI sequences is displayed in rapid succession from top to bottom. The mask used is cerebrospinal fluid mask.

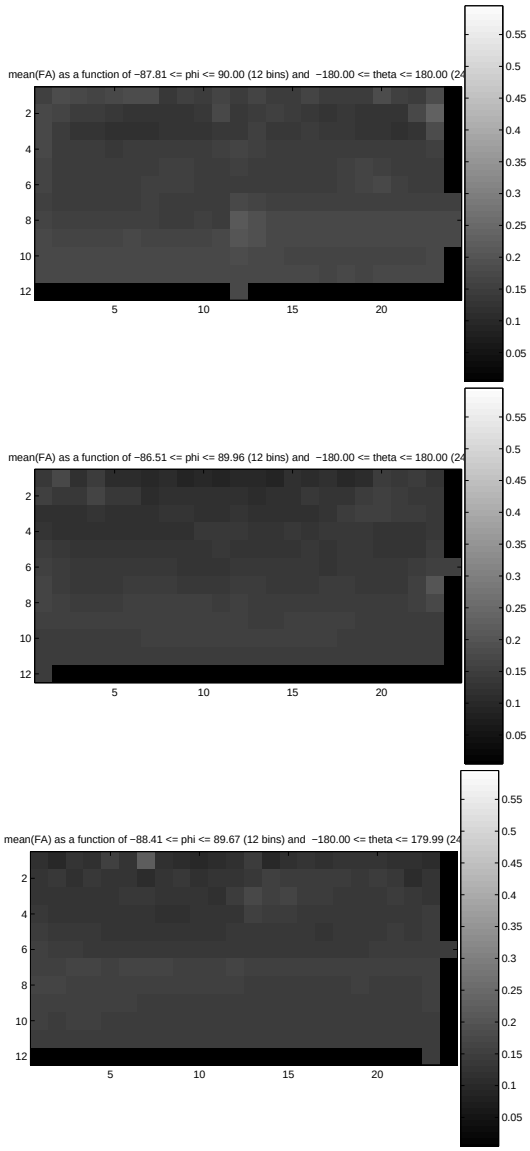

Figure 3.36: This plot demonstrates the mean values of FA in the same manner as the standard deviation plot above.

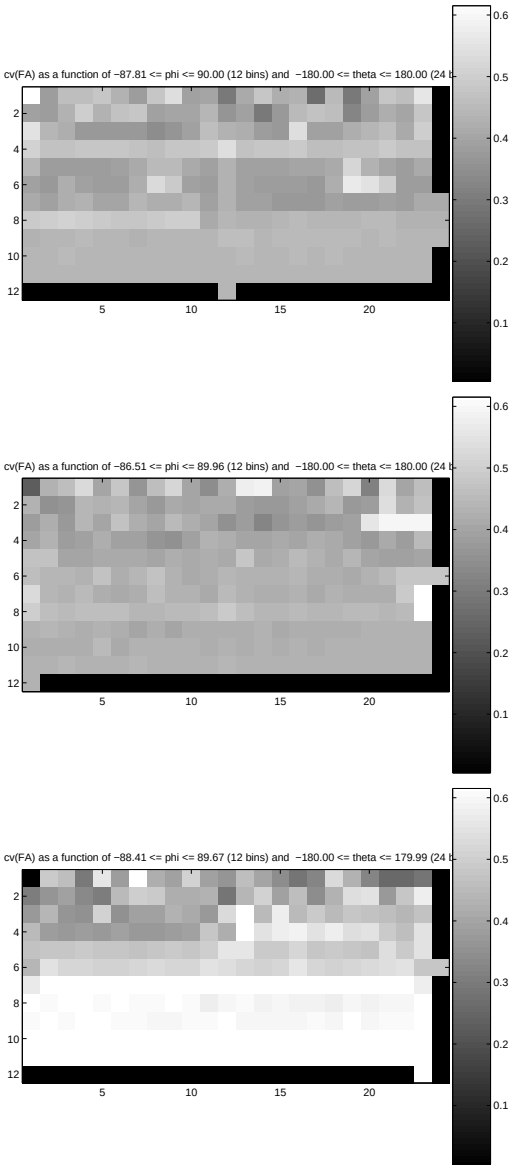

Figure 3.37: This plot demonstrates the coefficient of variation, CV, of the FA values in the same manner as the standard deviation plot above. $cv(FA) = std(FA)/mean(FA)$. That is the standard deviation relative to the mean value. The CV is useful when there are variations in the mean values.

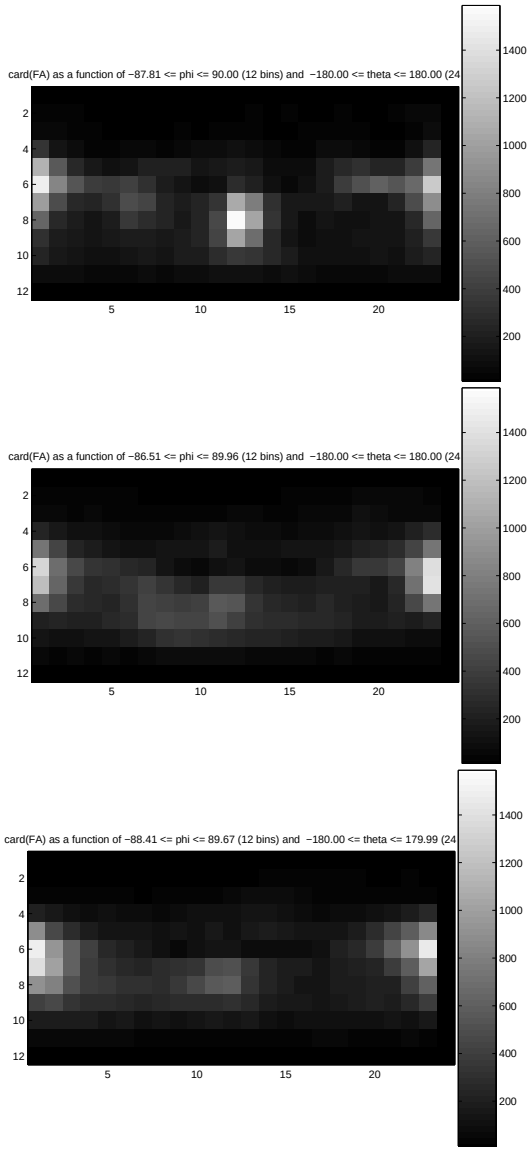

Figure 3.38: This gray scale plot demonstrates how many voxels that have the same properties for the θ and ϕ angles.

3.8 Color-coding of the FA maps

Others (Sarah Brockstedt, Lund) have discovered a marginal difference between DTI acquisition schemes with many directions and few averages compared to few directions and many averages by color-coding the FA map. This can be achieved when the eigenvectors in the different directions is given different colors. In the example below x-direction (V_x) is red, y-direction (V_y) is green and z-direction (V_z) is blue. The color intensity is given by the FA value.

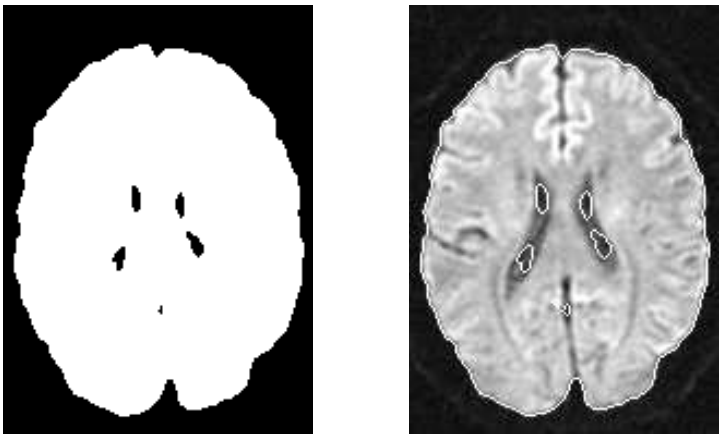

Figure 3.39: Left image: ROI determined to calculate FA and directional information from the eigenvectors and eigenvalues. Right image: The outer contour of the brain from the ROI. Data from subject OH and the sequence contains 25 diffusion directions and 2 NEX.

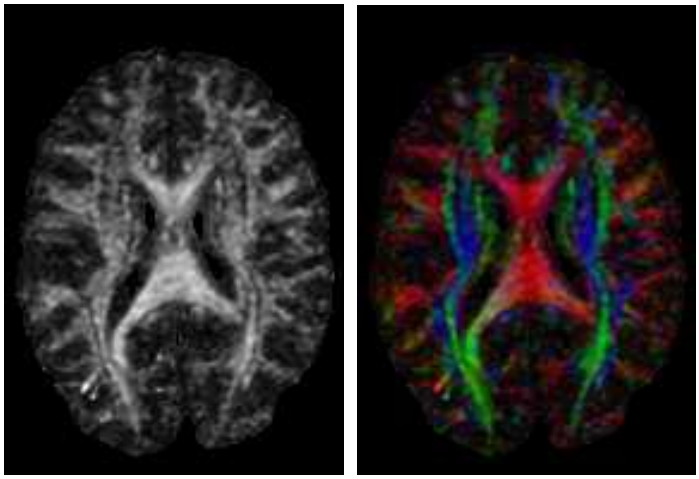

Figure 3.40: FA map to the left and the color-coded map to the right. Both maps showing subject OH and 25 diffusion directions and 2 NEX.

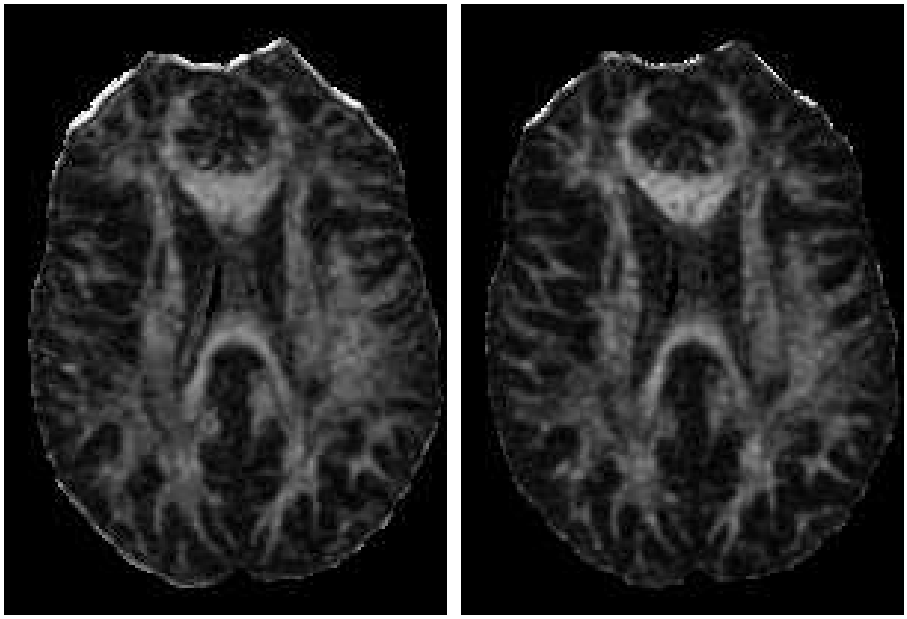

Figure 3.41: FA map to the left with 6 diffusion directions and 8 NEX and FA map to the right with 25 directions and 2 NEX. Both maps showing subject EK.

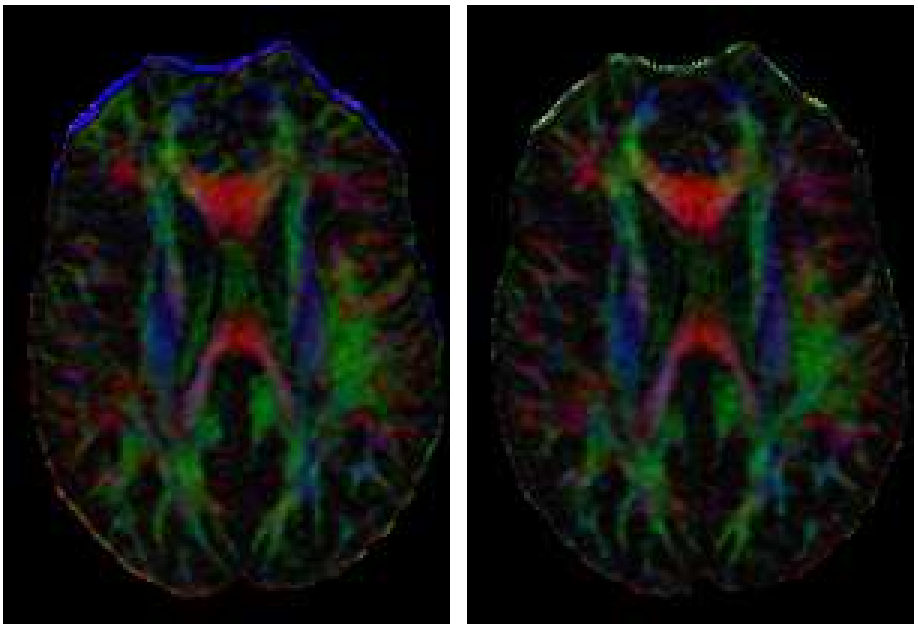

Figure 3.42: Color-coded map to the left with 6 diffusion directions and 8 NEX and color-coded map to the right with 25 directions and 2 NEX. Both maps showing subject EK.

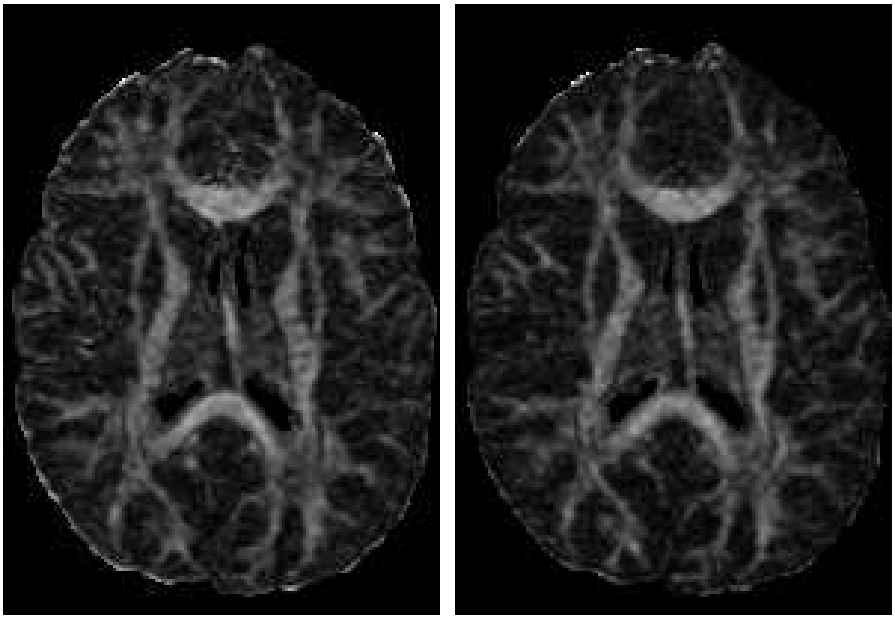

Figure 3.43: FA map to the left with 6 diffusion directions and 8 NEX and FA map to the right with 25 directions and 2 NEX. Both maps showing subject OB.

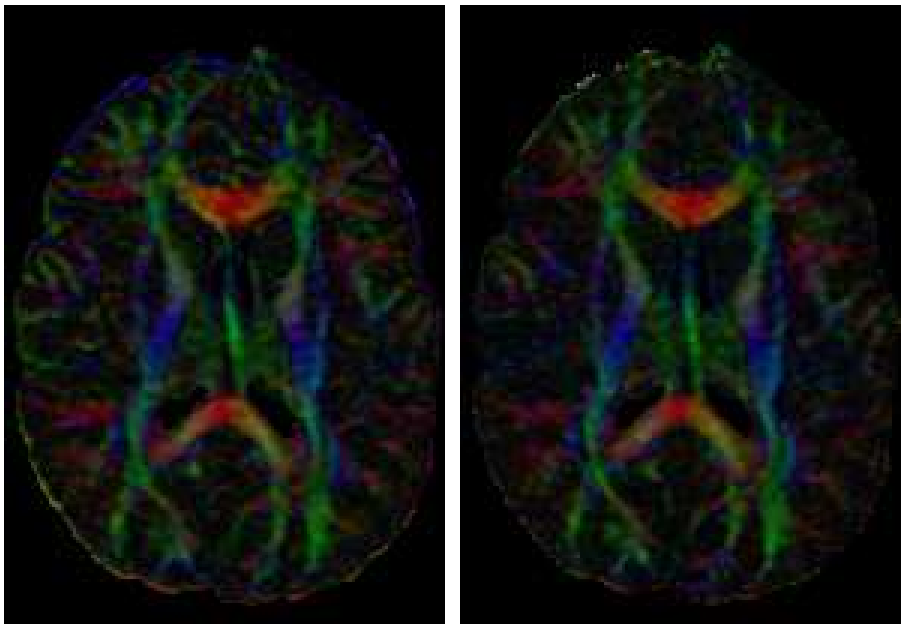

Figure 3.44: Color-coded map to the left with 6 diffusion directions and 8 NEX and color-coded map to the right with 25 directions and 2 NEX. Both maps showing subject OB.

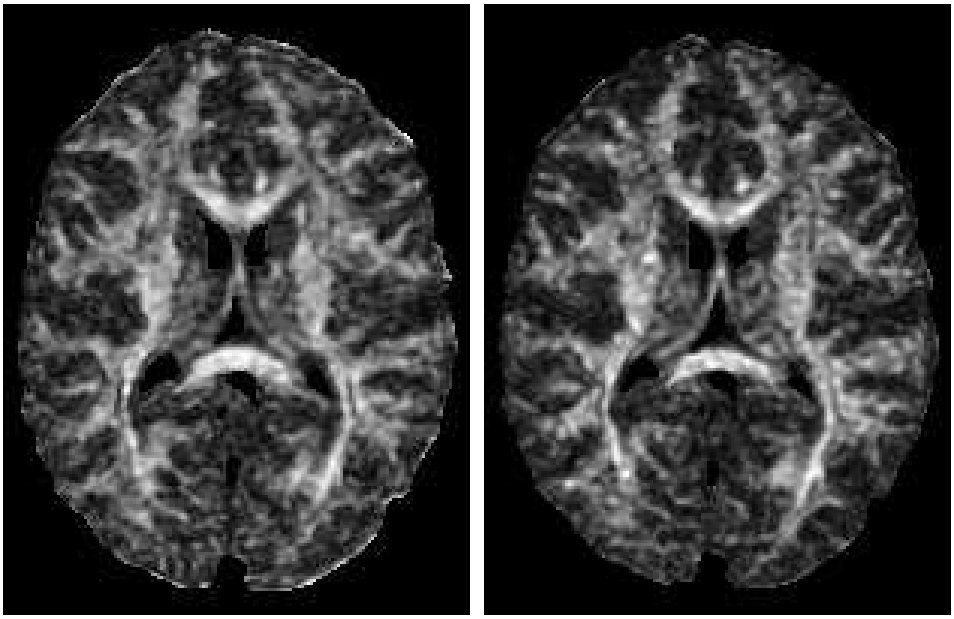

Figure 3.45: FA map to the left with 6 diffusion directions and 8 NEX and FA map to the right with 25 directions and 2 NEX. Both maps showing subject JL.

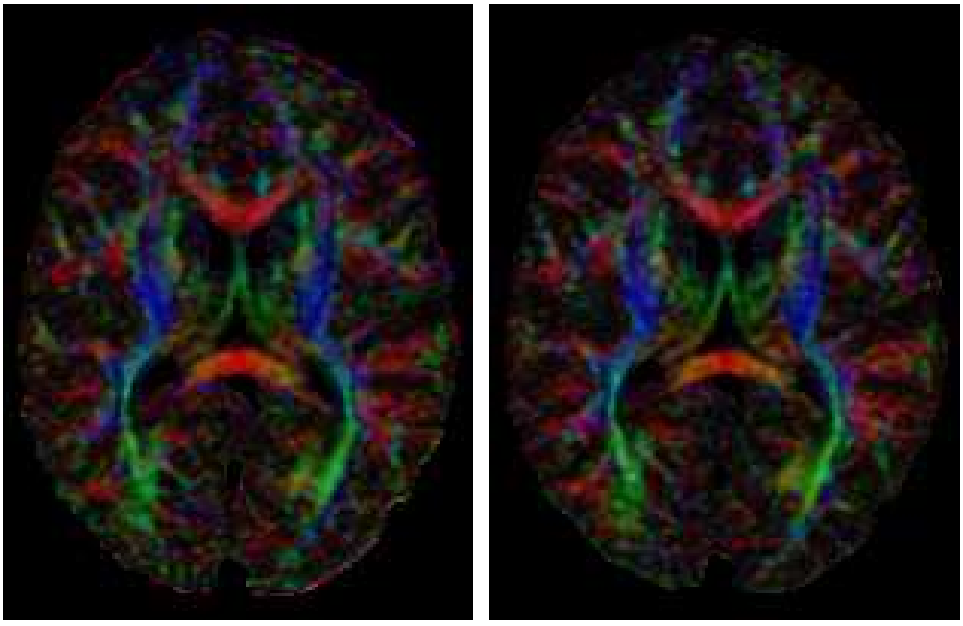

Figure 3.46: Color-coded map to the left with 6 diffusion directions and 8 NEX and color-coded map to the right with 25 directions and 2 NEX. Both maps showing subject JL.

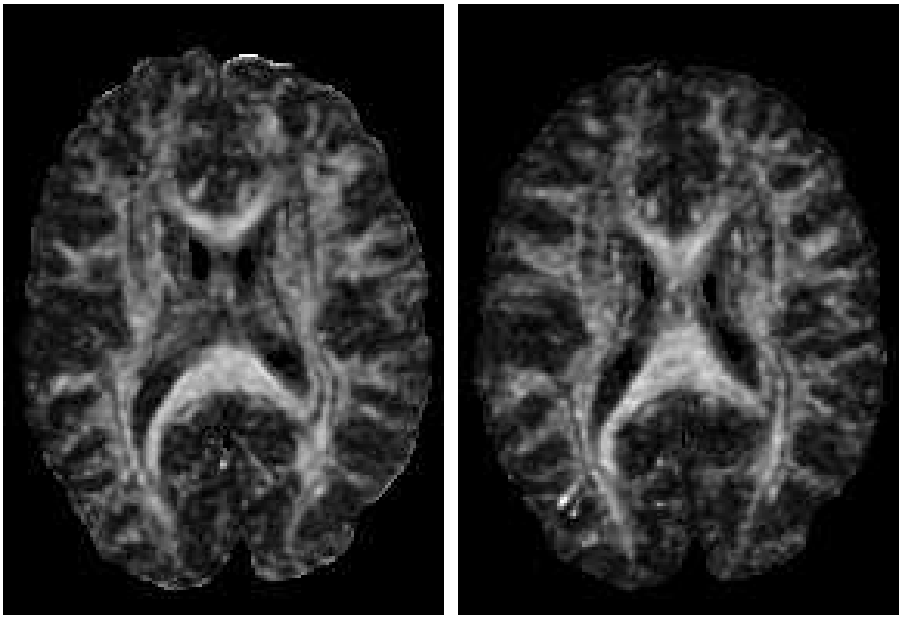

Figure 3.47: FA map to the left with 6 diffusion directions and 8 NEX and FA map to the right with 25 directions and 2 NEX. Both maps showing subject OH.

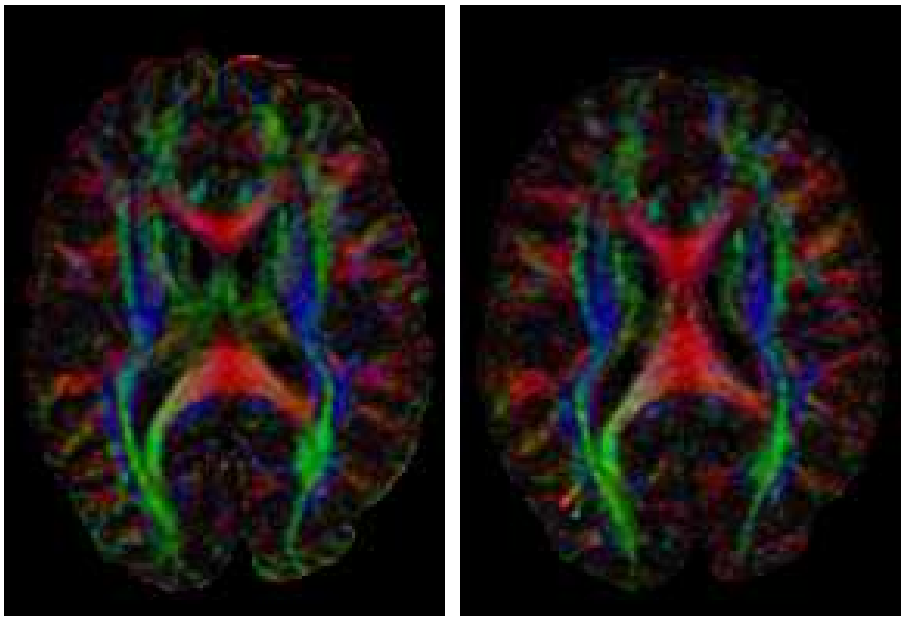

Figure 3.48: Color-coded map to the left with 6 diffusion directions and 8 NEX and color-coded map to the right with 25 directions and 2 NEX. Both maps showing subject OH.

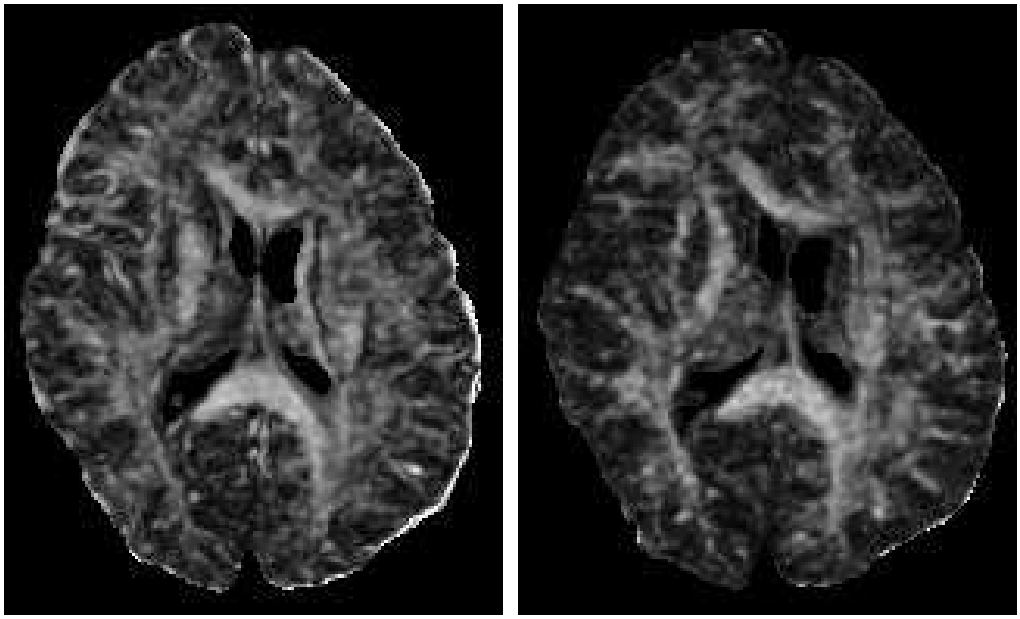

Figure 3.49: FA map to the left with 6 diffusion directions and 8 NEX and FA map to the right with 25 directions and 2 NEX. Both maps showing subject SA.

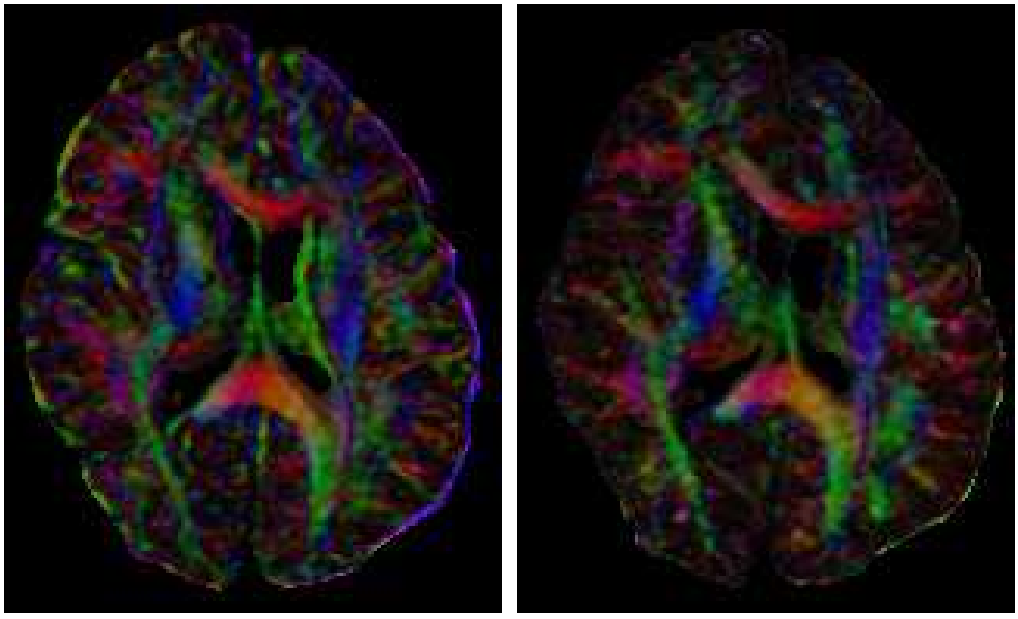

Figure 3.50: Color-coded map to the left with 6 diffusion directions and 8 NEX and color-coded map to the right with 25 directions and 2 NEX. Both maps showing subject SA.

3.9 Increased number of directions with constant NEX

By doing the same analysis as above on two sequences with different number of diffusion sensitizing directions and keeping the NEX constant, we want to ascertain that the SNR will increase with increasing number of directions. This time analysis is done only for FA in white matter. See table 3.3 and figure 3.51.

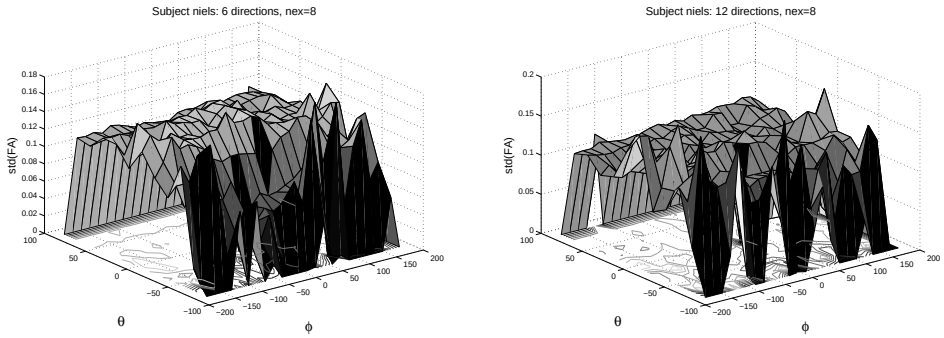

Figure 3.51: This 3D plot shows the standard deviation for the FA values as a function of the azimuth θ and elevation ϕ for the largest eigenvector. The scanner used is a Siemens and the acquisition matrix is 128×128. The plot at the top of the figure shows the results for the scanner image parameter sequence 6 directions and 8 NEX, the bottom plot 12 directions and 8 NEX. That means that the number of diffusion sensitizing directions has increased while the NEX has been held constant. The voxels which is chosen to evaluate the FA are taken from the white matter mask.

TN	6dir8NEX	12dir8NEX
std	0.0268	0.0208
cv	0.2177	0.2046

Table 3.3: This table shows the standard deviation and the coefficient of variation for the FA values for subject TN. The acquisitins in this data set has been recorded at a Siemens scanner, with a acquisition matrix 128×128 and two different acquisition schemes. The first is 6 directions and 8 NEX and the second one is 12 directins and 8 NEX. The results from this experiment shows that increasing the number of directions only, and keeping the NEX constant, will lower the standard deviation of the FA. That means that the SNR is higher and that the quality of the acquisitions increases when the number of directions increases. This is as expected.

3.10 FMRIB Software Library and Eddy Current Correction

FSL is a comprehensive library of functional and structural brain image analysis tools, written mainly by members of the Image Analysis Group, FMRIB, Oxford, UK. For details see [36] and [37].

With this software library it is possible to do the FA calculations as has been done in the work of this thesis in an easy and user-friendly way with GUI's (Graphical User Interface). In addition it is possible to do eddy current correction on the image volumes, before FA is calculated. As expected eddy current correction increases contrast and makes the image smoother. An example of FA images is calculated with FSL from the same dataset as used in our work using subject OB. Only the results from the sequences 6 directions and 8 NEX and 25 directions and 2 NEX will be presented. See the figures 3.53, 3.54 and 3.52.

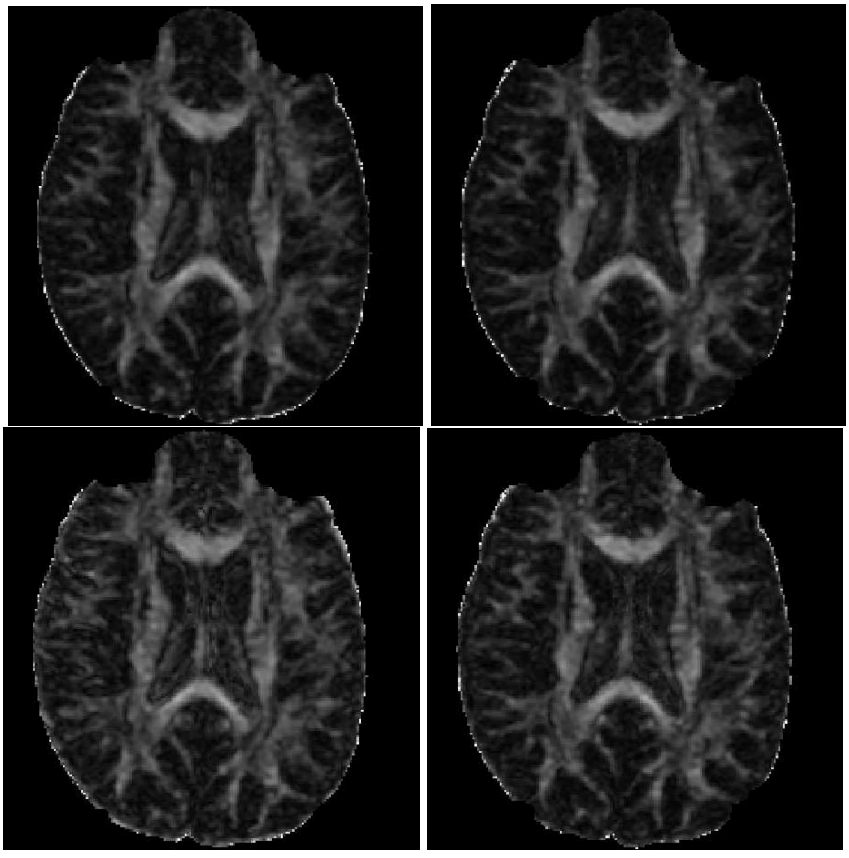

Figure 3.52: First row shows with ecc and second row without. First column shows 6dir 8NEX and second column shows 25dir 2NEX.

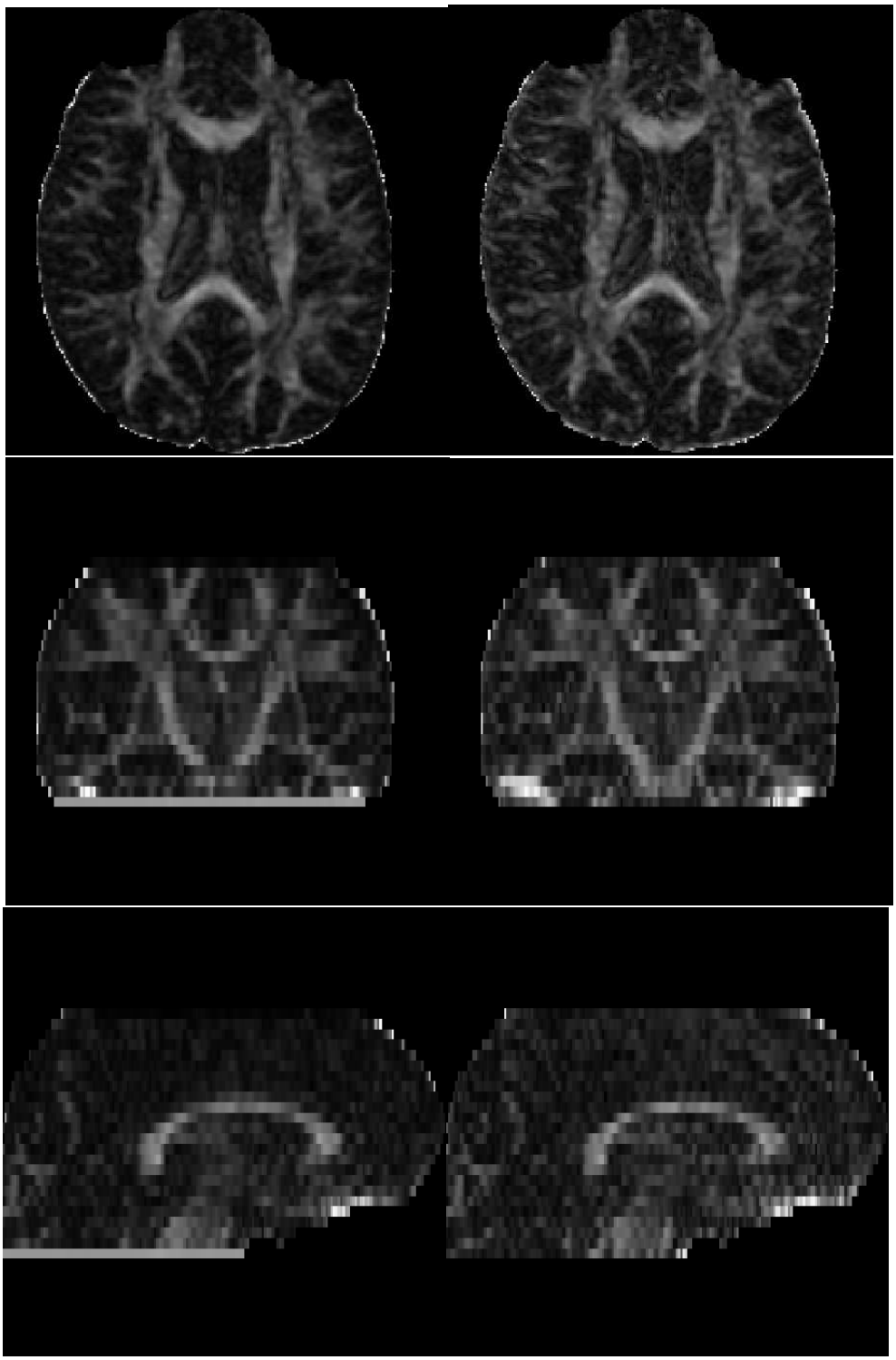

Figure 3.53: First row shows an axial slice, the second row shows a coronal slice and the third row shows a sagittal slice .Left column with eddy current correction and right column without. The sequence is 6 directions and 8 NEX.

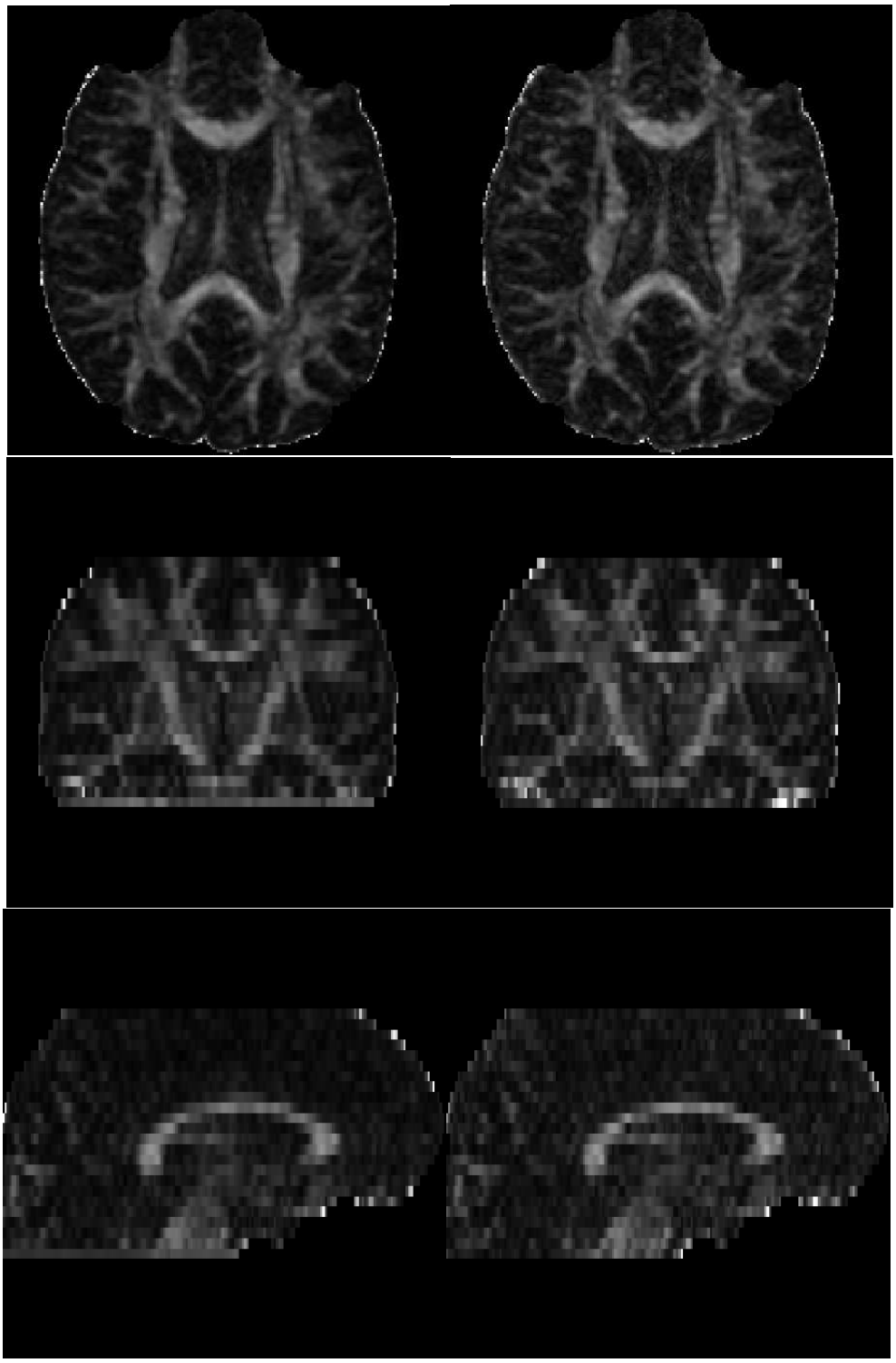

Figure 3.54: First row shows an axial slice, the second row shows a coronal slice and the third row shows a sagittal slice .Left column with eddy current correction and right column without. The sequence is 25 directions and 2 NEX.

3.11 Summary of our results

Standard deviation of the FA values From the results of the calculation of the standard deviation of tissue specific FA, we found that the sequence with K=6 and NEX=8 had slightly lower CV value than the other sequences for every subject. However, this difference in CV compared to the other protocols was very small and could not in itself bring a clear conclusion to our problem.

The 3D plots By careful inspection of the 3D plots, we found no visual difference large enough to make any conclusions in favor of one DTI acquisition scheme in favor of the others.

The color-coded images For subject EK it is possible to see a neater and more distinct structure and a more precise coloring in the image with directions=25 and NEX=2 than for the image with directions=6 and NEX=8. This is especially clear at nine o'clock.

Subject OB at nine o'clock shows a more unambiguous, precise or unique coloring and the image is more homogeneously colored for directions=25 and NEX=2.

For subject JL it is clear that the image showing directions=25 and NEX=2 is more smoothly delineated. This is easiest to see in the central triangular between genu and splenium.

Subject OH has very different coloring in the central parts of the image. The central triangular seems to connect the genu and splenium together for directions=25 and NEX=2 than for the directions=6 and NEX=8, where the central part is green.

For subject SA the genu has a more mixed coloring for directions=25 and NEX=2, but the splenium and the central triangular seems more continuous for directions=6 and NEX=2.

For all of the subjects the boundary seems more exposed to distortions for the image showing directions=25 and NEX=2 than for the other.

4

Discussion

The signal in MR-DTI is both weak and vulnerable to noise and artifacts, such that the determination of the diffusion tensor **D** and the FA-index are subject to uncertainty and errors. Among several methods that can be applied to improve signal strength and reduce noise we chose to explore if there were any potentially significant differences between DTI head acquisitions obtained (for a fixed measurement time) when the number of diffusion sensitizing directions (K) was maximized compared to the situation where the number of excitations (NEX) was maximized.

4.1 Main results

From our analysis we found that there was a slightly higher quality in white matter results using a protocol with K=6 and NEX=8 than for the protocols using K=13 and NEX=4 or K=25 and NEX=2.

However in his thesis [24] Skare concludes from his second paper [38] that: "Given the same total number of measurements, it is better to measure the diffusion in many directions rather than do more averages of DWIs in fewer directions. Because of noise, the eigenvalues are not rotationally invariant. The accuracy of the eigenvalues and diffusion anisotropy varies with the direction of the tensor relative to the image plane. The smaller the number of directions used, the larger the

variation." From our results, this conclusion is not clearly violated since the difference in $std(FA)/mean(FA)$ of white matter for the protocols (K=6 and NEX=8), (K=13 and NEX=4) and (K=25 and NEX=2) were very small, i.e. $CV(FA)_{wm}$ ranging from $0.279-0.319$, $0.285-0.357$ and $0.299-0.390$ respectively.

4.2 Strengths and weaknesses of our approach

4.2.1 Eddy current correction

Due to lack of time and software, we did not perform eddy current (EC) correction in our comparative study of protocols. As depicted in Section 3.10, demonstrating the effect of EC correction in a single subject OB (K=6 and NEX=8) and (K=25 and NEX=2), we see that EC correction increases contrast and details and makes the FA map smoother. To further explore the quality differences between high K or high NEX, EC correction should be done previous to tensor and FA calculations.

4.2.2 Determination of the ROI and the segmentation process

For tissue specific analysis the definition of region of interest (ROIs) is important. In our case with FA maps, it is not wise to use the FA images themselves as this would be using the dependent variable to define itself. This can definitely impede the identification of abnormal tissue such as white matter regions with low FA. Therefore it was decided to automate the definition of ROIs based on a T_2-weighted structural image. To our knowledge, probabilistic tissue segmentation of the S_0-image to obtain tissue specific FA-values has not previously been reported. Using the segmentor in SPM2 and simple thresholding, we obtained a large sample of GM, WM and CSF voxels that were in co-register with the other DTI acquisitions that were used to calculate the tensor **D** and the FA-values. The S_0 image from the protocol with K=6 and NEX=8 was used for segmentation, since it had the highest SNR among all of the S_0 images that were acquired.

Because the S_0-image data suffers from a substantially lower quality than a genuine 3D anatomy image (e.g. MPRAGE, 3D FLASH), the poor quality can possibly cause misclassification of tissues in the segmentation process. It is therefore an alternative to acquire a full 3D anatomic data set and later co-register with the DTI data. However, this would lead to higher examination times and may be hampered with mis-registration problems, if simple affine transformations were used as is most common [1].

Pfefferbaum and Sullivan has reported that systematically eroding or dilating the circumference of the ROI by eliminating or adding pixels, a margin of potential error in the segmentation process is demonstrated [39]. They state that:

"This draws into question use of global analysis approaches, such as statistical parametric mapping (SPM), based on resizing of brain parenchyma to a common template without regard for partial voluming arising from mis-registration that can contribute significantly to DTI measures."

4.2.3 Advantages with many directions

Many diffusion sensitizing directions enables so-called diffusion spectrum imaging (DSI) which is an alternative yet effective approach for mapping the intravoxel structures of white matter, especially fiber crossings, using a circular spectral decomposition technique based on HARD MRI (Zhan *et al.* [40]). Another example which favor many diffusion sensitizing directions opposed to more averages of few directions, is high quality fiber tracking. It is necessary to encode the DTI acquisitions with many diffusion sensitizing directions to get more reliable trackings ([41]).

4.2.4 Suggestion for improvements

Apart from eddy current correction on the raw data before calculating the tensor and the FA index, better or more coils for parallel imaging ([42]) will certainly give better results, but depends on having the proper hardware in the MR scanner. Another quality test in protocol comparison will be fiber tracking evaluation. By the recently available synthetic DTI datasets [43], the goodness of a given tracking algorithm could be established, which could then be applied to a real DTI data set from a single subject acquired with different DTI protocols.

4.3 Future work – extending the assessment to fiber tracking results

Further analysis would be to test the three DTI acquisition schemes on results from fiber tracking. There exists several methods for fiber tractography based on DTI data [44] [45] [46] [47] [48] [49] [50] and [51] . One of them is implemented in FSL by FMRIB, which does probabilistic tracking ([36]).

4.3.1 Probabilistic tracking

Oxford Center for Functional Magnetic Resonance Imaging of the Brain, FMRIB, has developed a technique for characterizing the uncertainty associated with parameter estimates in diffusion weighted MRI, and for propagating this uncertainty

through the diffusion weighted data. This allows computation of probability distributions on the location of the dominant fiber pathway such that it is possible to quantify the belief in the tractography results.

Analysis of diffusion weighted data normally involves the fitting of a model of local diffusion to the data in each voxel. A weakness in such an approach is that the assumed model is of the diffusion profile and not the underlying fiber structure which are the parameters that are of real interest. Because there has been no model proposed to predict, adopting a Bayesian framework, how a specific structure or distribution of fiber directions within a voxel will reflect itself in the measured diffusion weighted MR signal, therefore, any attempt to recreate the fiber structure from such a profile is essentially an educated guess. Another issue is that even when fitting a model of local diffusion, the resulting parameters have uncertainty associated with them.

FMRIB have presented a method for the full treatment of such an uncertainty. They have shown, using Bayes' equation along with well established methods for its numerical solution, that it is possible to form a complete representation of the uncertainty in the parameters in any generative model of diffusion, in the form of posterior probability density functions on these parameters.

They then consider the uncertainty at a global level by outlining the theory behind moving from the probability density functions (pdfs) on local principal diffusion direction to an estimate of the probability distribution on global connectivity. They choose to use a simple partial volume model to model local diffusion. The reason for this choice is that it maximizes the chance that the effect of diverging or splitting fibers will be seen as uncertainty in the principal diffusion direction, and not as a change in the diffusion profile. This is so because such a model only allows for a single fiber direction within a voxel.

The next stage is to define a model of global connectivity. This is done with *streamlining algorithms*. That is, given absolute knowledge of local fiber directions, connectivity is assumed between two points if, and only if, there exists a connected path between them through the data. They simply allow for uncertainty in fiber direction when computing streamlines by effectively repeatedly sampling local pdfs to create streamlines, and regarding these streamlines as samples from a global pdf. They choose to compute the local pdfs in a rigorous fashion given the MR data.

An important result of their procedure is that the recovered connectivity distributions are strictly probability distributions on the connected pathway through dominant fiber directions. That means that there is no explicit representation of splitting or diverging fibers in either the local or global model. They are strictly inferring that the effect of fiber divergence within a voxel (e.g. branching/crossing fibers) must reveal itself as uncertainty in the principal diffusion direction. However, because fiber divergence within a voxel is treated as uncertainty in principal

diffusion direction, this sensitivity to diverging and branching fibers will be dependent on the experimental design. In general, the more information in the MR measurements, the lower the uncertainty in principal diffusion direction.

This makes it possible to model tractography also in grey matter corticothalamic projection neurons. Even though the FA is low here.

Using the computational framework for probabilistic fiber tracking, it would be possible to assess the effect of using different DTI image acquisition protocols (i.e. K=6 and NEX=8 vs. K=13 and NEX=4 vs. K=25 and NEX=2). However, this would require much more computer resources and time for analysis than was available in this project. We have therefore limited ourself to make a few simple experiments with the probabilistic tracking methods applied to our own data.

4.3.2 Preliminary results from probabilistic tracking applied to data from subject AL

We have done probabilistic tracking on one dataset, subject AL, using a modified acquisition protocol on the 1.5 T GE Signa Echospeed scanner at HDS, with K=25 and NEX=2. For this case 5 T_2-weighted (b=0) images were recorded in order to improve tensor calculations (cf. [31] and [38]). We also increased the number of slices to 34, using a k-space acquisition matrix of 96×96 (interpolated to 256×256 display matrix), and isotropic voxel size of 2,3×2,3×2,3 mm^3. We will here remark that most published studies of fiber tracking employ 60 or more slices with about 2.0 mm slice thickness (e.g [52]). The shell-script used for the tensor calculations and tracking (accessing the routines in FDT*/FSL) is given in Appendix B.11.

Figure 4.1 depicts a detail from the experimental results showing probabilistic fiber tracks in the anterior corpus callosum region, superimposed on the corresponding FA map. Initially, a bar-shaped seed-mask was manually placed along the whole corpus callosum in a para-sagittal plane. In Fig. 4.1 we see the intersection of this mask with an axial slice (small yellow rectangle) close to the genu part of the corpus callosum). The algorithms implemented in FDT first performs Markov Chain Monte Carlo sampling to build up distributions on diffusion parameters at each voxel of the brain (consuming about 20 hours on our Linux machine!). Then FDT was used to generate probabilistic streamlines in each voxel, and finally compute a connectivity distribution, as seen in Fig. 4.1. All brain voxels will have a value (though many of these may be zero) *representing the number of samples that pass through that voxel from the seed mask*. Connectivity distributions from multiple seed voxels in the mask are summed to produce this output,

*FDT–tools for low-level diffusion parameter reconstruction and probabilistic tractography (http://www.fmrib.ox.ac.uk/fsl/fdt)

and the connectivity values depend on the number of voxels in the seed mask. Thus, the brightness of a pixel, say *p*, representing a streamline in Fig. 4.1 reflects the area (number of voxels) within the seed mask that are probably connected to *p*.

At this early stage of our tracking experiments good results and proper evaluation is hard to obtain, partly because we had little time on the scanner to experiment with higher spatial resolution and whole brain coverage, combined with good data quality. One flaw with the acquisition of the present dataset was that our axial slices were hampered with some left-right over-folding artifacts. By switching the direction of the phase encoding and frequency encoding imaging gradients in follow-up experiments, this artifact was not present. However, these new DTI-acquisitions were recorded for simple FA-calculations, and had larger slice thickness, less number of slices, and were spatially not appropriate for tracking experiments.

We will, as a next step, study the possibility of modifying our DTI acquisition protocol to be better suited for fiber tracking, and such that the time consumption of the sequence is compatible with clinical use.

As shown in Fig. 4.1 the correctness/quality of the fiber tractography images are difficult to interpret, and a more rigorous study should include DTI protocols with higher spatial resolution.

4.4 Conclusion

From our data, which are sparse, and evaluation methods, we conclude that the quality of the resulting diffusion tensor **D** *and the FA maps are about the same using protocols that favors number of directions (large K) traded with number of averages (few NEX), and protocols that favors number of excitations (high NEX) traded with number of directions (small K).*

Since a large K enables more sophisticated analysis (e.g. diffusion spectrum imaging, DSI) we recommend a protocol with many diffusion sensitizing directions. This is also in accordance with the latest recommendation from the vendor of the scanner (i.e. after upgrade to Echospeed gradient system), where K=25 and NEX=1 are prescribed in their standard DTI protocol.

FA with seed-mask

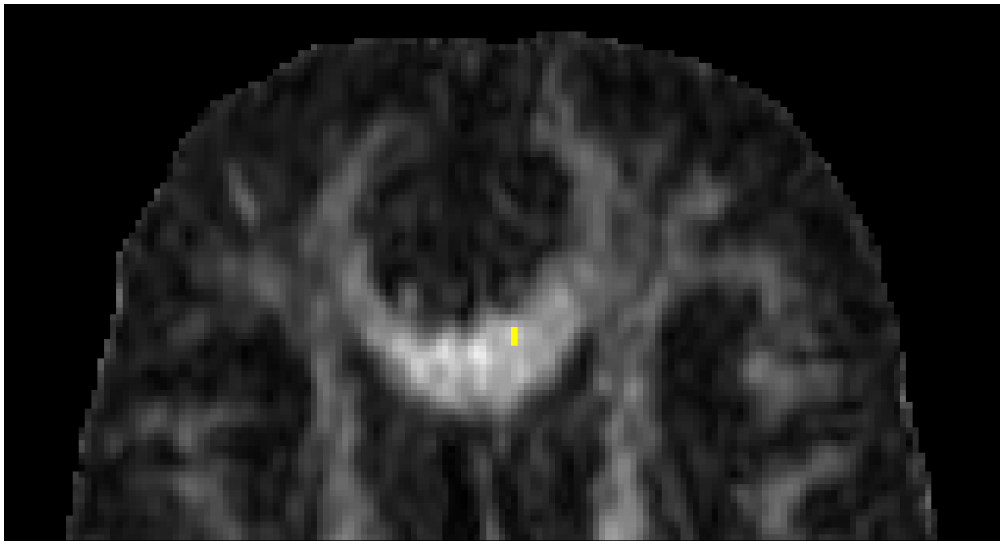

Tracking superimposed on FA

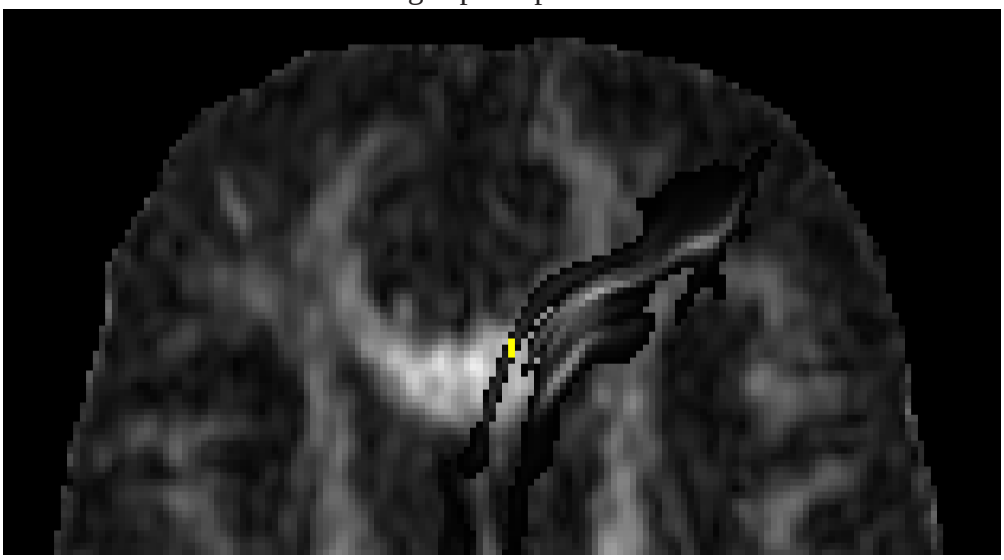

Figure 4.1: The results from probabilistic fiber tracking using the FDT/FSL software from Oxford's FMRIB on MR-DTI data acquired in subject AL. The spatial connectivity matrix, shown as streamlines superimposed on the FA image in the anterior part of corpus callosum (CC), is related to a bar-shaped seed mask manually placed along the CC. Part of this seed-mask (small yellow rectangle) can be seen where the mask intersects one of the axial slices (9/32)

A

Programs used in the work of this thesis

A.1 MATLAB

MATLAB [53] is a high-level technical computing language and interactive environment for algorithm development, data visualization, data analysis, and numerical computation. Using MATLAB, one can solve technical computing problems faster than with traditional programming languages, such as C, C++ and Fortran.

One can use MATLAB in a wide range of applications, including signal image processing, communications, control design, test and measurements, financial modeling and analysis, and computational biology. Add-on toolboxes (collections of special-purpose MATLAB functions, available separately) extend the MATLAB environment to solve particular classes of problems in these application areas.

MATLAB provides a number of features for documenting and sharing of work. One can integrate your MATLAB code with other languages and applications, and distribute MATLAB algorithms and applications.

A.2 nICE

nICE – Image Control and Evaluation [32] – is a medical viewing, analysis and processing package developed with a view to ease of use and high performance an a standard Windows platform. In addition to a wide range of basic image processing and analysis functions, nICE provides comprehensive functionality for dynamic image analysis (e.g. perfusion) and processing/display of

functional MRI (fMRI) data. For this purpose, nICE provides easy data transfer to other fMRI analysis software packages.

We used nICE to load the DTI images as DICOM-files and save them as SPM/Analyze format. Separate volumes was made for each of the diffusion sensitizing directions.

A.3 SPM2 (Statistical Parametric Mapping)

The SPM [54] was originally developed by Karl Friston and is a software package for the analysis of brain imaging data sequences. The sequences can be a series of images from different cohorts, or time-series from the same subject. SPM is based on MATLAB functions and subroutines. Routines for probabilistic segmentation of high resolution magnetic resonance brain images is also implemented. Segmentation divides the brain into to gray matter (GM), white matter (GM) and cerebrospinal fluid (CSF) and other parts based on the image intensity.

The segmentation algorithm utilizes a priori probability images of GM, WM and CSF (range 0-1). Before segmentation each voxel in the image is mapped to its equivalent location in the a priori probability images through a spatial transformation.

The iterative segmentation algorithm is based on maximum likelihood 'mixture model' clustering algorithm. The algorithm is terminated when the change in log-likelihood from the previous iteration becomes negligible.

A.4 MRI-TOOLBOX

The toolbox makes it possible to, among other things, import the segmented tissue volume from analyze-format into MATLAB as a *.mat file. This makes it convenient to work with the segmented tissue volumes in MATLAB. The mri-toolbox can be downloaded from here [55]. Search for mri-toolbox.

B

MATLAB-code and additional shell scripts

B.1 diffusionellipsoid.m

```
r = diffusionellipsoid(D, xrot, yrot, zrot, n)

% Axis rotation
Rx = [1, 0, 0; 0, cosd(xrot), sind(xrot); 0, -sind(xrot), cosd(xrot)];
Ry = [cosd(yrot), 0, -sind(yrot); 0, 1, 0; sind(yrot), 0, cosd(yrot)];
Rz = [cosd(zrot), sind(zrot), 0; -sind(zrot), cosd(zrot), 0; 0, 0, 1];

R = Rz*Ry*Rx;  % Resulting rotation matrix

[E, lambda] = eigs(D);
L = diag(lambda);
[x,y,z] = lcl_ellipsd(L', E, n);
D_rot = R*D*(R');
[E_rot, lambda_rot] = eigs(D_rot);
L_rot = diag(lambda_rot);
[x_rot,y_rot,z_rot] = lcl_ellipsd(L_rot', E_rot, m);

surfc(z,y,x)                % Original diffusion ellipsoid, before spatial transformation
surfc(z_rot,y_rot,x_rot)  % Diffusion ellipsoid after reorientation of tensor


[x,y,z] = lcl_ellipsd(smax,nrm,n)
%   ELLIPSD(SA,NRM,N) plots ellipsoid with
%   semiaxes vector SA=[SAX SAY SAZ] and
%   axes orientation given in the matrix NRM.
%   N specifies dimension of coordinate matrices
%   X, Y, Z (all NxN matrices
```

B.2 runme.m

```
wd = pwd;
disp( 'Load DTI data from DICOM format...');
cd Data\dti\KETIL_20040604\SA\SA25dir2NEX

dti_foer_nedskalering = double( loaddti( 'im',24,26,1,true ));
cd( wd );
clear wd;

% Makes a section of the volume to place a limitation on the amount of
% memory used in the calculations
disp( ' Scaling down dataset...' );
dti = dti_foer_nedskalering(:,40:235,51:210,:); %SA

disp( '  Computing diffusion-tensor for each voxel...' );
D = difftensorlsq( dti );

disp( '   Computing norms from diffusion-tensor...' );
disp( '    Computing FA norm...' );
img_fa = dtnorm( D, 'fa' );
```

For `loaddti.m` see B.3 page 92, for `difftensorlsq.m` see B.4 page 93 and for `dtnorm.m` see B.6 page 95.

B.3 loaddti.m

```
function dti = loaddti( fileprefix, slices, directions, offset, debug )
% LOADDTI Load DTI volume data fra DICOM files
%   LOADDTI( fileprefix ) loads the DICOM-files beginning with 'prefix'
%   from disk.
%
%   LOADDTI( fileprefix, slices ) assumes there are 'slices' slices of
%   images in the dataset. Default is 19.
%
%   LOADDTI( fileprefix, slices, directions ) assumes there are
%   'directions' directions in the dataset. Default is 7.
%
%   LOADDTI( fileprefix, slices, directions, offset ) assumes the
%   first image is named 'sprintf('%s%d', fileprefix, offset)'. Default
%   is 1.
%
%   LOADDTI( fileprefix, slices, directions, offset, debug ) shows
%   information about the loading process if 'debug' is true.
%
%   dti = LOADDTI(...) returns a volume containing the loaded data.
%   size( dti ) = 'directions' * rows * cols * 'slices', where rows and
%   cols are the number of rows and columns in each of the
%   DICOM-images, and 'directions' and 'slices' are inputparameters.

switch ( nargin )
    case 1
        dti = loaddti( fileprefix, 19 );
        return;
    case 2
        dti = loaddti( fileprefix, slices, 7 );
        return;
    case 3
        dti = loaddti( fileprefix, slices, directions, 1 );
        return;
    case 4
```

```
        dti = loaddti( fileprefix, slices, directions, offset, false );
        return;
end

if (debug)
    disp('Loading DTI data...');
end

for filenumber = offset : slices*directions
    filename = sprintf('%s%d', fileprefix, filenumber);

    dir = floor( (filenumber - offset) / slices ) +1;
    slc = mod( (filenumber - offset) , slices ) +1;

    info = dicominfo( filename );
    dti( dir,:,:,slc) = dicomread( info );

    if (debug)
        disp( sprintf( ' Reading file %s...', filename ));
        disp( sprintf( '  Direction  = %d', dir ));
        disp( sprintf( '  Slice      = %d', slc ));
        disp( sprintf( '   File info' ));
        disp( sprintf( '    Filesize   = %d', info.FileSize ));
%        disp( sprintf( '    Minimum    = %d', info.SmallestImagePixelValue ));
%        disp( sprintf( '    Maximum    = %d', info.LargestImagePixelValue ));
        disp( sprintf( '    Resolution = %dx%d', info.Rows, info.Columns ));
        disp( sprintf( '    Date       = %s', info.FileModDate ));
    end
end
```

B.4 difftensorlsq.m

```
function D = difftensorlsq( dti )
% DIFFTENSTORLSQ Calculates a diffusion tensor volume from a dti volume
%   DIFFTENSTORLSQ( dti ) calculates a diffusion tensor for each
%   voxel in the dataset 'dti'. 'dti' is of resolution dirs x rows x
%   cols x slcs. Let rows x cols x slcs represent the complete MRI
%   volume being examined. From these dirs values for each voxel in
%   the volume we can compute [Westin et al.( 2002)] a diffusion
%   tensor. We will do this using Trygve Nilsens linear least squares
%   approach. See lecturenotes dated April 24.
%
%   D = DIFFTENSORLSQ( ... ) returns a diffusion tensor calculated for
%   each voxel in the volume. The tensor for each voxel will be a 3x3
%   matrix, and therefore size( D ) = 3 x 3 x rows x cols x slcs.

b = 1000;
g = scandir( size( dti,1 ));

%% Translate dataset to minimum 1 to later avoid log(0)
dti = dti - min(min(min(min( dti )))) +1;

%% Transform to correct scale
dti = log( dti );
for dir = 1:size( g,2 )
    y( dir,:,:,: ) = (dti( 1,:,:,: ) - dti( dir+1,:,:,: )) / b;
end

%% Calculate gamma-matrix
for row = 1:size( g,2 )
```

```
    gamma(row,:) = reshape( g(:,row) * g(:,row)', [1 9]);
end

%% Remove duplicate columns to prevent singularity
gamma = uniquecols( gamma );

%% Precalculate matrix needed for analytical solution
M = inv( gamma' * gamma ) * gamma';

%% For each voxel, solve minimization analytically
for row = 1:size( dti,2 )
    for col = 1:size( dti,3 )
        for lvl = 1:size( dti,4 )
            delta(:,row,col,lvl) = M * y( :,row,col,lvl );
        end
    end
end

%% Convert vector pr voxel to symmetric matrix pr voxel
D( 1,1,:,:,: ) = delta( 1,:,:,: );
D( 1,2,:,:,: ) = delta( 2,:,:,: ) * 0.5;
D( 1,3,:,:,: ) = delta( 3,:,:,: ) * 0.5;
D( 2,2,:,:,: ) = delta( 4,:,:,: );
D( 2,3,:,:,: ) = delta( 5,:,:,: ) * 0.5;
D( 3,3,:,:,: ) = delta( 6,:,:,: );
D( 2,1,:,:,: ) = D( 1,2,:,:,: ); %% Symmetric
D( 3,1,:,:,: ) = D( 1,3,:,:,: ); %% Symmetric
D( 3,2,:,:,: ) = D( 2,3,:,:,: ); %% Symmetric

%% Remove duplicate columns from M
function U = uniquecols( M )
U = [];
for col = 1:size( M,2 )
    if ~ismember( M(:,col)', U', 'rows' )
        U = [U, M(:,col)];
    end
end
```

For scandir.m see B.5 page 94.

B.5 scandir.m

```
function g = scandir( dircount, scannertype )

%% Do not count b=0 direction
dircount = dircount -1;

switch( dircount )
    case 6
        g = load( 'ge_6.txt' )';
        return;
    case 13
        g = load( 'ge_13.txt' )';
        return;
    case 25
        g = load( 'ge_25.txt' )';
        return;
end
% The *.txt fils has been made from the information in the tensor.dat file
```

B.6 dtnorm.m

```
function V = dtnorm( D, normhandle )
% DTNORM Computes a volume norm for a diffusion tensor volume
%   DTNORM( D, normhandle ) computes a norm from the diffusion tensor
%   stored in each voxel of 5D 'D', using the handle to the matrixnorm
%   'normhandle'. 'normhandle' is the name of a function in the 'private'
%   subdirectory (without the extension).
%
%   V = DTNORM( ... ) returns a volume where each voxel contains the
%   norm of the corresponding diffusion tensor in 'D'. If size( D ) =
%   m x n x rows x cols x slcs, then size( V ) = rows x cols x slcs.
%
%   Example:
%       V = dtnorm( D, 'linear' );

normhandle = str2func( normhandle );

for row = 1:size( D,3 )
    for col = 1:size( D,4 )
        for lvl = 1:size( D,5 )
            d = D( :,:,row,col,lvl );
            V( row,col,lvl ) = feval( normhandle, d );
        end
    end
end
```

B.7 fa.m

```
function value = fa( D )
lambda = flipud( sort( eig( D )));

value = 1/sqrt(2) * (sqrt( (lambda(1)- lambda(2))^2 + ...
 (lambda(2)- lambda(3))^2 + (lambda(1)- lambda(3))^2) / ...
   sqrt( lambda(1)^2 + lambda(2)^2 + lambda(3)^2));
```

B.8 makemask.m

```
function mask = makemask ( volume, treshold, subject )
% MAKEMASK makes a binary mask from the volume 'volume' with threshold from 0 to
% 1 and scales the volume to fit the img_fa volume of subject 'subject'.
%
% Example: mask = makemask( img_white, 0.95, 'JL' );  gives us the binary mask from
% the volume img_white with treshold 0.95 and scales the volume for subject 'JL'.

% Author: Ketil Oppedal May 2004
% revised: October 2004

volume = volume/max(max(max(volume)));

for i = 1:size(volume,3)
    volume_rot = rot90(volume(:,:,i));
    volume_rot_tresh = im2bw(volume_rot(:,:), treshold);
    mask(:,:,i) = reshape(volume_rot_tresh(:,:), size(volume,1), size(volume,2), 1);
end
```

B.9 fa-plotting

```
function fa_plotting_20041018(subj_id, nof_diff_dirs, nex)
```

```
DELTA_DEG = 15; % Discretization ("binning") of the phi and theta angles

% for subject OB
% loading data
data = '.\ketils_workspaces\20040214\OB6dir8NEX.mat';
load(data)

% importing the segmented brain volumes from analyze format
[gm, xx] = avw_img_read('g:\Ketil\m-files\Data\dti\KETIL_20040214\OB\SPM_OB6dir8NEX\b0_seg1');
[wm, xx] = avw_img_read('g:\Ketil\m-files\Data\dti\KETIL_20040214\OB\SPM_OB6dir8NEX\b0_seg2');
[csf, xx] = avw_img_read('g:\Ketil\m-files\Data\dti\KETIL_20040214\OB\SPM_OB6dir8NEX\b0_seg3');

% making the tissue specific mask
gm_mask = makemask( gm.img, 0.925, 'OB' );
wm_mask = makemask( wm.img, 0.925, 'OB' );
csf_mask = makemask( csf.img, 0.925, 'OB' );

% Make column vectors
img_fa_vec = reshape(img_fa, prod(size(img_fa)), 1);
vecoord_ph_vec = reshape(vecoord_ph, prod(size(vecoord_ph)), 1);
vecoord_th_vec = reshape(vecoord_th, prod(size(vecoord_th)), 1);
gm_mask_vec = reshape(gm_mask, prod(size(gm_mask)), 1);
wm_mask_vec = reshape(wm_mask, prod(size(wm_mask)), 1);
csf_mask_vec = reshape(csf_mask, prod(size(csf_mask)), 1);

% Extract positions within masks
N = length(img_fa_vec);
%gm
I = find(gm_mask_vec > 0);
vecoord_ph_vec_gm(1:length(I))=0;
vecoord_th_vec_gm(1:length(I))=0;
img_fa_vec_gm(1:length(I))=0;
for i=1:length(I)
    vecoord_ph_vec_gm(i) = vecoord_ph_vec(I(i));
    vecoord_th_vec_gm(i) = vecoord_th_vec(I(i));
    img_fa_vec_gm(i) = img_fa_vec(I(i));
end
%wm
J = find(wm_mask_vec > 0);
vecoord_ph_vec_wm(1:length(J))=0;
vecoord_th_vec_wm(1:length(J))=0;
img_fa_vec_wm(1:length(J))=0;
for i=1:length(J)
    vecoord_ph_vec_wm(i) = vecoord_ph_vec(J(i));
    vecoord_th_vec_wm(i) = vecoord_th_vec(J(i));
    img_fa_vec_wm(i) = img_fa_vec(J(i));
end
%csf
K = find(csf_mask_vec > 0);
vecoord_ph_vec_csf(1:length(K))=0;
vecoord_th_vec_csf(1:length(K))=0;
img_fa_vec_csf(1:length(K))=0;
for i=1:length(K)
    vecoord_ph_vec_csf(i) = vecoord_ph_vec(K(i));
    vecoord_th_vec_csf(i) = vecoord_th_vec(K(i));
    img_fa_vec_csf(i) = img_fa_vec(K(i));
end

% Calculates std, mean og cv for the fa-values within the masks
std_fa_gm = std(img_fa_vec_gm);
mean_fa_gm = mean(img_fa_vec_gm);
```

```
cv_fa_gm = std_fa_gm/mean_fa_gm;
std_fa_wm = std(img_fa_vec_wm);
mean_fa_wm = mean(img_fa_vec_wm);
cv_fa_wm = std_fa_wm/mean_fa_wm;
std_fa_csf = std(img_fa_vec_csf);
mean_fa_csf = mean(img_fa_vec_csf);
cv_fa_csf = std_fa_csf/mean_fa_csf;

% max and min for phi and theta
min_ph = min(vecoord_ph_vec_wm); max_ph = max(vecoord_ph_vec_wm);
min_th = min(vecoord_th_vec_wm); max_th = max(vecoord_th_vec_wm);

% rounded to integers
n_ph = round( (max_ph - min_ph)/DELTA_DEG);
n_th = round( (max_th - min_th)/DELTA_DEG );

% linspace(min_ph, max_ph, n_ph) generates a row vector of n_ph linearly
% equally spaced points between min_ph and max_ph.
ph = linspace(min_ph, max_ph, n_ph);
th = linspace(min_th, max_th, n_th);

% N = HISTC(X,EDGES), for vector X, counts the number of values in X
% that fall between the elements in the EDGES vector (which must contain
% monotonically non-decreasing values).  N is a LENGTH(EDGES) vector
% containing these counts.
% [N,BIN] = HISTC(X,EDGES,...) also returns an index matrix BIN.  If X is a
% vector, N(K) = SUM(BIN==K). BIN is zero for out of range values.
[nof_ph, bin_ph] = histc(vecoord_ph_vec_wm, ph);
[nof_th, bin_th] = histc(vecoord_th_vec_wm, th);

phdim = max(bin_ph);
thdim = max(bin_th);

fa_card(1:phdim,1:thdim)=0;
fa_mean(1:phdim,1:thdim)=0;
fa_std(1:phdim,1:thdim)=0;
fa_cv(1:phdim,1:thdim)=0;
for i_ph=1:phdim
    for i_th=1:thdim
        Kph = find(bin_ph == i_ph);
        Kth = find(bin_th == i_th);
        K = intersect(Kph, Kth);
        cardK = length(K);
        if cardK > 0
            tmp_fa(1:cardK)=0;
            for k=1:cardK
                tmp_fa(k) = img_fa_vec_wm(K(k));
                fa_bin{i_ph,i_th}.val{k} = tmp_fa(k);
            end
            fa_bin{i_ph,i_th}.idx = K;
            fa_card(i_ph,i_th) = cardK;
            fa_mean(i_ph,i_th) = mean(tmp_fa);
            fa_std(i_ph,i_th) = std(tmp_fa);
            fa_cv(i_ph,i_th) = std(tmp_fa)/mean(tmp_fa);
        end
    end
end

% Plotting
mx=1600; %mx=max(max(fa_card));
mn=0; %mn=min(min(fa_card));
fg1=figure(1);
```

```
set(fg1, 'Position', [71 91 814 578]);
imagesc(fa_card, [mn mx]), colormap(gray), axis image, colorbar('v');
title(sprintf('card(FA) as a function of
    min_ph, max_ph, phdim, min_th, max_th, thdim));

mx=0.60; %mx=max(max(fa_mean));
mn=0; %mn=min(min(fa_mean));
fg2=figure(2);
set(fg2, 'Position', [71 91 814 578]);
imagesc(fa_mean, [mn mx]), colormap(gray), axis image, colorbar('v');
title(sprintf('mean(FA) as a function of
    min_ph, max_ph, phdim, min_th, max_th, thdim));

mx=0.22; %mx=max(max(fa_std));
mn=0; %mn=min(min(fa_std));
fg3=figure(3);
set(fg3, 'Position', [71 91 814 578]);
imagesc(fa_std, [mn mx]), colormap(gray), axis image, colorbar('v');
title(sprintf('std(FA) as a function of
    min_ph, max_ph, phdim, min_th, max_th, thdim));

mnx=-200;mxx=200;mny=-100;mxy=100;mnz=0;mxz=0.25;
fg4=figure(4);
set(fg4, 'Position', [71 91 814 578]);
surfc(th,ph,fa_std), colormap(gray);
axis([mnx mxx mny mxy mnz mxz])
zlabel('std(FA)', 'FontSize', 14)
xlabel('\phi', 'FontSize', 18)
ylabel('\theta', 'FontSize', 18)
title(sprintf('Subject %s: %d directions, nex=%d', ...
    subj_id, nof_diff_dirs, nex), 'FontSize', 14)

mx=0.62; %mx=max(max(fa_cv));
mn=0; %mn=min(min(fa_cv));
fg5=figure(5);
set(fg5, 'Position', [71 91 814 578]);
imagesc(fa_cv, [mn mx]), colormap(gray), axis image, colorbar('v');
title(sprintf('cv(FA) as a function of
    min_ph, max_ph, phdim, min_th, max_th, thdim));
```

B.10 dti-demo-all-slice.m

```
function r = dti_demo_all_slices_20041116(study,slice_no)
% dti_demo_all_slices_20041116.m
% Ex:
% r = dti_demo_all_slices_20041116('OH25dir2NEX', 12);
% Arvid Lundervold, NOV-2004


close all

%BASE_DIR = 'g:/Ketil/m-files/ketils_workspaces/20040214';
BASE_DIR = 'g:/Ketil/m-files/ketils_workspaces/20040604';

% load /mnt/cdrom/SA6dir8NEX.mat
% load d:/OH25dir2NEX.mat
cmd = sprintf('load %s/%s.mat', BASE_DIR, study);  eval(cmd);

% ==>
%   D                           5-D       3     3   196   160    24
```

```
%   V                         256x256x24
%   dti                         4-D       7   196   160    24
%   dti_foer_nedskalering       4-D       7   256   256    24
%   img_fa                    196x160x24
%   img_linear                196x160x24
%   linmask                   196x160x24   logical array
%   mask                      196x160x24   double array
%   vecoord_ph                196x160x24   double array
%   vecoord_th                196x160x24   double array
%   whitemask                 196x160x24   logical array
%   wm_mask                   196x160x24   logical array


DISP = 1;
SLICE = slice_no;

[D_nr, D_nc, nr, nc, ns] = size(D);
[nd, nr, nc, ns] = size(dti);
nd=nd-1;


L_THR = 100; % 300;  % By inspection of histograms ...
D_slice = reshape(dti(2:nd+1,:,:,SLICE), nd, nr, nc);
[M] = lcl_make_brain_mask(D_slice, L_THR, DISP);

D_tensor = reshape(D(:,:,:,:,SLICE), D_nr, D_nc, nr, nc);
[EIGval, EIGvec] = lcl_compute_eigensystem(D_tensor, nr, nc);

txt = sprintf('%s - slice %d', study, slice_no);
[FA] = lcl_display_fractional_anisotropy(EIGval, nr, nc, M, txt, DISP);

[RGB] = lcl_display_diff_rgb(EIGval, EIGvec, FA, nr, nc, M, txt, DISP);

r.SLICE = SLICE;
r.M = M;
r.EIGval = EIGval;
r.EIGvec = EIGvec;
r.FA = FA;
r.RGB = RGB;

%=========================================================================

% Local functions

%-------------------------------------------------------------------------

function [EIGval, EIGvec] = lcl_compute_eigensystem(D_tensor, nr, nc)

x=zeros(9,nr*nc);
% for k=1:nd-1
%     G_tilde_k = lcl_dual_tensor_basis_element(k, nd-1, diff_enc_dirs_6);
%     x = x + ( ones(9,1)*reshape(beta_k(k,:),1,nr*nc) ) .* (
%     reshape(G_tilde_k, 9, 1)*ones(1,nr*nc) );
% end


k=0;
for i=1:3
    for j=1:3
        k=k+1;
        x(k,:) = reshape(D_tensor(i,j,:,:), 1, nr*nc);
    end
```

```
end


D = x;
EIGval = zeros(3,nr*nc);
EIGvec = zeros(3,3,nr*nc);  % zeros(9,nr*nc);
for i=1:nr*nc;
    Di = reshape(D(:,i), 3,3);
    [eigenvec, eigenval] = eig(Di);  % eigs(Di) is much slower
    [val, I] = sort(-diag(eigenval));
    for j=1:3;
      vec(1:3,j) = eigenvec(1:3,I(j));
    end
    EIGval(:,i) = -val;
    EIGvec(:,:,i) = reshape(vec,3,3,1);
end

return

%---------------------------------------------------------------------

function [FA] = lcl_display_fractional_anisotropy(EIGval, nr, nc, M, txt, DISP)


fno = 120;

WIENER = 0;
c = 1/sqrt(2);

FA_vec=zeros(1,nr*nc);
epsi = 1e-100;
for i=1:nr*nc;
    l1 = EIGval(1,i);
    l2 = EIGval(2,i);
    l3 = EIGval(3,i);
    numer = sqrt((l1-l2)*(l1-l2) + (l2-l3)*(l2-l3) + (l1-l3)*(l1-l3));
    denumer = max(sqrt(l1*l1+l2*l2+l3*l3), epsi);
    %denumer = sqrt(l1*l1+l2*l2+l3*l3);
    FA_vec(i) = c*numer/denumer; % min(c*numer/denumer, 1.0);
    %if FA_vec(i) > 1.0001
    %    FA_vec(i) = NaN;
    %end
end

FA = reshape(FA_vec,nr,nc);

FA_M = FA .* M;

if DISP == 1
    mn = min(min(FA_M)); mx = max(max(FA_M));
    figure(fno)
    set(gcf, 'Position', [485 265 840 687]);
    if WIENER == 1
        [FA_wiener,NOISE] = wiener2(FA_M,[3 3]);
        imagesc(FA_wiener, [mn mx]), axis image, axis off, colormap(gray);
    else
        imagesc(FA_M, [mn mx]), axis image, axis off, colormap(gray);
    end
    txt2 = sprintf('%s  min=%.2f, max=%.2f', txt, mn, mx);
    %title(txt2, 'FontSize', 14)
    pause(0.05)
end % DISP
```

```
return

%--------------------------------------------------------------------------

function [RGB] = lcl_display_diff_rgb(EIGval, EIGvec, FA, nr, nc, M, txt, DISP)

fno = 130;

WIENER = 0;
FA_vec = reshape(FA, 1, nr*nc);
RGB=zeros(nr,nc,3);
lambda1 = zeros(1,nr*nc);
v1x = zeros(1,nr*nc);
v1y = zeros(1,nr*nc);
v1z = zeros(1,nr*nc);
for i=1:nr*nc;
    lambda1(i) = EIGval(1,i);
    x = EIGvec(1,1,i); % x-component of eigenvector corresponding to largest eigenvalue
    y = EIGvec(2,1,i); % y-comp.
    z = EIGvec(3,1,i); % z-comp.
    v = [x, y, z]';
    vn = v / sqrt(v'*v);
    v1x(i) = abs(FA_vec(i)*vn(1));
    v1y(i) = abs(FA_vec(i)*vn(2));
    v1z(i) = abs(FA_vec(i)*vn(3));
end
V1x = reshape(v1x,nr,nc);
V1y = reshape(v1y,nr,nc);
V1z = reshape(v1z,nr,nc);

if WIENER == 1
    [R, noise_r] = wiener2(V1x,3,3); % ./ max(max(V1x));
    [G, noise_g] = wiener2(V1y,3,3); %  ./ max(max(V1y));
    [B, noise_b] = wiener2(V1z,3,3); % ./ max(max(V1z));
else
    R = V1x; % ./ max(max(V1x));
    G = V1y; %  ./ max(max(V1y));
    B = V1z; % ./ max(max(V1z));
end

R_M = R .* M;
G_M = G .* M;
B_M = B .* M;

RGB(:,:,1) = R ./ max(max(R));
RGB(:,:,2) = G ./ max(max(G));
RGB(:,:,3) = B ./ max(max(B));

RGB_M(:,:,1) = R_M ./ max(max(R));
RGB_M(:,:,2) = G_M ./ max(max(G));
RGB_M(:,:,3) = B_M ./ max(max(B));

if DISP == 1
    figure(fno)
    imshow(RGB_M);
    set(gcf, 'Position', [485 265 840 687]);
    txt2 = sprintf('%s  R = FA*|v1_x|, G = FA*|v1_y|, B = FA*|v1_z|', txt);
    %title(txt2, 'FontSize', 14)
    pause(0.05)
end %DISP
```

```
return

%-----------------------------------------------------------------------

function [M] = lcl_make_brain_mask(D_slice, thr, DISP)

HSIZE = 5;
SIGMA = 3.0;
L_THRES = thr;

[nd, nr, nc] = size(D_slice);
im =zeros(nr,nc);
for d=1:nd
    im = im + reshape(D_slice(d,:,:), nr, nc);
end
im = im/nd;

H = fspecial('gaussian', HSIZE, SIGMA);
im1 = imfilter(im, H);


% 2-D order statistics filtering
%im2 = ordfilt2(im1, 1, ones(3,3));
im2 = im1;
mn = min(min(im2)); mx = max(max(im2));
M = roicolor(im2, L_THRES, mx);

% Outlined original image

im3 = bwperim(M);
im4 = im;
im4(im3) = max(max(im2)); % 255;

if DISP == 1
    fno = 101;
    figure(fno)
    set(gcf, 'Position', [485 265 840 687]);
    subplot(1,2,1)
    imagesc(M, [0 1]), axis image, axis off, colormap(gray);
    txt = sprintf('ROI (for calculation of DTI)');
    %title(txt, 'FontSize', 12)
    subplot(1,2,2)
    imagesc(im4, [mn mx]), axis image, axis off, colormap(gray);
    txt = sprintf('Outer contour of the brain:  min=%.2f, max=%.2f', mn, mx);
    %title(txt, 'FontSize', 12)
end % DISP

return
```

B.11 fsl-dtianal-34slices.sh

```
#!/bin/sh

# fsl_dtianal_34slices.sh


FSLDIR=/usr/local/fsl
. ${FSLDIR}/etc/fslconf/fsl.sh
PATH=${FSLDIR}/bin:${PATH}
export FSLDIR PATH
```

```
CUR_DIR=‘pwd‘

DATA_DIR=/home/mrdata/al_tracking_12052005/Analyze/
echo DATA_DIR=$DATA_DIR

cd $DATA_DIR

# Merges the DTI-data from several 3D Analyze images too a 4D dataset
avwmerge -t data_noecc.nii rb00.hdr b01.hdr b02.hdr b03.hdr b04.hdr b05.hdr
b06.hdr b07.hdr b08.hdr b09.hdr b10.hdr b11.hdr b12.hdr b13.hdr b14.hdr
b15.hdr b16.hdr b17.hdr b18.hdr b19.hdr b20.hdr b21.hdr b22.hdr b23.hdr
b24.hdr b25.hdr

# Eddy current correction on the dataset
eddy_correct data_noecc.nii data.nii 0

# Makes a non-DTI image by merging of the b0 data
avwmerge -t nodif_noecc.nii rb00.hdr

# Eddy current correction on the dataset
eddy_correct nodif_noecc.nii nodif.nii 0

# Brain extraction tool, deletes non-brain tissue from an image of the
# whole brain
bet2 nodif nodif_brain -m -v

# DTIFit fits a diffusion tensor model at each voxel and does eigen-
# decompsition and calcultaes among other tings FA
dtifit --data=data --out=dti --mask=nodif_brain_mask --bvecs=bvecs
--bvals=bvals --verbose

# Bayesian Estimation of Diffusion Parameters Obtained using Sampling
# Techniques. Bedpost runs Markov Chain Monte Carlo sampling to build
# up distributions on diffusion parameters at each voxel. It creates
# all the files necessary for running probabilistic tractography
bedpost .

cd $CUR_DIR
echo CUR_DIR=$CUR_DIR
```

To learn more about the brain extraction tool used here see [56].

C

The Diffusion Equations

C.1 Basic Hypothesis and Mathematical Theory

Fick [57] recognized the obvious analogy between heat conduction and isotropic diffusion. Transfer of heat is caused by random molecular motions as well. He put diffusion on a quantitative basis by adopting the mathematical equation of heat conduction derived earlier by Fourier [58]. The mathematical theory of diffusion in isotropic substances is therefore based on the hypothesis that the rate of transfer of diffusing substance through a unit area of a section is proportional to the concentration gradient measured normal to the section, i.e.

$$F = -D\partial C/\partial x \tag{C.1}$$

where F is the rate of transfer per unit area of section, C the concentration of diffusing substance, x the space coordinate measured normal to the section, and D is called the diffusion coefficient. With diffusion taking place in dilute solutions, D can admissibly be taken as constant, and with diffusion taking place in high polymers, it depends markedly on concentration. If F, the amount of diffusing substance, and C the concentration are expressed in terms of the same unit of quantity, then it is clear from equation (C.1) that D is independent of this unit and has dimensions $length^2 time^{-1}$. The negative sign in equation (C.1) arises because diffusion occurs in the direction opposite to that of increasing concentration.

It is important to accentuate that equation (C.1) only yields for an isotropic medium i.e. a medium whose structure and diffusion properties in the neighborhood of any point are the same relative to all directions. Because of this symmetry, the flow of diffusing substance at any point is along the normal to the surface of constant concentration through the point. As shown in C.3 this is seldom true in an anisotropic medium for which the diffusion properties depend on the direction in which they are measured.

C.2 Differential Equation of Diffusion

The fundamental differential equation of diffusion in an isotropic medium is derived from equation (C.1) as described below:

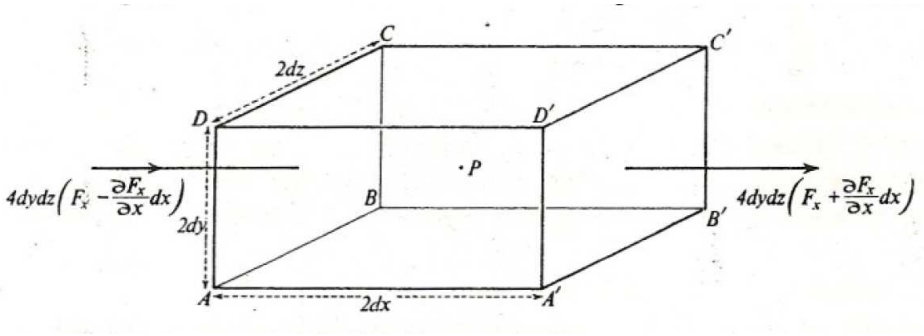

Figure C.1: Element of volume

Imagine an element of volume in the form of a rectangular parallelepiped whose sides are parallel to the axes of coordinates and are of lengths $2dx, 2dy$ and $2dz$. Let the center of the element be at $P(x,y,z)$, where the concentration of diffusing substance is C. Let $ABCD$ and $A'B'C'D'$ be the faces perpendicular to the axis of x as in Figure C.1. Then the rate at which diffusing substance enters the element through the face $ABCD$ in the plane $x-dx$ is given by

$$4dydz\left(F_x-\frac{\partial F_x}{\partial x}dx\right) \tag{C.2}$$

where F_x is the rate of transfer through unit area of the corresponding plane through P. Similarly the rate of loss of diffusing substance through the face $A'B'C'D'$ is given by

$$4dydz\left(F_x+\frac{\partial F_x}{\partial x}dx\right) \tag{C.3}$$

The contribution to the rate of increase of diffusing substance in the element from these two faces is thus equal to

$$-8dxdydz\frac{\partial F_x}{\partial x} \tag{C.4}$$

Similarly from the other faces we obtain

$$-8dxdydz\frac{\partial F_y}{\partial y} \qquad \text{and} \qquad -8dxdydz\frac{\partial F_z}{\partial z} \tag{C.5}$$

But the rate at which the amount of diffusing substance in the element increases is also given by

$$-8dxdydz\frac{\partial C}{\partial t} \tag{C.6}$$

and hence we have immediately

$$\frac{\partial C}{\partial t}+\frac{\partial F_x}{\partial x}+\frac{\partial F_y}{\partial y}+\frac{\partial F_z}{\partial z}=0 \tag{C.7}$$

If the diffusion coefficient is constant, F_x, F_y, F_z are given by equation (C.1), and (C.7) becomes

$$\frac{\partial C}{\partial t} = D\left(\frac{\partial^2 C}{\partial x^2} + \frac{\partial^2 C}{\partial y^2} + \frac{\partial^2 C}{\partial z^2}\right) \tag{C.8}$$

reducing simply to

$$\frac{\partial C}{\partial t} = D\frac{\partial^2 C}{\partial x^2} \tag{C.9}$$

if diffusion is one–dimensional, i.e. if there is a gradient of concentration only along the x-axis. Expression (C.1) and (C.9) are usually referred to as Fick's first and second laws of diffusion, since they were first formulated by Fick [57] by direct analogy with the equations of heat conduction.

In many systems, e.g. the inter diffusion of metals or the diffusion of organic vapors in high polymer substances, D depends on the concentration of diffusing substance, C. In this case, and also when the medium is not homogeneous so that D varies from point to point, equation (C.7) becomes

$$\frac{\partial C}{\partial t} = \frac{\partial}{\partial x}\left(D\frac{\partial C}{\partial x}\right) + \frac{\partial}{\partial y}\left(D\frac{\partial C}{\partial y}\right) + \frac{\partial}{\partial z}\left(D\frac{\partial C}{\partial z}\right) \tag{C.10}$$

where D may be a function of $x, y, z,$ and C.

If D depends on time during which diffusion has been taking place but not on any of the other variables, i.e.

$$D = f(t), \tag{C.11}$$

then on introducing a new time-scale T such that

$$dT = f(t)dt \tag{C.12}$$

the diffusion equation becomes

$$\frac{\partial C}{\partial T} = \frac{\partial^2 C}{\partial x^2} + \frac{\partial^2 C}{\partial y^2} + \frac{\partial^2 C}{\partial z^2} \tag{C.13}$$

which is the same as equation (C.8) for a constant diffusion coefficient equal to unity.

C.2.1 Diffusion in a Cylinder and a Sphere

Other forms of the above equations follow by transformation of coordinates, or by considering elements of volume of different shape. Thus by putting

$$\begin{aligned} x &= r\cos\theta, \\ y &= r\sin\theta, \end{aligned} \tag{C.14}$$

or by considering an element of volume of a cylinder of sides $dr, rd\theta, dz$, we obtain the equation for diffusion in a cylinder,

$$\frac{\partial C}{\partial t} = \frac{1}{r}\left[\frac{\partial}{\partial r}\left(rD\frac{\partial C}{\partial r}\right) + \frac{\partial}{\partial \theta}\left(\frac{D}{r}\frac{\partial C}{\partial \theta}\right) + \frac{\partial}{\partial z}\left(rD\frac{\partial C}{\partial z}\right)\right] \tag{C.15}$$

in terms of the cylindrical coordinates r, θ, z. The corresponding equation for a sphere in terms of spherical polar coordinates r, θ, ϕ is obtained by writing

$$\begin{aligned} x &= r\sin\theta\cos\phi \\ y &= r\sin\theta\sin\phi \\ z &= r\cos\theta \end{aligned} \tag{C.16}$$

or by considering an element of volume of a sphere of sides $dr, rd\theta, r\sin\theta d\phi$. It is

$$\frac{\partial C}{\partial t} = \frac{1}{r^2}\left[\frac{\partial}{\partial r}\left(Dr^2\frac{\partial C}{\partial r}\right) + \frac{1}{\sin\theta}\frac{\partial}{\partial\theta}\left(D\sin\theta\frac{\partial C}{\partial\theta}\right) + \frac{D}{\sin^2\theta}\frac{\partial^2 C}{\partial\phi^2}\right] \tag{C.17}$$

The equations (C.15) (C.17) can be expressed in terms of the nomenclature of vector analysis as

$$\frac{\partial C}{\partial t} = div\,(D\ grad\ C) \tag{C.18}$$

C.3 Anisotropic Media

Anisotropic media have different diffusion properties in different directions. Some common examples are crystals, textile fibers, and polymer films in which the molecules have a preferential direction of orientation. For such a media it is not always true, as was stated in C.1 for isotropic media, that the direction of flow of diffusing substance at any point is normal to the surface of constant concentration through the point. This means that equation (C.1) must be replaced in general by the assumptions

$$\begin{aligned} -F_x &= D_{11}\frac{\partial C}{\partial x} + D_{12}\frac{\partial C}{\partial y} + D_{13}\frac{\partial C}{\partial z} \\ -F_y &= D_{21}\frac{\partial C}{\partial x} + D_{22}\frac{\partial C}{\partial y} + D_{23}\frac{\partial C}{\partial z} \\ -F_z &= D_{31}\frac{\partial C}{\partial x} + D_{32}\frac{\partial C}{\partial y} + D_{33}\frac{\partial C}{\partial z} \end{aligned} \tag{C.19}$$

so that F_x, for example, depends not only on $\partial C/\partial x$ but also on $\partial C/\partial y$ and $\partial C/\partial z$. The D's have the significance that $D_{13}\partial C/\partial z$, for example, is the contribution to the rate of transfer in the x–direction due to the component of concentration gradient i the z–direction. Substituting from equation (C.19) for the F's in equation (C.7) we obtain

$$\begin{aligned} \frac{\partial C}{\partial t} = D_{11}\frac{\partial^2 C}{\partial x^2} + D_{22}\frac{\partial^2 C}{\partial y^2} + D_{33}\frac{\partial^2 C}{\partial z^2} + (D_{23}+D_{32})\frac{\partial^2 C}{\partial y\partial z} \\ + (D_{31}+D_{13})\frac{\partial^2 C}{\partial z\partial x} + (D_{12}+D_{21})\frac{\partial^2 C}{\partial x\partial y} \end{aligned} \tag{C.20}$$

if the D's are taken as constant. The extension to non-constant D's is obvious from equation (C.10). A transformation to rectangular coordinates ξ, η, ζ can be found which reduces equation (C.20) to

$$\frac{\partial C}{\partial t} = D_1\frac{\partial^2 C}{\partial\xi^2} + D_2\frac{\partial^2 C}{\partial\eta^2} + D_3\frac{\partial^2 C}{\partial\zeta^2} \tag{C.21}$$

This is the same transformation as that by which the ellipsoid

$$D_{11}x^2 + D_{22}y^2 + D_{33}z^2 + (D_{23} + D_{32})yz + (D_{31} + D_{13})zx + (D_{12} + D_{21})xy = \text{constant} \quad \text{(C.22)}$$

is reduced to

$$D_1\xi^2 + D_2\eta^2 + D_3\zeta^2 = \text{constant} \quad \text{(C.23)}$$

The new axes may be called the principal axes of diffusion and D_1, D_2, D_3 the principal diffusion coefficients. If we make the further transformation

$$\xi_1 = \xi\sqrt{(D/D_1)}, \qquad \eta_1 = \eta\sqrt{(D/D_2)}, \qquad \zeta_1 = \zeta\sqrt{(D/D_3)}, \quad \text{(C.24)}$$

where D may be chosen arbitrarily, equation (C.21) becomes

$$\frac{\partial C}{\partial t} = D\left(\frac{\partial^2 C}{\partial \xi_1^2} + \frac{\partial^2 C}{\partial \eta_1^2} + \frac{\partial^2 C}{\partial \zeta_1^2}\right). \quad \text{(C.25)}$$

This has the same form as equation (C.8) for isotropic media, and hence certain problems in anisotropic media can be reduced to corresponding problems in anisotropic media. Whether or not this can be done in a given case depends on the boundary conditions. Thus it is possible when the medium is infinite, or when it is bounded by planes perpendicular to the principal axes of diffusion so that the boundary conditions are of the familiar form C = constant, $\xi = 0$, $\xi = l$, $t > 0$, for example, and similarly for η and ζ. The problem of diffusion into an anisotropic cylinder which has its axis along ξ and is bounded by planes perpendicular to ξ reduces to the corresponding problem in an isotropic cylinder provided $D_2 = D_3$.

Certain properties deduced by Carslaw and Jaeger [59] page 29 indicate the physical significance of the ellipsoid and also of the principal axes of diffusion. Thus it can be shown that the square of the radius vector of the ellipsoid in any direction is inversely proportional to the diffusion coefficient normal to the surfaces of constant concentration at points where their normals are in that direction. Hence the diffusion coefficient, D_n, at right angles to surfaces whose normals have direction cosines l, m, n relative to the principal axes of diffusion is given by

$$D_n = l^2D_1 + m^2D_2 + n^2D_3 \quad \text{(C.26)}$$

Carslaw and Jaeger further show that if there is symmetry about the planes $\xi = 0$ and $\eta = 0$, then the general relationships (C.19) for the F's reduce to

$$-F_\xi = D_1\partial C/\partial\xi, \qquad -F_\eta = D_2\partial C/\partial\eta, \qquad -F_\zeta = D_1\partial C/\partial\zeta \quad \text{(C.27)}$$

This simplification also occurs for other types of crystallographic symmetry. It means that the flow through a surface perpendicular to a principal axis of diffusion is proportional simply to the concentration gradient normal to the surface as is the case for isotropic media.

C.3.1 Significance of Measurements in Anisotropic Media

Since in the majority of experiments designed to measure a diffusion coefficient the flow is arranged to be one-dimensional one–dimensional one—dimensional, it is worth while to see how such measurements are affected by anisotropy. If the diffusion is one-dimensional in the sense that a concentration gradient exists only along the direction of x, it is clear from equation (C.20), since

both C and $\partial C/\partial x$ are everywhere independent of y and z, that the diffusion is governed by the simple equation

$$\frac{\partial C}{\partial t} = D_{11}\frac{\partial^2 C}{\partial x^2} \tag{C.28}$$

and D_{11} is the diffusion coefficient measured. If the direction of diffusion is chosen to be that of a principal axis, then D_{11} is equal to one or the other of the principal diffusion coefficients D_1, D_2 or D_3. Otherwise the coefficient $D_{11} = D_n$, related to D_1, D_2, D_3, by equation (C.26) is measured. This would be measured, for example, by an observation of the rate of flow through a plane sheet of a crystal cut so that its normal has direction cosines (l, m, n) relative to the principal axes of diffusion of the crystal. Similar remarks apply to a high polymer sheet in which there is both uni-planar and uni-directional orientation, i.e. the molecules are arranged with their long axes lying mainly parallel to the plane of the sheet and all parallel to one direction in that plane. The principal axes of diffusion of such a sheet will be normal to the plane sheet, and along and perpendicular to the preferred direction of orientation in that plane. Even if a concentration gradient exists in one direction only, it is clear from equations (C.19) and (C.25) that the diffusion flow is not along this direction unless it coincides with a principal axis of diffusion.

D

Diffusion gradients and the b-value

In DTI there is a need for diffusion gradients to encode diffusion. Several pulse sequences has incorporated such gradients. Former the Stejskal-Tanner pulse scheme [22], implemented in a spin echo pulse sequence as depicted in Figure D.1, has been the most common type of diffusion gradient design. Today the readout gradient is often replaced by an EPI (Echo Planar Imaging) readout train.

In the Stejskal-Tanner pulse scheme the first diffusion gradient is applied between the excitation pulse and the 180° refocusing pulse. The second diffusion gradient is applied between the 180° refocusing pulse and the echo.

In this way the diffusion gradients introduce phase shifts of the spins as a function of position. They can be applied in the *x*,*y* or *z* direction or a linear combination of these. If the gradients are applied for example in the *z* direction, the phase shift due to the first gradient is

$$\varphi_1 = \gamma \int_0^{\delta} G \cdot z dt = \gamma \cdot G \cdot \delta \cdot z_1 \tag{D.1}$$

where z_1 is the position of spin or molecule which is assumed to be still during the time δ when the diffusion gradient is applied. The assumption is only valid as long as $\delta \ll \Delta$, which means that the diffusion process must be negligible during the application of the diffusion sensitizing gradients. Because the gradient amplitude in human MR scanners is limited to $20-50 mT/m$ a fairly large δ is needed to obtain the desired diffusion weighting, so the above-mentioned assumption is seldom met. On the other hand, this assumption serves to provide a basic understanding of how the *b*-value is derived.

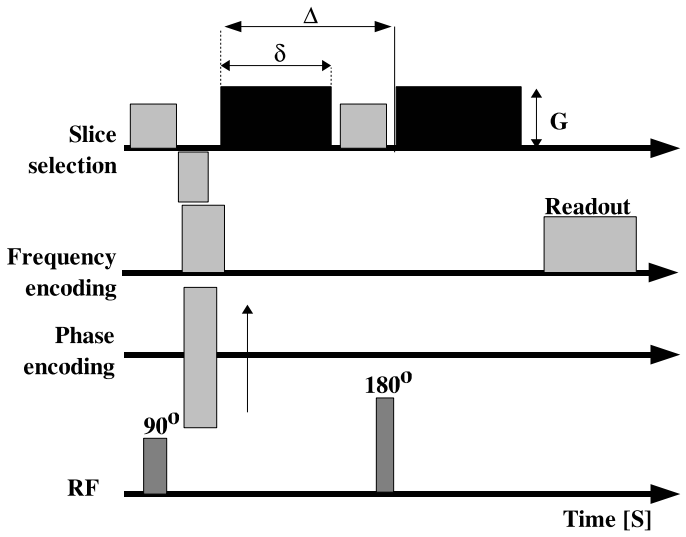

Figure D.1: Stejskal-Tanner diffusion gradients in a spin echo sequence. The duration (δ), amplitude (G) and time shift between the gradients (Δ) affects the amount of diffusion weighting – e.g. the "b" value. It is important to note that the diffusion gradient can be applied on any of the three imaging axes or on a combination of them. Courtesy of Skare [24].

After the first diffusion gradient has been switched off, the 180° refocusing pulse is applied. The refocusing pulse changes the sign of the phase ($\varphi_1 \Rightarrow -\varphi_1$). The second diffusion gradient will then produce a phase shift of

$$\varphi_2 = \gamma \int_{\Delta}^{\Delta+\delta} G \cdot z dt = \gamma \cdot G \cdot \delta \cdot z_2 \tag{D.2}$$

where z_2 is the position of the spin during the application of the second diffusion gradient. If the spin is "static", i.e. a spin that does not move between the excitation pulse and the echo pulse, $z_1 = z_2$ and the net phase of the two diffusion gradients is

$$\varphi = \varphi_1 + \varphi_2 = \gamma \cdot G \cdot \delta(-z_1 + z_2) = 0 \tag{D.3}$$

For spins that diffuse a certain amount during the time interval between the application of the diffusion gradients, the phase will be non-zero. Because diffusion is a random process it is necessary to inspect the entire population of spins in each voxel. Depending on the displacement path along the diffusion gradient, each individual spin will get a certain net phase, φ_j. The resulting net magnetization M for a voxel is the vector sum of the magnetic moments μ of each of the N spins within that voxel

$$M = \mu \left| \sum_{j=1}^{N} e^{i \cdot \varphi_j} \right| \tag{D.4}$$

This is illustrated in Figure D.2. In a hypothetical situation with no diffusion at all $\varphi_j = k$ which

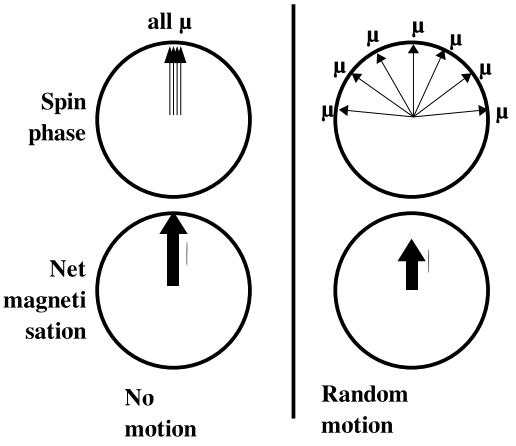

Figure D.2: If the water molecules have diffused during the application of the diffusion sensitizing gradients the spins are dephasing randomly in the transverse plane. The vector sum of all magnetic moments now results in a lower net magnetization (M). This is in contrast to the situation with no diffusion where the net magnetization is unaffected. Courtesy of Skare [24].

is a constant and the net magnetization would be maximal

$$M = \mu \left| \sum_{j=1}^{N} e^{i \cdot k} \right| = \mu \cdot N \tag{D.5}$$

Let $P(z_2|z_1,\Delta)dz_2$ be the conditional probability of finding a spin, originating at z_1 at $t = 0$, between z_2 and $z_2 + dz_2$ at $t = \Delta$. Then, by combining Eq. (D.3), (D.4) and (D.5) we get

$$M = M_0 \int e^{i \cdot \gamma G \delta (z_2 - z_1)} P(z_2|z_1,\Delta) dz_2 \tag{D.6}$$

where $P(z_2|z_1,\Delta)$ for this 1D case is given by

$$P(\mathbf{r},t) = \frac{1}{\sqrt{4\pi D\Delta}} \cdot e^{-(z_2 - z_1)^2 / 4D\Delta} \tag{D.7}$$

Combining Eq. (D.6) and (D.7) gives the following

$$\frac{M}{M_0} = e^{-(\gamma \cdot \delta \cdot G)^2 \cdot \Delta \cdot D} = e^{-b \cdot D} \tag{D.8}$$

Equation (D.8) shows the degree of signal attenuation due to diffusion as a function of gradient amplitude, duration and time interval between the two diffusion gradients. The expression for the b value is here $b = \left(\gamma \dot{\delta} \cdot G\right)^2 \Delta$, which again is only valid if $\delta \ll \Delta$. In the same way as TE and TR are parameters that controls the amount of T_2-weighting and T_1-weighting respectively, does the b-value control the diffusion weighting in an image.

A general expression for the b-value is

$$\frac{M}{M_0} = e^{-\left[\gamma^2 \int_0^{TE} \left(\int_0^t g(t')dt'\right)^2 dt\right] \cdot D} = e^{-b \cdot D} \tag{D.9}$$

where TE is the echo time. This expression does not assume that $\delta \ll \Delta$ and the diffusion gradients may be more than two and can be combined without invalidating the expression. For the Stejskal-Tanner diffusion gradient scheme Fig. D.1, the diffusion gradient function $g(t)$ is

$$g(t) = \begin{cases} G & ,0 \leq t < \delta \\ 0 & ,\delta \leq t < \Delta \\ -G & ,\Delta \leq t < \Delta + \delta \end{cases} \tag{D.10}$$

Putting (D.10) into (D.9) will give us

$$b = \gamma^2 \int_0^{\Delta+\delta} \left(\int_0^t g(t')dt' \right)^2 dt = \ldots = (\gamma \cdot G \cdot \delta)^2 \cdot \left(\Delta - \frac{\delta}{3} \right) \tag{D.11}$$

And so we have arrived at the familiar expression for the b value. If we now let $\delta \ll \Delta$, Eq. (D.11) becomes identical to the b factor derived in Eq. (D.8).

The optimal value for b: Due to noise the choice of b value becomes important. If the b value is chosen to low, it will result in a diffusion induced signal attenuation that is comparable to the variance of the diffusion weighted data. The implication is that the calculated diffusion coefficient will be estimated with too low precision. In the reverse example, if the b value is chosen to high, the signal attenuation and the signal may drop below the system noise level.This results in an underestimation for high values for the calculated diffusion because the system noise is higher than the true diffusion weighted signal.

We have chosen to use b equally to $1000 s/mm^2$, because that is most often reported in literature, see for example [27], [60], [34], [25] and [24].

References

[1] P.J. Basser D.C. Alexander, C. Pierpaoli and J.C. Gee. Spatial transformations of diffusion tensor magnetic resonance images. *IEEE Transactions on Medical Imaging*, 20(11):1131–1139, 2001.

[2] Corey Ann Kemper. Incorporation of diffusion tensor mri in non-rigid registration for image-guided neurosurgery. Master's thesis, Department of Electrical Engineering and Computer Science, MIT, 2003.

[3] Christian Beaulieu. The basis of anisotropic water diffusion in the nervous system–a technical review. *NMR IN BIOMEDICINE*, 15:435–455, 2002.

[4] *The Fine Structure of the Nervous System: Neurons and their Supporting Cells*. Oxford University Press, 3^{rd} edition, 1991.

[5] Allen PS. Beaulieu C. Determinants of anisotropic water diffusion in nerves. *Magetic Resonance in Medicine*, 31:394–400, 1994.

[6] Duncan ID Lauterbur PC Gulani V, Webb AG. Apparent diffusion tensor measurements in myelin-deficit rat spinal cords. *Magnetic Resonance in Medicine*, 45:191–195, 2001.

[7] Peled S Zientara GP Barnes PD Jolesz FA Volpe JJ Huppi PS, Maier SE. Microstructural development of human newborn cerebral white matter assessed in vivo by diffusion tensor magnetic resonance imaging. *Pediatr. Res.*, 44:584–590, 1998.

[8] McKinstry RC Schefft GL Snyder AZ Almli CR Akbudak E Aronovitz JA Miller JP Lee BC Conturo TE Neil JJ, Shiran SI. Normal brain in human newborns: Apparent diffusion coefficient and diffusion anisotropy measured by using diffusion tensor mr imaging. *Radiology*, 209:57–66, 1998.

[9] Dettbarn WD Darind De Lorenzo AJ, Brzin M. Fine structure and organization of nerve fibres and giant axon in homarus americanus. *J. Ultrastruct. Res.*, 24:367–384, 1968.

[10] Takahashi M Maeda M Ikenake K Sakurai K Sakai N Kagawa T Fritz-Zieroth B Nagai T et al. Ono J, Harada K. Differentiation between dysmyelination and demyelination using magnetic resonance diffusional anisotropy. *Brain Res.*, 671:141–148, 1995.

[11] Barkovich AJ Prayer L Kucharczyk J Moseley M Arieff A. Prayer D, Roberts T. Diffusion-weighted mri of myelination in the rat brain following treatment with gonadal hormones. *Neuroradiology*, 39:320–325, 1997.

[12] Morita Y Navon G Seo Y, Shinar H. Anisotropic and restricted diffusion of water in the sciatic nerve: A (2)h double-quantum-filtered nmr study. *Magnetic Resonance in Medicine*, 42:461–466, 1999.

[13] Barkovich AJ Prayer LM Moseley ME Kucharczyk J Wimberger DM, Roberts TP. Identification of "premyelination" by diffusion-weighted mri. *J. Comput. Assist. Tomogr.*, 19:28–33, 1995.

[14] Peter J. Basser Alan Barnett Giovanni Di Chiro Carlo Pierpaoli, Peter Jazzard. Diffusion tensor mr imaging of the human brain. *Radiology*, 201:637–648, 1996.

[15] Takeda K Tagami T Nakagawa T Tamagawa Y Ishii Y Tsukamoto T Sakuma H, Nomura Y. Adult and neonatal human brain: Diffusional anisotropy and myelination with diffusionweighted mr imaging. *Radiology*, 180:229–233, 1991.

[16] Allen PS. Beaulieu C. Water diffusion in the giant axon of the squid: implications for diffusion-weighted mri of the nervous system. *Magnetic Resonance in Medicine*, 32:579–583, 1994.

[17] Hawkins J Trudeau JD, Dixon WT. The effect of inhomogeneous sample susceptibility on measured diffusion anisotropy usin nmr imaging. *Journal of Magnetic Resonance*, 180:22–30, 1995.

[18] Allen PS. Beaulieu C. An in vitro evaluation of the effects of local magnetic-susceptibility-induced gradients on anisotropic water diffusion in nerve. *Magnetic Resonance in Medicine*, 141:52–61, 1996.

[19] Tofts PS. Clark CA., Barker GJ. An in vivo evaluation of the effects of local magnetic susceptibility-induced gradients on water diffusion measurements in human brain. *Journal of Magnetic Resonance*, 141:52–61, 1999.

[20] LeBihan D. Basser PJ, Mattiello J. Estimation of the effective self-diffusion tensor from the nmr spin echo. *Journal of Magnetic Resonance B*, 103(3):247–254, 1994.

[21] LeBihan D Basser PJ, Mattiello J. Mr diffusion tensor spectroscopy and imaging. *Biophysical Journal*, 66(1):259–267, 1994.

[22] Tanner J.E. Stejskal, E.O. Spin diffusion measurements: Spin echoes in the presence of a time-dependent field gradient. *Journal of Chemical Physiology*, 42:288–292, 1965.

[23] Breton E. Lallemand D. Grenier P. Cabanis E. Laval-Jeantet M. LeBihan, D. Mr imaging of of intravoxel incoherent motions: application to diffusion and perfusion in neurologic disorders. *Radiology*, 161:401–407, 1986.

[24] Stefan Skare. Optimisation strategies in diffusion tensor mr imaging. Kongl. Carolinska Medico Chirurgiska Institutet, Karolinska University Press, 2002.

[25] Bo Nordell Martin Invar Stefan Skare, Tie-Qiang Li. Noise considerations in the determination of diffusion tensor anisotropy. *Magnetic Resonance Imaging*, 6(18):659–669, 2000.

[26] PJ Basser. Inferring microstructural features and the physiological state of tissues from diffusion weighted images. *NMR Biomed*, 8(7-8):333–344, 1995.

[27] Erik M. Akkerman. Efficient measurement and calculation of mr diffusion anisotropy images using the platonic variance method. *Magnetic Resonance in Medicine*, 49:599–604, 2003.

[28] Peter J. Basser and Carlo Pierpaoli. Microstructural and physiological features of tissues elucidated by quantitative-diffusion-tensor mri. *Journal of Magnetic Resonance*, 111:209–219, 1996.

[29] Carlo Pierpaoli and Peter J. Basser. Toward a quantitative assessment of diffusion anisotropy. *Magnetic Resonance in Medicine*, 36:893–906, 1996.

[30] Gordon Kindlmann Dennis L. Parker Andrew L. Alexander, Khader Hasan and Jay S. Tsuruda. A geometric analysis of diffusion tensor measurements of the human brain. *Magnetic Resonance in Medicine*, 44:283–291, 2000.

[31] Simmons A Jones DK, Horsfield MA. Optimal strategies for measuring diffusion in anisotropic systems by magnetic resonance imaging. *Magnetic Resonance in Medicine*, 42:515–525, 1999.

[32] http://www.nordicneurolab.com.

[33] Derek K. Jones. The effect of gradient sampling schemes on measures derived from diffusion tensor mri: A monte carlo study. *Magnetic Resonance in Medicine*, 51:807–815, 2004.

[34] Sinisa Pajevic and Carlo Pierpaoli. Color schemes to represent the orientation of anisotropic tissues from diffusion tensor date: Application to white matter fiber tract mapping in the human brain. *Magnetic Resonance in Medicine*, 42:526–540, 1999.

[35] P.J. Basser S. Marenco C. Pierpaoli G.K. Rohde, A.S. Barnett. Comprehensive approach for correction of motion and distortion in diffusion-weighted mri. *Magnetic Resonance in Medicine*, 51:103–114, 2004.

[36] http://www.fmrib.ox.ac.uk/fsl/.

[37] http://www.fmrib.ox.ac.uk/analysis/research/fdt/.

[38] Michael E. Moseley Tie-Qiang Li Stefan Skare, Maj Hedehus. Condition number as a measure of noise performance of diffusion tensor data acquisition schemes with mri. *Journal of Magnetic Resonance*, 147:340–352, 2000.

[39] Adolf Pfefferbaum and Edith V. Sullivan. Increased brain white matter diffusivity in normal adult aging: Relationship to anisotropy and partial voluming. *Magnetic Resonance in Medicine*, 49:953–961, 2003.

[40] Su Xu David A. Silberweig Emily Stern-Yihong Yang Wang Zhan, Hong Gu. Circular spectrum mapping for intravoxel fiber structures based on high angular resolution apparent diffusion coefficients. *Magnetic Resonance in Medicine*, 49:1077–1088, 2003.

[41] M. Jenkinson H. Johansen-Berg R.G. Nunes-S. Clare P.M Matthews J.M. Brady T.E.J. Behrens, M.W. Woolrich and S.M. Smith. Characterization and propagation of uncertainty in diffusion weighted mr images. Technical report, Oxford Centre for Functional Magnetic Resonance Imaging of the Brain, 2003.

[42] Frank J. Rybicki-Walid E. Kyriakos-Alan Edelman Gary P. Zientara Dimitris Mitsouras, W. Scott Hoge. Non-fourier encoded parallel mri using multiple receiver coils.

[43] http://www.sci.utah.edu/ gk/dti-data/.

[44] Mukundan G Kraut MA-Pomper MG van Zijl PC Melhem ER, Mori S. Diffusion tensor mr imaging of the brain and white matter tractography. *American Journal of Roentgenology*, 178:3–16, 2002.

[45] Peter J. Basser, Sinisa Pajevic, Carlo Pierpaoli, Jeffrey Duda, and Akram Aldroubi. In vivo fiber tractography using dt–mri data. *Magnetic Resonance in Medicine*, 44:625–632, 2000.

[46] Williams SC Horsfield MA Jones DK, Simmons A. Non-invasive assessment of axonal fiber connectivity in the human brain via diffusion tensor mri. *Magnetic Resonance in Medicine*, 42:37–41, 1999.

[47] Cull TS Akbudak E-Snyder AZ Shimony JS McKinstry RC Burton H Raichle ME Conturo TE, Lori NF. Trackin neuronal fiber pathways in the living human brain. *Proceedings of the National Academy of Sciences*, 96:10422–10427, 1999.

[48] Chacko VP van Zijl PC Mori S, Crain BJ. Three-dimensional tracking of axonal projections in the brain by magnetic resonance imaging. *Annals of Neurology*, 45:265–269, 1999.

[49] Akram Aldroubi Sinisa Pajevic and Peter J. Basser. A continous tensor field approximation of discrete dt-mri data for extractin microstructural and architectural features of tissue. *Journal of Magnetic Resonance*, 154:85–100, 2002.

[50] Barker GJ Rowe JB Mac-Manus DG Wheeler-Kingshott CA Ciccarelli O Passingham RE Spinks RL Lemon RN Turner R Parker GJ, Stephan KE. Initial demonstration of *in vivo* tracing of axonal projections in the macaque brain and comparison with the human brain using diffusion tensor imaging and fast marching tractography. *Neuroimage*, 15:797–809, 2002.

[51] Barker GJ Parker GJ, Wheeler-Kingshott CA. Estimating distributed anatomical connectivity using fast marching methods and diffusion tensor imaging. *IEEE Transaction on Medical Imaging*, 21:505–512, 2002.

[52] *Quantitative MRI of the Brain*, chapter D: the Diffusion of Water. John Wiley & Sons, Ltd, 2003.

[53] http://www.mathworks.com/products/matlab/description1.html.

[54] http://www.fil.ion.ucl.ac.uk/spm/spm2.html.

[55] http://sourceforge.net/project/showfiles.php?group_id=50847 &package_id=53694&release_id=240026. Current date: 2004-05-21.

[56] Stephen M. Smith. Fast robust automated brain extraction. *Human Brain Mapping*, 17(3):143–155, November 2002.

[57] Fick A. *Ann. Phys. Lpz.*, 170(59), 1855.

[58] Fourier JB. Théorie analytique de la chaleur, 1822.

[59] Carslaw HS. and Jaeger JC. Conduction of heat in solids, Oxford, 1947.

[60] Konstantinos Arfanakis, Bruce P. Hermann, Baxter P. Rogers, John D. Carew, Michael Seidenberg, and Mary E. Meyerand. Diffusion tensor mri in temporal lobe epilepsy. *Magnetic Resonance Imaging*, 20:511–519, 2002.